Ceramic Pottery Production in the North Caucasus in the Bronze Age and the Iron Age

A Dissertation

Submitted in Partial Fulfilment
of the Requirements for the Degree of
Doktor der Naturwissenschaften (Dr. rer. nat.)
to the Department of Earth Sciences
of Freie Universität Berlin

by Ki Suk Park

Berlin, November 2019

Supervisor: PD. Dr. Ralf Milke

Second Examiner: Prof. Dr. Patrick Degryse

Third Examiner: Prof. Dr. Elke Kaiser

Date of defense: February 3rd, 2020

Erklärung der Eigenständigkeit

Hiermit versichere ich, dass ich die vorliegende Arbeit selbstständig verfasst und keine anderen als die angegebenen Quellen und Hilfsmittel benutzt habe; alle Ausführungen, die anderen Schriften wörtlich oder sinngemäß entnommen wurden, kenntlich gemacht sind und die Arbeit in gleicher oder ähnlicher Fassung noch nicht Bestandteil einer Studien- oder Prüfungsleistung war.

Berlin, den 18.11.2019

Table of contents

List of tables

List of figures

Lithoclasts composed of K-feldspar, quartz and mica; (j) aggregate composed of clay, K-feldspar and quartz; (k) aggregate composed of clay in sintering, quartz (Ab: albite, An: anorthite, Byt: bytownite, Bt: biotite, Chl: chlorite, Clc: calcite, Cpx: clinopyroxene, Di: diopside, Lab: labradorite, Ol: olivine, Plg: plagioclase, Qtz: quartz, Sa: sanidine).

Figure 4-3. Mineralogical composition of dominant grain groups of the samples for the sites, (a) Ransyrt 1, (b) Kabardinka 2, (c) Levinsadovka–Saf'janovo with the back scattered electron (BSE) images of the representative grains [1] is compared to the size distribution, circularity and sphericity 1 of coarse sand grains (>250μm, lithoclasts) present in the selected samples (Clc: calcite, Cpx: clinopyroxene, Kfsp: K-feldspar, Sa: sanidine, Mica–Chl: mica–chlorite mixed layers, Bt: biotite, Ol: olivine, Plg: plagioclase, Qtz: quartz, Kln: kaolinite). Each mineralogical grain groups presented in different colors (Qtz + Kfsp + Mica – Chl/Qtz + Kfsp/Qtz (+Clc): light grey, Qtz + Kfsp + Plg + Mica Chl + Alteration/Qtz + Kfsp + Plg + Mica – Chl: light blue, Plg + Cpx: blue, Qtz + Kfsp + Clc: light yellow, Qtz + Complex sediments (+Clc): dark grey, various combinations: light green).

Figure 4-4. (a) Grain size distribution (max. length), (b) sphericity 1 and (c) sphericity 2 derived from 2D (blue) and 3D (orange) image analysis of the coarse sand grains (>250 μm) in the ceramic sherd (Ran1_514_2). Pixel size of 10^2 μm^2 and grain numbers/A (area) = 1.501 ea/mm^2 for the 2D images. Voxel size of 9.49^3 μm^3 and sand grain numbers/V (volume) = 12.182 ea/mm^3.

Figure 4-5. (a) Original ceramic sherd and segmented grain like cavities, calcite ghosts in the sample (blue and yellow) (voxel size: 25.00^3 μm^3). (b) A cross polarized light micrograph of the cross thin section shows coexisting calcite grains and closed type of voids in different sizes (Clc: calcite).

Figure 4-6. Chemical composition of ceramic matrix (grains < 50 μm) normalized to 100 wt.%: (a) SiO_2-Al_2O_3-CaO: (1) Ransyrt 1; (2) Kabardinka 2; (3) Levinsadovka-Saf'janovo; (b) at-f-alc (at=CaO+MgO; f= Fe_2O_3; alc=K_2O+Na_2O): (1) Ransyrt 1; (2) Kabardinka 2, (3) Levinsadovka-Saf'janovo.

Figure 4-7. Representative XRD and FT-IR (transmittance, samples heated at 170 °C for 60 hours) results of ceramic sherds excavated at Ransyrt 1 (blue) and Kabardinka 2 (orange, gray).

Figure 4-8. Illite d spacing at the lattice plane (020)/(110).

Figure 4-9. Comparison of SR-FIR absorption spectra and NIR diffuse reflectance spectra of the samples containing the lowest firing degree. (a) Ransyrt 1; (b) Kabardinka 2. Modified from *Park et al.* [1,22].

Figure 5-1. Photos of original ceramic sherds and segmented images of the large pore complex (blue) and sand grains (red and black) of the ceramics discovered at Ransyrt 1 (connectivity = 26). Region of interest (ROI) in the box of the white dashed line. (a) Bottom-wall fragments: 1. Separate formation of the bottom and wall part (wall on the bottom), oriented parallel pressure/stress from the surface (voxel size: 29.05^3 μm^3); 2. Continuous formation of the bottom and wall part (voxel size: 29.63^3 μm^3); 3. Separate formation of the bottom and wall part (wall next to the side of the bottom) (voxel size: 24.31^3 μm^3); 4. Two layers for the bottom building (voxel size: 28.21^3 μm^3); (b) Wall fragments: 1. Mixture of

List of publications related to the thesis

Articles: Archaeometry/Science

1. Park, K.S., Milke, R., Efthimiopoulos, I., Pausewein, R.R., Reinhold, S. Pyrometamorphic process of ceramic composite materials in pottery production in the Bronze/Iron Age of the Northern Caucasus (Russia). Sci. Rep. 9 (2019) 10725. https://doi.org/10.1038/s41598-019-47228-y.

: Chapter 1, 2, 3, 4, 6

2. Park, K.S., Milke, R., Rybacki, E., Reinhold, S. Application of image analysis for the identification of prehistoric ceramic production technologies in the North Caucasus (Russia, Bronze/Iron Age). Heritage 2 (2019) 2327-2342. https://doi.org/10.3390/heritage2030143.

: Chapter 1, 2, 3, 4, 5, 6

3. Park, K.S., Schade, U., Vrijmoed, J.C., Reinhold, S., Milke, R. Redox-thermal behavior of the archaeological ceramics from the North Caucasus (Russia, Bronze/Iron Age). J. Eur. Ceram. Soc. 40 (2020) 2207-2221. https://doi.org/10.1016/j.jeurceramsoc.2020.01.030.

: Chapter 1, 2, 3, 6; modified from the preprint of the article

Articles: Archaeology/Review/Methodology

1. Park, K.S., Milke, R., Rybacki, E., Reinhold, S. Image analysis of the archaeological ceramics and its application to the identification of the prehistoric production technologies. In: Proceedings of the 6th international conference, 'Methodology&Archaeometry', Zagreb, Croatia, December 6th-7th 2018; I. Miloglav (Ed.) (in press).

: Chapter 1, 2, 3, 5; modified from the preprint of the article

2. Park, K.S., Reinhold, S., Milke, R. Pottery production technology and technological style in the North Caucasus (Russia) in the Bronze/Iron Age: Archaeological characterization from archaeometric results. (in prep.).

: Chapter 1, 2, 3, 4, 5, 6, 7; ; modified from the preprint of the article

Abstract

The ceramic pottery production in the North Caucasus in the Bronze and Iron Age enables us to understand the production technology, technological development and transfer, craft system and mobility of the potters in the semi-sedentary and semi-mobile society. However, most prehistoric archaeological ceramics are heterogeneous composite materials containing various chemical and mineralogical compositions, firing states and alteration degrees, so that the ceramic production technology cannot be easily characterized and classified. Moreover, the amount of the excavated ceramic objects is huge, which causes additional difficulty for the analysis.

In order to overcome these limitations, multiproxy- and multiscale-approach was employed step by step using polarization light microscopy (PM), scanning electron microscopy with energy/wavelength-dispersive spectroscopy (SEM/SEM-EDS/WDS), X-ray powder diffraction (XRD), Fourier transform infrared spectroscopy (FTIR), synchrotron radiation Fourier transform infrared (SR-FTIR), Raman spectroscopy, three dimensional micro computed tomography (3D μ-CT) and image analysis. Firing conditions such as time, heating rate and temperature were concretized by the kinetics of the dehydroxylation of the clay mineral and finite different method (FDM) on the oxygen diffusion and heat transfer. This combined approach focused on resource gathering, firing and shaping techniques. The total 150 samples excavated at two archaeological sites in the North Caucasus, Ransyrt 1 (Middle/Late Bronze Age) and Kabardinka 2 (Late Bronze/Early Iron Age) were investigated. Samples of 21 ceramic sherds uncovered at Levinsadovka and Saf'janovo around the Sea of Azov, Russia (Late/Final Bronze Age) were compared to the mountain ceramics.

According to the results, the mineralogy and shape parameters of sand grains and chemical composition of the ceramic matrix composed of grains smaller than 50 μm were able to distinguish the ceramic pastes from each site. This provides the potters' practice of the main use of the local resource. The alignment of the large pore complex and grains enabled to identify the continuous or modular slab building by hands for the formation of the ceramic pottery body. The firing techniques were derived from the pyrometamorphic process under oxidizing and reducing conditions and corresponding firing behavior of the composite materials containing the common clay mineral, *cis/trans-vacant (cv/tv)* 1M illite. The complex combination of clay sintering, pore topology and its Euler characteristic and transformation of the indicator minerals such as calcite, hematite, spinel and gehlenite gave detailed clues for the firing temperature thresholds between under 675 and 1200 °C. In many ceramics fired in the oxidizing atmosphere, the reactivity between oxygen and Fe-, C- and S-bearing phases present in the ceramic pastes caused localization of the redox state within a sample, forming a color profile on the cross section of the object. In the middle of the cross section of those samples, earlier dehydroxylation of illite and corresponding total collapse occur due to the local reduction. The firing conditions derived from the dehydroxylation kinetics of illite and simulation of the oxygen diffusion and heat transfer indicate that the non-isothermal conditions with the high heating rate could produce the ceramic pottery with various

firing degrees within a few hours by the instant firing without a furnace. The firing practice at both sites were similar, however the firing temperatures of the Kabardinka 2 ceramics are distributed in the wider range than those of the Ransyrt 1 ones, which might be related to the longer history of the settlement at Kabardinka 2.

According to the combination of the archaeometric results and archaeological contexts, the local ceramic pottery production technologies at both sites were driven by similar human practice and site-specific resource. Although the individual decision making in the pottery production contributed to the heterogeneity of the ceramics as well, the resource-driven local technological styles dominated the pottery production at the studied sites in the Bronze and Iron Age. This characterization will shed light on the understanding of the development and transfer of the production technology in the North Caucasus.

Abstract (in German)

Die Keramik- und Keramikvesselproduktion im Nordkaukasus der Bronze- und Eisenzeit ermöglicht uns, die Produktionstechnologie, deren Entwicklung und Transfer der Technologie, Handwerk und Mobilität der Handwerker in einer Gesellschaft, wo eine kombinierte Form des mobilen und sesshaften Lebensstils existierte. Heterogene Komposite wie archäologische Keramikscherben beinhalten verschiedene chemische und mineralogische Zusammensetzungen, Feuerzustände und Alterationsgrade innerhalb einzelner Proben erschweren damit die spezifische Charakterisierung und davon abgeleitete Klassifikation von Keramikscherben durchgeführt werden können. Darüber hinaus wurden bei den meisten Ausgrabungen wurden große Mengen von Keramikobjekten gefunden, deren zahlreiche schwer einzuordnen und zu untersuchen sind.

In diesem Projekt wurde Multiproxy- und Multiskalen-Herangehensweise verwendet, um diese Beschränkungen zu überwinden. Die integrative Probencharakterisierung wurde mit den folgenden Methoden durchgeführt: Polarisationsmikroskopie, Rasterelektronenmikroskopie mit wellenlängen- und energiedispersiver Röntgenspektroskopie, Röntgenpulverbeugung, Fourier-Transform-Infrarotspektrskopie, Synchrotron-Fourier-Transform-Infrarotspektroskopie, Ramanspektroskopie, 3D Mikro-Computertomographie und Bilderkennung und -analyse. Brennbedingungen wie Dauer, Erwärmungsrate und Brenntemperatur wurden von der Kinetik der Dehydroxylation von Tonmineralen und Finite-Differenzen-Methoden für Sauerstoffdiffusion und Wärmeübertragung abgeleitet. Für die Charakterisierung der Produktionstechnologie, wurden Präparation von Keramikpasten, Brenntechnik und Formationstechnik intensiv untersucht. Die Proben von 150 Keramikscherben wurden an zwei archäologischen Plätzen im Nord Kaukasus (Russland) ausgegraben: Ransyrt 1 (Mitel/Spät-Bronzezeit) und Kabardinka 2 (Spät-Bronze- und Früh-Eisenzeit). Die Proben von 21 Keramikobjekten aus Levinsadovka and Saf'janovo am See von Azov, Russland (Spät/Final-Bronzezeit) wurden verglichen.

Nach der Mineralogie und Formparameter der Sandkörner und der chemischen Zusammensetzung aller Körner, die kleiner als 50 µm sind, konnten die Keramikproben dem zuständigen archäologischen Platz zugeordnet werden. Die lokalen Töpfer hätten die Ressource in der nahen Umgebung ihrer Siedlung besorgt. Die Orientierung der Poren und Körner in den Keramikscherben weist darauf hin, dass die Struktur der Objekte durch kontinuierliche Bildung oder Montagen von funktionalen Platten mit den Händen gebildet wurde. Diese Formationstechnik ist bei den Scherben aus den beiden Siedlungen zu finden. Die Brenntechnik wurde durch den pyrometamorphischen Prozess vor allem, das Brennverhalten von *cis/trans-vacant (cv/tv)* 1M Illit, das gemeinsame Tonmineral der meisten Proben, in der Oxidation und Reduktion identifiziert. Die Kombination des Sinterprozesses von Illit, Porentopologie und deren Euler Nummer und Transformation der Indikatorminerale wie Kalzit, Hematit, Spinell und Gehlenit konnte Information über Brenntemperaturen von unter 675 bis 1200 °C vermitteln. Trotz der oxidierenden atmosphärischen Bedingung bei dem Brennvorgang, ist öfters zu sehen, dass die Reaktion zwischen Sauerstoff und Fe-, C- und S-Phasen in den Ressourcen die lokale Reduktion und Oxidation

innerhalb der Probe verursacht. Diese Lokalisierung des Zustandes der Oxidation und Reduktion erscheint als das Farbprofil in dem Querschnitt. Die frühe Dehydroxylation von Illit passiert in der Mitte des Querschnittes der Probe, wo die lokale Reduktion aktiv ist. Nach der Berechnung der Dehydroxylationskinetik für Illit bzw. der Simulation über die Wärmeübertragung der Keramik und Diffusion von Sauerstoff konnte das nicht-isothermische Temperaturbedingung mit dem hohen Erwärmungsrate mehrere unterschiedlich gebrannte Objekte in wenigen Stunden ermöglichen. Diese Technik ohne Brennofen oder ähnliche Struktur wurde an den beiden archäologischen Plätzen durchgeführt. Die längere Nutzung der Siedlung in Kabardinka 2 bezieht sich auf den breiteren Bereich für die Brenntemperaturen von den Scherben.

Im Zusammenhang mit dem archäologischen Kontext ist die Keramikproduktionstechnologie an den beiden untersuchten Plätzen als ähnliche Praxis der Töpfer und lokale Ressource zu charakterisieren. Obwohl die individuellen Entscheidungen der Töpfer bei der Produktion zur Vielfalt der Eigenschaften der Keramik beitrugen, beherrschte der lokale technologische Stil, der von den lokalen Ressourcen angetrieben wurde die Keramikproduktion an Ransyrt 1 und Kabardinka 2. Diese Charakterisierung des lokalen technologischen Stiles in der Keramikproduktion wird zur Verständnis über die Entwicklung der Technologie und deren Transfer über Nordkaukasus weiter eine große Rolle spielen.

Acknowledgements

For the supervision of my work, I would like to thank PD. Dr. Ralf Milke (Institut für Geologische Wissenschaften, FU Berlin), Prof. Dr. Patrick Degryse (Division of Geology, Katholieke Universiteit Leuven & Department of Archaeological Sciences, Universiteit Leiden) and Prof. Dr. Elke Kaiser (Institut für prähistorische Archäologie, FU Berlin).

The main archaeological contexts and objects for this project were provided by PD. Dr. Sabine Reinhold (Deutsches Archäologisches Institut, Berlin). I am very grateful for her permission and support for the archaeometric research. Related to the field work, I wish to thank Dr. D.S. Korobov (Institute of Archaeology, Russian Academy of Sciences) and Dr. A.B. Belinskij (GUP Nasledie, cultural heritage organization in the Stavropol Region, Russia) for the support, as well as the international students in the survey and excavation. Leon van Hoof (FU Berlin) and Prof. Dr. Ortwin Dally (Deutsches Archäologisches Institut, Rom) provided archaeological ceramics from the Taganrog archaeological project for the comparison. I want to thank them for their help.

Regarding the archaeometric approach, I am very grateful for the mineralogy/petrology workgroup led by Prof. Dr. Timm John and the Institut für Geologische Wissenschaften, Freie Universität Berlin. Dr. Moritz Liesegang (Universität Bonn), Sascha Zertani and Prof. Dr. Esther Schwarzenbach gave constructive advice for the doctoral work, together with the help for the analysis. Dr. Tina Menneken (Universität Bonn) and Robbin Visser gave the big support for the Raman spectroscopy. Dr. Johannes C. Vrijmoed supervised the numerical simulations. Prof. Dr. Susan Schorr organized the access to synchrotron facility. Sabine Meister and Fadime Ay helped at the laboratory work. Anna Giribaldi prepared thin section samples of the ceramics despite of the difficulty. René Schleuer provided IT-support. Philip Groß gave an access with the guide to the polarized light microscopy with the specific magnification. Jan Evers supported the measurements of FESEM at the paleontology group. I wish to thank all the people in the group for the support.

I got chances to use 3D µ-CT at GFZ (Potsdam). I want to mention that Dr. Erik Rybacki and Claudius Marx supported the measurements using 3D µ-CT. Hans-Peter Nabein provided technical advice for related instruments and program as well. I am very grateful for their help.

FTIR were measured in the Rathgen-Forschungslabor (Berlin), GFZ and HZB. I would like to thank to Dr. Ilias Efthimiopoulos (GFZ), Prof. Dr. Monika Koch-Müller (GFZ), Regine-Ricarda Pausewein (Rathgen-Forschungslabor) and Dr. Ina Reiche (Institut de Recherche de Chimie Paris), Dr. Ulrich Shade (HZB) and Dr. Ljiljana L. Puskar (HZB) for the huge support and advice. I am also grateful for the HZB for the access to the IRIS beamline of the electron storage ring BESSY II.

Lastly, I would like to acknowledge the colleagues in archaeometry, Ariadni Kostomitsopoulou Marketou (University of Oslo) and Katharina Kuntz (FU Berlin), Takehiro Miki (FU Berlin) and Thomas Rose (Ben Gurion University of the Negev) for the advice and discussion. I hope all the success in their research.

Chapter 1. Introduction

The archaeological ceramics are one of the most common objects found at the excavations of the prehistoric and historic sites and the ceramic pottery production technology is one of the most important topics in the archaeological and archaeological scientific studies. Based on the occurrence, frequency at the excavations, ubiquitous characteristics in the daily and specific use and accessibility to the users, production technology of pottery would have influenced the life of the prehistoric and historic people, their knowledge, knowledge production. Therefore, the identification of ceramic production technology is considered as the main issue for understanding of ancient material production techniques, technology transfer, formation of the regional technological styles.

1.1. Purpose of the study:

Direct measurements based multiproxy and multiscale archaeometric approach for the characterization of pottery production technology in the North Caucasus (Russia, Bronze/Iron Age)

The main purpose of this doctoral study is to identify the production technology of the ceramic pottery in the North Caucasus during the Late Bronze- and the Early Iron Age (1400 BC. – 800/700 BC.). The main objects are the ceramic sherds excavated at the archaeological settlement sites at Ransyrt 1 and Kabardinka 2. The potters might have followed five steps of the production: preparation, shaping, drying, firing and post-firing. The identification of technical elements imprinted by potters' action during each step will be the key to characterize employed technologies and technological styles composed of human practice for production. In this study, three main steps of production, preparation of the ceramic pastes, shaping and firing techniques will be focused intensively by a multiproxy and multiscale approach for the samples representing for the settlement ceramics of the archaeological site. These topics decide local technological styles together with the social system. In the prehistoric craft system, this firing technology was transferred through practice in small scale interpersonal relations [1] and characteristic ways of controlling fire in various conditions designated local technological styles [2-4]. The serial combination of various methods such as polarized light microscopy, Scanning electron microscopy with energy/wavelength-dispersive X-ray spectroscopy (SEM-EDS/WDS), X-ray powder diffraction (XRD) and Fourier-transform infrared spectroscopy (FT-IR, absorbance, reflectance)/Synchrotron (SR)-FT-IR (absorbance), Raman spectroscopy, 3D μ-computed tomography (3D μ-CT) coupled with image analysis covering various observation scales is expected to figure out the local technological styles derived from the human and nature induced factors in the ceramics with the proper sequence. In direct measurements of the original samples, the heterogeneity in the mineralogical and chemical composition and thermal property of most prehistoric ceramics make it difficult to identify production technologies and technological styles. For example, common clay minerals such as illite has polytypes with heterogeneous thermal decomposition procedure in different temperatures under heating [5-6]. Various

sized sand grains composed of different minerals in the ceramics will interrupt the precise interpretation of the firing state. Furthermore, most archaeological sites yield numerous ceramic sherds which carry different technological styles within a same site. Previous researches studying production technologies of archaeological ceramics have focused either on the chemical composition in a macroscale or firing behaviors of a few specific mineral phases or on the experimental approach, producing of the replicates of the original samples. However, despite of the in-depth studies focusing on the identification of the ceramic pastes and thermal deformation and transformation of the archaeological ceramics, the various kinds of the heterogeneity of many original objects are not always easy to reproduce in the laboratory based experiments, besides of the precise identification of the elemental and structural components. Moreover, these ceramic materials deliver complex information about the material production techniques in various observation scales, which is not easy to interconnect for the archaeological interpretation.

In order to overcome these issues, samples will be measured for a macroscale and categorized into corresponding data groups. Regarding the high number of consisting chemical elements and mineral and mineral like phases, the dominant phase or component will be identified for the classification. From the groups at each measurement step, representative samples will be selected for the further measurement with a higher resolution. With this approach, the data representing various resources and firing conditions can be gathered efficiently from numerous samples. Moreover, average firing conditions estimated from macroscale observations as well as more precise pyrometamorphic state within a sample from a meso-/microscale can be compared to each other, so that the more precise categorization and interpretation are possible. Especially, firing behavior of the composite materials will be characterized from the level of the mobility of chemical elements up to macroscale. The possible firing conditions will be generally suggested from calculation of dehydroxylation kinetics of the identified clay mineral, oxygen diffusion and heat transfer rate within porous ceramics. The archaeologically important parameters such as firing time and temperature, heating rate and reduction-oxidation will be derived. Both 2D and 3D images and their parameterization of highly heterogeneous archaeological ceramics will provide visualized and numeric evidence in various scales about prehistoric ceramic production technologies focusing on resource gathering, firing degree by the quantitative evaluation and shaping techniques qualitatively.

1.2. Production technology as human practice

At the level of actual practice, technologies are always organized through techniques of the body and the form, use and function of a technology cannot be separated from the practices [7]. In order to figure out distribution of techniques and technical groups in the Late Bronze- and Early Iron Age, I choose to employ a theory of practice which can connect ceramic pottery manufacture to human practice. This theory focuses on how humans, with their diverse motives and intentions, make and transform the world in which they live. Imitation, repetition, imprinting, training, and sanctions make the human body the

crucial intermediary in the transmission, acquisition, and reproduction of social practices [8]. Habitus, one of the key concepts from the Bourdieu's approach to practices, is a generative principle, allowing for creativity and improvisation [9] and agency is denoted for an actor choosing to act. According to Bourdieu, technologies that involve the human body are essentially subsets of habitus, organized forms of movement [7]. It has been one of the common characteristics of technologies in the industry of non-automated systems. The practical sense of technologies carries the social history from small scale interpersonal relations in which technology was once embedded, and the relations in which the experiencing individual is embedded [7,10]. This is a useful approach of viewing the process by which patterns in ceramic pottery production are assimilated and reproduced, particularly in the case of prehistoric societies where craft learning generally takes place through observation and emulation without use of a formally articulated set of rules [11]. This dynamic process enables to explain how distribution of production technologies occurred in specific social relations and contexts. In addition, ethnological elements which are used for interpretation of results about the relationship between technological styles of archaeological potteries and potters in various regional and ethnic groups by ethnoarchaeologists, will be considered for my study, too. The specific regional social context is reconstructed using identified settlement types and regional archaeological cultures in the Late Bronze- and the Early Iron Age, in order to offer regional social and cultural background of development of technology, technological practice and technical groups.

1.3. History of the ceramic archaeometry

Many previous studies employed experimental approaches, such as firing soils or clay minerals acquired at sites. The firing products from such experiments were compared to the excavated ceramics using XRD, differential thermal analysis (DTA)/thermogravimetric analysis (TG), X-ray fluorescence (XRF), FT-IR, SEM or transmission electron microscopy (TEM) coupled with EDS [12-22]. Al-K edge X-ray absorption near edge structure (XANES) was employed to explain changes in structural order and firing products of kaolinite based clay [23]. The results were often compared to the micromorphological changes in BSE images. Sintering process of clay minerals in the ancient ceramics could be observed by atomic force microscopy (AFM) and piezo response-force-microscopy instrumentation [24]. Besides, Raman spectroscopy and Fe-K edge XANES are employed to determine oxidation states of iron [25-26] Additionally, Mössbauer shed light on the oxidation state of Fe ions in silicates indicating different degree of firing temperature and $f(O_2)$ [27]. Parameters in physical or mechanical properties such as bending strength, porosity and thermal conductivity are changed according to the firing temperature [28-30]. Changes in the magnetic susceptibility which could be related with mobility of Fe ions, were used for the estimation of the firing temperature [31]. Spectrocolorimetric analysis showing the relationship between reflectance spectra and CIE L*a*b* colorimetric measurements confirmed with TEM-EDX provides information on iron compounds developed in various firing conditions including combined firing atmosphere and temperature [32]. The changes in the colors of the various parts of the ceramics

during firing were investigated, in terms of the formation and transformation of Fe-bearing minerals such as hematite and magnetite according to the temperature and oxygen partial pressure [27,33-34]. The black coring effect is one of the phenomena closely related to oxidation-reduction states in ceramics during firing [35-37]. Because most ceramic pastes gathered from sediments contain Fe- and C-bearing phases, their thermally induced reactivity to O together with H_2O causes the complex reaction chains of the electronic charge transfer and gasification in the ceramic matrix composed of the ferrosiliceous minerals, iron oxides/hydroxides and carbonates, micro-organics, S-bearing phases [38-41]. The localized oxygen partial pressure from this interaction contributes to the formation of the color profile within the cross section such as reddish brown in the sides and dark brown in the middle of the object. Besides, the firing conditions or the thermal behavior of the clay based ceramics were suggested from the heat transfer simulations using finite element method using the material properties from experiments [42-43].

In addition to the analytical instruments from the fundamental to the advanced level, there has been a rapidly growing demand for the application of image analysis and image processing in the past twenty years [44-45]. Above all, the application of high resolution X-ray CT clarified the internal structure of fossils, meteorite, textural differences in magmatic, metamorphic and sedimentary rocks and related soils as well as products of sintering procedures [46-51]. This technique is supported by the mass data processing accompanied by the progress in the central processing unit (CPU) and graphics processing unit (GPU) and the data transport system. This allowed the image visualization and segmentation as well as the complex calculation of the geometry of the studied objects such as curvatures of powder grains and interstitial pore topology. Advanced image acquisition and analysis have a huge research potential in archaeology and archaeological sciences. Thanks to the mobility of digital data, researchers can perform the analysis in relatively political and geographical boundary free conditions without the necessity to transport the fragile archaeological objects over long distance and time.

In previous studies, polarized light microscopic images or scanned images of cross thin sections of ceramics were used for the identification of various technical aspects in pottery production, such as ceramic pastes, shaping techniques [52-60]. Alignments and their distributions of grains or pores with specific angles and layout provided clues about the shaping techniques such as coiling, molding or wheel shaping/throwing making use of rotational kinetic energy [59-63]. The 2D image analysis of cross thin sections and 3D analysis using X-ray radiography or 3D μ-CT were employed to characterize the grain size and pore size distribution and to prove specific temper materials in ceramics such as organic materials or heavy minerals [56-58,64-65]. Back scattered electron (BSE) images acquired by SEM have provided classical evidence about the temperature dependence of the pore morphology of various ceramics [66-67]. The porosity of the ceramics can be supplemented by the Brunauer–Emmett–Teller (BET) method or mercury intrusion porosimetry (MIP) [68-69].

However, the image analysis of most prehistoric ceramics is still not easy to employ for the study of pottery production technologies, because archaeological ceramics are composed of various

heterogeneous mineral phases and chemical compositions, various alteration degrees and firing states within a single sample [70-73]. These properties make it difficult to measure and segment, reconstruct and analyze the region of interest (ROI), the target area of the measurement by the microscopy and 3D μ-CT, from the object in 2D and 3D and this time consuming process is almost impossible to be employed for the whole archaeological ceramics which are found in massive amounts at each archaeological sites. Nevertheless, the research potential of image analysis in archaeological sciences is very large. Various structural elements and components and their shapes and layouts within a ceramic sherd can be directly measured and linked to the various physico–chemical and chemical–mineralogical properties reflecting production site, firing states and forming techniques. The identified techniques will contribute to the reconstruction of prehistoric regional crafts and their technological styles as well [74-77].

1.4. References

1. Dietler, M. and Herbich, I. Habitus, techniques, style: An integrated approach to the social understanding of material culture and boundaries. In: Stark, M.T. (Ed.), The Archaeology of social boundaries, Smithsonian Institution Press: Washington D.C. (1998) pp. 232-263.

2. Lechtman, H. Style in technology: Some early thoughts. In: Lechtman, H., Merrill, R.S. (Eds.), Material culture: Style, organization and dynamics of technology, West Publishing Company:
St. Paul (1977) 3-20.

3. Pfaffenberger, B. Social anthropology of technology. Annual Review of Anthropology 21, 491-516 (1992).

4. Gosselain, O.P. Social and technical identity in a clay crystal ball. The Archaeology of social boundaries, Smithsonian Institution Press: Washington D.C. (1998) pp. 78-106.

5. Drits, V.A. and McCarty, D.K. The nature of diffraction effects from illite and illite-smectite consisting of interstratified trans-vacant and cis-vacant 2:1 layers: A semi-quantitative technique for determination of layer-type content. Am. Mineral. 81 (1996) 852-863.

6. Pevear, D.P. Illite and hydrocarbon exploration. Proc. Natl. Acad. Sci. U.S.A. 96 (7) (1999) 3440-3446. https://doi.org/10.1073/pnas.96.7.3440.

7. Sterne, J. Bourdieu, Technique and Technology. Cultural studies 17 (3/4) (2003)367-389. https://doi.org/10.1080/0950238032000083863a.

8. Bourdieu, P. Outline of a theory of practice, Cambridge university press: NY. (1977). https://doi.org/10.1017/CBO9780511812507.

9. Bourdieu, P. The logic of practice, Stanford university press: Stanford (1990).

10. Dietler, M. and Herbich, I. Habitus, techniques, style: An integrated approach to the social understanding of material culture and boundaries. In: M.T. Stark (ed.), The Archaeology of social boundaries, Smithsonian Institution Press: Washington D.C. (1998) pp. 232-263.

11. Herbich, I. Learning patterns, potter interaction and ceramic style among the Luo of Kenya. The African Archaeological Review 5 (1987) 193-204.

12. Pennisi, L. In ceramics and glasses. Engineering Materials Handbook vol. 4, ASM International: Materials Park, OH (1991) pp. 255–259.

13. Duminuco, P., Messiga, B., Riccardi, M.P. Firing process of natural clays. Some microtextures and related phase compositions. Thermochim. Acta 321 (1998) 185-190. https://doi.org/10.1016/S0040-6031(98)00458-4.

14. Riccardi, M.P., Messiga, B., Duminuco, P. An approach to the dynamics of clay firing. Appl. Clay Sci. 15(3-4) (1999) 393-409. https://doi.org/10.1016/S0169-1317(99)00032-0.

15. Cultrone, G., Rodriguez-Navarro, C., Sebastian, E., Cazalla, O., De La Torre, M.J. Carbonate and silicate phase reactions during ceramic firing. Eur. J. Mineral. 13 (2001) 621-634. https://doi.org/10.1127/0935-1221/2001/0013-0621.

16. Jordán, M.M., Sanfeliu, T., de la Fuente, C. Firing transformations of Tertiary clays used in the manufacturing of ceramic tile bodies. Appl. Clay Sci. 20 (2001) 87-95. https://doi.org/10.1016/S0169-1317(00)00044-2.

17. Aras, A. The change of phase composition in kaolinite- and illite-rich clay-based ceramic bodies. Appl. Clay Sci. 24 (2004) 257-269. https://doi.org/10.1016/j.clay.2003.08.012.

18. Trindade, M.J., Dias, J., Coroado, M.I., Rocha, F. Mineralogical transformations of calcareous rich clays with firing: A comparative study between calcite and dolomite rich clays from Algarve, Portugal. Appl. Clay Sci. 42 (2009) 345-355. https://doi.org/10.1016/j.clay.2008.02.008.

19. Rathossi, C., Pontikes, Y. Effect of firing temperature and atmosphere on ceramics made of NW Pelephonnese clay sediments, Part I: Reaction paths, crystalline phases, microstructure and colour. J. Eur. Ceram. Soc. 30 (2010) 1853-1866. https://doi.org/10.1016/j.jeurceramsoc.2010.02.002.

20. Shoval, S., Yadin, E., Panczer, G. Analysis of thermal phases in calcareous Iron Age pottery using FT-IR and Raman spectroscopy. J. Therm. Anal. Calorim. 104 (2011) 515-525. https://doi.org/10.1007/s10973-011-1518-5.

21. Damjanović, L., Bikić, V., Šarić, K., Erić, S., Holclajtner-Antunović, I. Characterization of the early Byzantine pottery from Caričin Grad (South Serbia) in terms of composition and firing temperature, J. Archaeol. Sci. 46 (2014) 156-172. https://doi.org/10.1016/j.jas.2014.02.031.

22. Ricci, G., Caneve, L., Pedron, D., Holesch, N., Zendri, E. A multi-spectroscopic study for the characterization and definition of production techniques for German ceramic sherds. Microchem. J. 126 (2016) 104-112. https://doi.org/10.1016/j.microc.2015.12.009.

23. Andrini, L., Gauna, M. R., Conconi, M. S., Suarez, G., Requejo F. G., Aglietti, E. F., Rendtorff, N. M. Extended and local structural description of a kaolinitic clay, its fired ceramics and intermediates: An XRD and XANES anaylsis. Appl. Clay. Sci. 124-125 (2016) 39-45. https://doi.org/10.1016/j.clay.2016.01.049.

24. Emami, M., Sakali, Y., Pritzel, C., Trettin, R. Deep inside the ceramic texture: A microscopic–chemical approach to the phase transition via partial-sintering processes in ancient ceramic matrices. J. Microsc. Ultrastruct. 4(1) (2016) 11-19. https://doi.org/10.1016/j.jmau.2015.08.003.

25. Cianchetta, I., Maish, J., Saunders, D., Walton, M., Mehta, A., Foran, B., Trentelman, K. Investigating the firing protocol of Athenian pottery production: A Raman study of replicate and ancient sherds. J. Raman. Spectrosc. 46 (2015a) 996-1002. https://doi.org/10.1002/jrs.4662.

26. Cianchetta, I., Trentelman, K., Maish, J., Saunders, D., Foran, B., Walton, M., Sciau, Ph., Wang, T., Pouyet, E., Cotte, M., Meirer, F., Liu, Y., Pianetta, P., Mehta, A. Evidence for an unorthodox firing sequence employed by the Berlin Painter: deciphering ancient ceramic firing conditions through high-resolution material characterization and replication. J. Anal. At. Spectrom. 30 (2015b) 666-676. https://doi.org/10.1039/C4JA00376D.

27. Maritan, L., Nodari, L., Mazzoli, C., Milano, A., Russo, U. Influence of firing conditions on ceramic products: Experimental study on clay rich in organic matter. Appl. Clay. Sci. 31 (2006) 1-15. https://doi.org/10.1016/j.clay.2005.08.007.

28. Jordán, M.M., Montero, M.A., Meseguer, S., Sanfeliu, T. Influence of firing temperature and mineralogical composition on bending strength and porosity of ceramic tile bodies. Appl. Clay. Sci. 42 (2008) 266-271. https://doi.org/10.1016/j.clay.2008.01.005.

29. Allegretta, I., Eramo, G., Pinto, D., Hein, A. The effect of mineralogy, microstructure and firing temperature on the effective thermal conductivity of traditional hot processing ceramics. Appl. Clay. Sci. 135 (2017) 260-270. https://doi.org/10.1016/j.clay.2016.10.001.

30. Mahmoudi, S., Bennour, A., Srasra, E., Zargouni, F. Characterization, Firing Behavior and Ceramic Application of Clays from the Gabes region in South Tunisia, Appl. Clay. Sci. 135 (2017) 215-225. https://doi.org/10.1016/j.clay.2016.09.023.

31. Karacic, S., Jameson, M., Weil, A.B. A Burning Issue: Firing Temperatures and the Production of Late Bronze Age Pottery from Tarsus-Gözlükule, Turkey, J. Archaeol. Sci. Rep. 9 (2016) 599-607. https://doi.org/10.1016/j.jasrep.2016.08.046.

32. Cianchetta, I., Trentelman, K., Walton, M.S., Maish, J., Mehta, A., Foran, B. Reverse engineering ancient Greek ceramics: morphological and spectral characterization of replicas, J. Am. Ceram. Soc. 99(5) (2016) 1792-1801. https://doi.org/10.1111/jace.14123.

33. Nodari, L., Marcuz, E., Maritan, L., Mazzoli, C., Russo, U. Hematite nucleation and growth in the firing of carbonate-rich clay for pottery production, J. Eur. Ceram. Soc. 27 (2007) 4665-4773. https://doi.org/10.1016/j.jeurceramsoc.2007.03.031.

34. de Bonis, A., Cultrone, G., Grifa, C., Langella, A., Leone, A.P., Mercurio, M., Morra, V., Different shades of red: The complexity of mineralogical and physico-chemical factors influencing the colour of ceramics, Ceram. Int. 43(11) (2017) 8065-8074. https://doi.org/10.1016/j.ceramint.2017.03.127.

35. Brownell, W.E. Black Coring in Structural Clay Products. J. Am. Ceram. Soc. 40(6) (1957) 179-187. https://doi.org/10.1111/j.1151-2916.1957.tb12600.x.

36. Abdrakhimov, V.Z., Abdrakhimova, E.C. Formation of the black core in high-speed firing of floor tiles. Glass and Ceramics 56(7-8) (1999) 263–265. https://doi.org/10.1007/BF02681509.

37. Stolecki, J., Murzyn, P. Influence of firing conditions on properties of ceramic materials made of carbon slate, Materiały Ceramiczne 63(1) (2011) 74-79.

38. Du, Z., Sarofim, A.F., Longwell, J.P., Tognotti, L., The CO/CO2 Ratio in the Products of the Carbon-Oxygen Reaction, in: J. Lahaye, P. Ehrburger (Eds.), Fundamental Issues in Control of Carbon Gasification Reactivity. NATO ASI Series (Series E: Applied Sciences) 192, Springer: Dordrecht (1991) pp. 91-106. https://doi.org/10.1007/978-94-011-3310-4_5.

39. Longbottom, R.J., Kolbeinsen, L. Iron ore reduction with CO and H_2 gas mixtures- thermodynamic and kinetic modelling. Proceedings of the 4th Ulcos seminar – New Direct Reduction (DR). 1st & 2nd October 2008, 1-13. http://ro.uow.edu.au/engpapers/1260.

40. Neumann, A., Petit, S., Hostetter, T.B., Evaluation of redox-active iron sites in smectites using middle and near infrared spectroscopy, Geochim. Cosmochim. Acta. 75 (2011) 2336-2355.

41. Gredmaier, L., Banks, C.J., Pearce, R.B. Calcium and sulphur distribution in fired clay brick in the presence of a black reduction core using micro X-ray fluorescence mapping, Constr. Build. Mater. 25(12) (2011) 4477-4486. https://doi.org/10.1016/j.conbuildmat.2011.03.054.

42. Hein, A., Kilikoglou, V., Modelling of thermal behavior of ancient metallurgical ceramics, Journal of the American Ceramic Society 90(3) (2007) 878 – 884. DOI: 10.1111/j.1551-2916.2006.01466.x.

43. Papathanasiou, T.K., dal Corso, F., Piccolroaz, A. Thermo-mechanical response FEM simulation of ceramic refractories undergoing severe temperature variations, J. Eur. Ceram. Soc. 36(9) (2016) 2329-2340. https://doi.org/10.1016/j.jeurceramsoc.2016.01.022.

44. Cnudde, V., Boone, M.N. High-resolution X-ray computed tomography in geosciences: A review of the current technology and applications. Earth-Sci. Rev. 123 (2013) 1–17.

45. Ketcham, R.A.; Carlson, W.D. Acquisition, optimization and interpretation of X-ray computed tomographic imagery: Applications to the geosciences. Comput. Geosci. 27 (2001) 381–400.

46. Dierick, M., Cnudde, V., Masschaele, B., Vlassenbroeck, J., Van Hoorebeke, L., Jacobs, P. Micro-CT of fossils preserved in amber. Nucl. Instrum. Methods Phys. Res. 580 (2007) 641–643.

47. Selden, P.A., Penney, D. Imaging techniques in the study of fossil spiders. Earth-Sci. Rev. 166 (2017) 111–131.

48. Voltolini, M., Zandomeneghi, D., Mancini, L., Polacci, M. Texture analysis of volcanic rock samples: Quantitative study of crystals and vesicles shape preferred orientation from X-ray microtomography data. J. Volcanol. Geotherm. Res. 202 (2011) 83–95.

49. Bauer, B., Cai, X., Peth, S., Schladitz, K., Steidl, G. Variational-based segmentation of bio-pores in tomographic images. Comput. Geosci. 98 (2017) 1–8.

50. Brun, F., Mancini, L., Kasae, P., Favretto, S., Dreossi, D. Tromba, G. Pore3D: A software library for quantitative analysis of porous media. Nucl. Instrum. Methods Phys. Res. 615 (2010) 326–332.

51. Yin, X.-Z., Wu, L., Li, Y., Guo, T., Li, H.-Y., Xiao, T.-Q., York, P., Nangia, A., Gui, S.-Y., Zhang, J.-W. Visualization and quantification of deformation behavior of clopidogrel bisulfate polymorphs during tableting. Sci. Rep. 6 (2016) 21770. https://doi.org/10.1038/srep21770.

52. Lindahl, A., Pikirayi, I. Ceramics and change: An overview of pottery production techniques in northern South Africa and eastern Zimbabwe during the first and second millennium AD. Archaeol. Anthr. Sci. 2 (2010) 133–149. https://doi.org/10.1007/s12520-010-0031-2.

53. Morzadec, H. Petro-archeologie des ceramiques armoricaines du neolithique a la fin de l'age du fer, Thèse de doctorat en Archéologie et archéométrie, Université de Rennes, Rennes, France (1993).

54. Quinn, P.S., Burton, M.M., Broughton, D., van Heymbeeck, S. Deciphering compositional patterning in plain ware ceramics from late prehistoric hunter-gatherer sites in the peninsular ranges, San Diego county, California. Am. Antiq. 78 (2013) 779–789.

55. Quinn, P.S.; Burton, M.M. Ceramic distribution, migration and cultural interaction among late prehistoric (ca. 1300–200 B.P.) hunter-gatherers in the San Diego region, Southern California. J. Archaeol. Sci. Rep. 5 (2016) 285–295. https://doi.org/10.1016/j.jasrep.2015.11.022.

56. Sobott, R., Bente, K., Kittel, M. Comparative porosity measurements on ceramic materials. Old Potter's Alm. 2014, 19, 18–25, https://doi.org/10.11588/opa.2014.1.14853.

57. Reedy, C.L., Anderson, J., Reedy, T.J., Liu, Y. Image analysis in quantitative particle studies of archaeological ceramic thin sections. Adv. Archaeol. Pract. 2 (2014) 252–268, https://doi.org/10.7183/2326-3768.2.4.252.

58. Livingood, P.C., Cordell, A.S. Point/counter point: The accuracy and feasibility of digital image techniques in the analysis of ceramic thin sections. J. Archaeol. Sci. 36 (2009) 867–872. https://doi.org/10.1016/j.jas.2008.11.015.

59. Courty, M., Roux, V. Identification of wheel throwing on the basis of ceramic surface features and microfabrics. J. Archaeol. Sci. 22 (1995) 17–50. https://doi.org/10.1016/S0305-4403(95)80161-8.

60. Roux, V., Courty, M.A. Identification of wheel-fashioning methods: Technological analysis of 4th-3rd Millennium BC oriental ceramics. J. Archaeol. Sci. 25 (1998) 747–763. https://doi.org/10.1006/jasc.1997.0219.

61. Carr, C. Advances in ceramic radiography and analysis: Applications and potentials. J. Archaeol. Sci. 17 (1990) 13–34. https://doi.org/10.1016/0305-4403(90)90013-U.

62. Kozatsas, J., Kotsakis, K., Sagris, D., David, K. Inside out: Assessing pottery forming techniques with micro-CT scanning. An example from Middle Neolithic Thessaly. J. Archaeol. Sci. 100 (2018) 102–119. https://doi.org/10.1016/j.jas.2018.10.007.

63. Gomart, L., Weiner, A., Gabriele, M., Durrenmath, G., Sorin, S., Angeli, L., Colombo, M., Fabbri, C., Maggi, R., Panelli, C. Spiralled patchwork in pottery manufacture and the introduction of farming to Southern Europe. Antiq. 91 (2017) 1501–1514.

64. Berg, I. Looking through pots: Recent advances in ceramics X-radiography. J. Archaeol. Sci. 35 (2008) 1177–1188.

65. Kahl, W.-A., Ramminger, B. Non-destructive fabric analysis of prehistoric pottery using high-resolution X-ray microtomography: A pilot study on the late Mesolithic to Neolithic site Hamburg-Boberg. J. Archaeol. Sci. 39 (2012) 2206–2219.

66. Cultrone, G., Sebastián, E., Elert, K., de la Torre, M.J., Cazalla, O., Rodriguez-Navarro, C. Influence of mineralogy and firing temperature on the porosity of bricks. J. Eur. Ceram. Soc. 24 (2004) 547–564. https://doi.org/10.1016/S0955-2219(03)00249-8.

67. Rathossi, C., Pontikes, Y. Effect of firing temperature and atmosphere on ceramics made of NW Peloponnese clay sediments: Part II. Chemistry of pyrometamorphic minerals and comparison with ancient ceramics. J. Eur. Ceram. Soc. 30 (2010) 1853–1866. https://doi.org/10.1016/j.jeurceramsoc.2010.02.002.

68. Diamond, S. Physical and chemical characteristics of cement composites. In: Page, C.L., Page, M.M. (Eds.), Durability of Concrete and Cement Composites, Woodhead Publishing: Cambridge (2007) pp. 10-44.

69. Sevinç, I., Sarikaya, Y., Akinc, M., Sarıkaya, Y. Adsorption characteristics of alumina powders produced by emulsion evaporation. Ceram. Int. 17 (1991) 1–4. https://doi.org/10.1016/0272-8842(91)90002-H.

70. Velde, B., Druc, I.C. Archaeological Ceramic Materials, Springer: Berlin/Heidelberg (1999).

71. Velde, B. Use of image analysis in determining multi-source ceramic materials. In Smith, A.L., Bosquet, D., Martineau, R. (Eds.), Pottery Manufacturing Processes: Reconstitution and Interpretation, Archaeopress: Oxford (2005) pp. 95–99.

72. Whitbread, I.K. Image and data processing in ceramic petrology. In: Middleton, A., Freestone, I. (Eds.), Recent Developments in Ceramic Petrology, British Museum Press: London, British Museum Occasional Paper 81 (1991) pp. 369–388.

73. Albero Santacreu, D.J., Cau Ontiveros, M.Á. Technological choices in hand-made indigenous pottery from Western Mallorca (Balearic Islands, Spain) (C.1200–75 bc): An archaeometric approach. Archaeometry 59 (2017) 642–666.

74. Lechtman, H. Style in technology: Some early thoughts. In: Lechtman, H., Merrill, R.S. (Eds.), Material Culture: Style, Organization and Dynamics of Technology, West Publishing Company: St. Paul, MN (1977) pp. 3–20.

75. Pfaffenberger, B. Social anthropology of technology. Annu. Rev. Anthropol. 21 (1992) 491–516.

76. Gosselain, O.P. Social and technical identity in a clay crystal ball. In: Stark, M.T. (Ed.), The Archaeology of Social Boundaries. Smithsonian Institution Scholarly Press: Washington, DC, USA, London (1998) pp. 78–106.

77. Albero Santacreu, D. Materiality, Techniques and Society in Pottery Production, De Gruyter: Berlin (2014). https://doi.org/10.2478/9783110410204.

Chapter 2. Archaeological sites

2.1. Research history in the North Caucasus (Bronze/Iron Age)

Caucasus is one of the culturally and geographically most complex regions of the Eurasian continent. Since it locates in the communication and trade routes between the north, south, east and west [1], this region has been influenced by different cultural groups from the outside. The main region of this study, the Kislovodsk basin is also one of such strategic points which lies on a route via the 2242 m high Gumbaši pass across the Upper Kuban River towards the Black Sea [2].

Since last decades archaeological excavations and surveys have been carried out intensively in this basin. In the numerous finds from these expeditions, pottery takes an important role playing a marker of identity, tradition, utility and eating habits. In the meanwhile, production technology integrated into the pottery production is less studied. It has the potential to give insight into various relations between human practice and distribution of material culture [3]. As an important parameter for this relationship, technical elements for the production are often termed as technological style [4-6]. Recent research shows that, in certain contexts, decorative style may be less indicative of human practice than are technological traditions [7-9]. According to ethnoarchaeologists, the relationship between diversity of production technology and social contexts appears more complex due to the influence of local communities, social boundaries, tribal entities or mobility patterns on the pottery production [10].

The archaeological research in the North Caucasus has concentrated traditionally on the uncovering of graves, not so many settlements are known in this region. [11]. However, Kislovodsk is archaeologically one of the specific sites where systematic landscape archaeological investigations using GIS (Geographic Information System) technologies have been carried out [12], with an investigation of the settlements and spatial structures under a diachronic perspective. Under the conduction of the Institute of Archaeology of the Russian Academy of Sciences, more than 400 sites have been discovered in the recent years in the course of surveys from 2004 to 2010 [13]. Since 2011 archaeological excavations were carried out in the new type of grave fields and settlement structures identified by aerial photographs. Geological mapping was carried for the information on the location of igneous and metamorphic rocks in the central Caucasian highlands and other sediment types and metal sources. Soil samples were studied by phosphate, magnetic, chemical and micro-bacteriological analysis, too [14]. These researches including archaeological expeditions were carried out the Project Kislovodsk, North Caucasus, a joint project of the Institute of Archaeology, Russian Academy of Sciences (D.S. Korobov), the Eurasian Department of the Deutsches Archäologisches Institut (DAI, S. Reinhold) and GUP Nasledie, the Ministry of Culture of the Stavropol Region, Russia (A.B. Belinsky). According to the chronology in the North Caucasus suggested by Reinhold, the Middle Bronze Age is equivalent to the North Caucasus Culture, the Late Bronze Age to Koban A and the Early Iron Age to Koban B/C [15]. The Late Bronze Age is represented by the settlement sites at Kabardinka. The excavation at Ransyrt in 2015 which is date back to 1700 BC by now, shows characteristics not only of the Late Bronze Age but of the Middle

Bronze Age, too. However, the question whether these settlements were occupied permanently or seasonally still remains unsolved.

Parallel to the excavations and surveys by the Kislovodsk Project, the archaeological, morphological typology and decoration of the ceramic finds from the Late Bronze – and the Early Iron Age in the whole Caucasus were investigated as a cultural and regional marker. In general, 16 types of vessels from various archaeological contexts (settlements, graves and grave fields, depots, surveys) are defined with regard to shape and size, informing regional and interregional tradition of ceramic production in the Caucasus [15]. Three general types in decoration motives (band, metope, plastic relief) normally with 20 - 30 variations occur at various contexts, too. Especially, settlements at Kabardinka 2 yield most of those motives. From the macroscopic observation specific evidence in working techniques is offered. Trace of a potter's wheel (wheel-shaped) often appears in the southern part of the Caucasian Mountains like South Ossetia and Abkhazia during the Late Bronze- and the Early Iron Age, while the most vessels from the northern part seem to be hand-made. Further, forming of the inner surface of the ceramics with textiles, the general firing temperature in a lower range, polishing for the surface treatment or use of organic temper materials at the archaeological sites were reported.

2.2. Cultural historical background of the archaeological materials

The time span of this doctoral research lies mainly between the Late Bronze – and the Early Iron Age, according to the regional chronology, from Koban A to Koban C1/C2 [15-16] (Figure 2-1). In this time span, regional archaeological finds consisting of accessories, weapons and ceramic/metal vessels appear in the various contexts of the Kislovodsk basin, indicating rapid economic development.

In the Late Bronze Age (Koban A) there was a fundamental change in groups of the whole Caucasus and development of archaeological unities, above all the Koban Culture in the central Mountains [17], because pre-existing Caucasian mobile groups became sedentary and were split into smaller regional units formatting of regional identities in the process [15]. This is indicated by changes in building layouts and construction materials for a permanent habitation [16,18]. This change also appears in the regional archaeological culture presented by new types of material objects, changed burial customs and expansion of metallurgy with tin-bronze. A clear increase in the number of settlements based on small villages, graves and grave fields [19] could stimulate development of social networks and -interaction within smaller regional groups. This change would cause to various village-based development and transfer of technological practice and style in pottery making. Identified building structures (line-form, oval/ring-form layout, symmetrical ground plan which looks like a closed ring, combination of symmetrical layout and curved line-form or wall arrangement) from the North Caucasus in the Late Bronze Age discovered by aerial photos [16] would provide more detailed indication of social relations inter- and intra-regional groups. The settlements at Kabardinka 2 shows various space concepts for a house and layout, for example, 1-3 rooms in a quadratic ground plan, a monumental entrance, a big room with a large central post or a symmetrical layout [2,16] providing possible patterns of social

contacts between inhabitants. At Ransyrt related to the Middle and Late Bronze Age, a stone architecture, probably an ancient sanctuary due to huge amounts of finds from the expedition in 2015, would offer chances for social contacts and networks in the region. The location of this site can be interpreted as an important trade route across the mountains, too [15].

In the Early Iron Age (Koban B-C) the characteristics of the Koban culture from the Late Bronze Age appear further in the settlement pattern, social organization or complex metal handicraft [20]. The motives from the period of Koban B1 occur in every settlement from this period [15]. At Verchnaja-Podkumok, a pit type settlement which was common in the Early Iron Age is identified by the stratigraphy, indicating different type of possible social relations of the inhabitants. In spite of these phases for development of permanent settlements in various regions, changes of the settlement area and cultural space are still observed in the Late Bronze- and the Early Iron Age [15], which influences on variability of production technology and material culture.

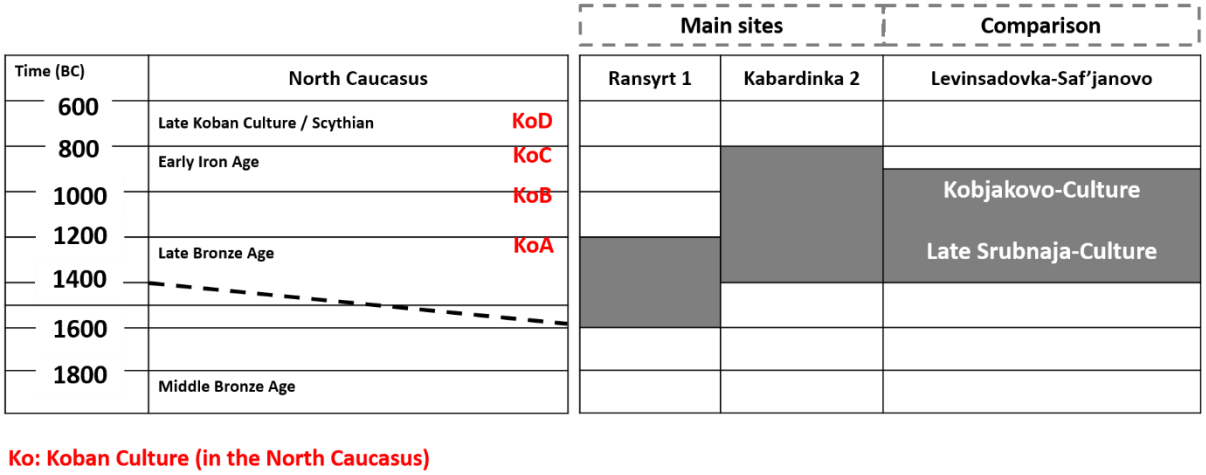

Table 2-1. Chronology of the North Caucasus (according to *Reinhold et al.* [15]).

2.3. The main archaeological sites of this study: Ransyrt 1 and Kabardinka 2

Figure 2-1 describes the archaeological sites of this study. Ransyrt 1 is located on the plateau with the height of 1850 m above sea level in Karachay-Cherkess Republic of the Russian Federation (43°50'29.7"N, 42°18'10.3"E). Kabardinka 2 lies on the lower plateau with 1400 m a.s.l. in Stavropol Krai of the Russian Federation (43°49'40.9"N, 42°42'57.4"E). The objects were excavated by the joint project of German Archaeological Institute (S. Reinhold), the Institute of Archaeology, Russian Academy of Sciences (D.S. Korobov) and GUP Nasledie, heritage organization in Stavropol, Russia (A.B. Belinsky) between 2006-2008 and 2013-2015. According to the local chronology defined by the construction phases and ^{14}C data, Ransyrt 1 is dated to 1800-1500 BC, the Middle Bronze Age (MBA) to the Late Bronze Age (LBA) and Kabardinka 2 to 1600-800 BC, which belong to the LBA and Early Iron Age (EIA) [16]. Especially Kabardinka 2 has relatively longer occupation history proved by two different construction phases, i.e., a linear phase between 1600-1200 BC and a symmetric phase between 1300-800 BC. In this time period, Koban culture was known in the North Caucasus region[7]. Geologically,

Ransyrt 1 bedrock is composed of dolomite, while the bedrock of Kabardinka 2 is mainly composed of calcite. Soil development of Kabardinka 2 is more progressed than Ransyrt 1.

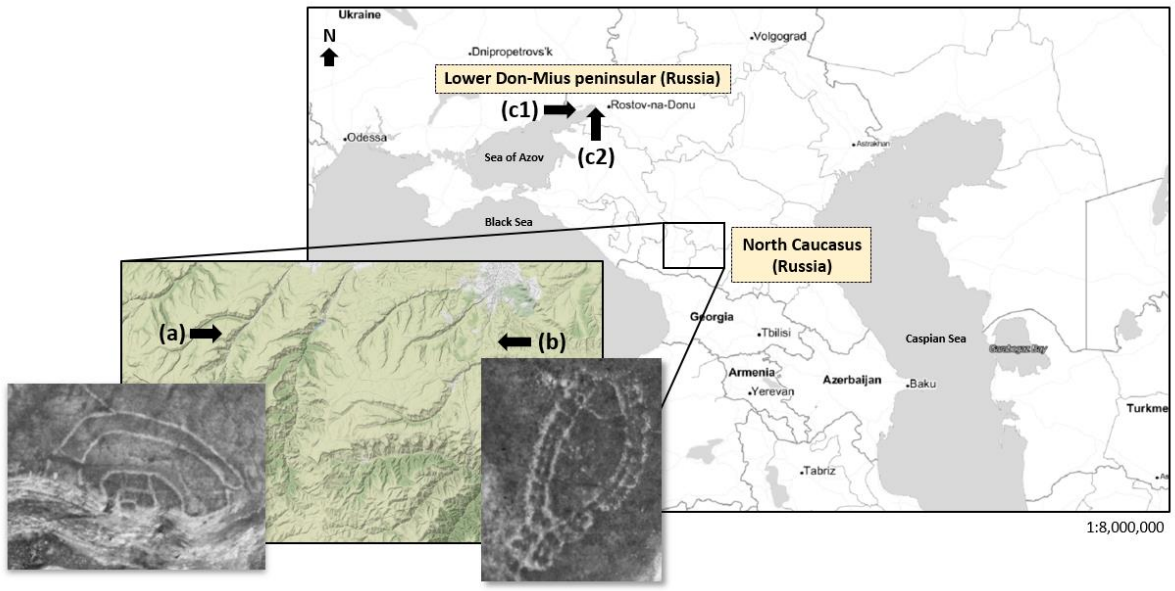

Figure 2-1. Archaeological sites in North Caucasus and in the Sea of Azov: (a) Ransyrt 1; (b) Kabardinka 2; (c1) Levinsadovka (Mius peninsular); (c2) Saf'janovo (Lower Don) (maps: created by QGIS 2.18.0 with open layers from OSM/Stamen, map tiles by Stamen Design, under CC BY 3.0. data by OpenStreetMap, under ODbL (maps.stamen.com); photos: *Reinhold et al.* [16]).

2.4. The sites for the comparison: Levinsadovka and Saf'janovo

These mountain ceramics were compared to the other archaeological ceramics from Levinsadovka (47°10′9.9"N, 38°30.17"E) and Saf'janovo (47°15′59.7"N, 39°26′30.1"E), located on the coast of Mius peninsular and on the lower area of the Don river. They were excavated by another joint project of the German Archaeological Institute, Don-Archaeological Society (Rostov on Don) and Institute of Archaeology, Russian Academy of Sciences. The site at Levinsadovka on the Mius peninsular was occupied by the Late Srubnaja Culture (LBA) and that at Saf'janovo by Kobjakovo Culture (Final Bronze Age, FBA) [21]. Corresponding to the radio carbon data, the both cultures were overlapping between 1600-800 BC.

2.5. References

1. Halbach, U., Kappeler, A. (Eds.) Krisenherd Kaukasus, Nomos-Verl.-Ges.: Baden-Baden (1995).

2. Reinhold, S., Korobov, D.S. Neu entdeckte früheisenzeitliche Siedlungslandschaften im Nordkaukasus. In: Trebsche, P., Balzer, I., Eggl, Ch., Koch, J., Nortmann, H., Wiethold, J. (Eds.), Die unteren Zehntausend, Beiträge zur Ur- und Frühgeschichte Mitteleuropas 47, Beier & Beran 2007: Langenweissbach (2007) pp. 139-148.

3. Dietler, M., Herbich, I. Habitus, techniques, style: An integrated approach to the social understanding of material culture and boundaries. In: Stark, M.T. (Ed.), The archaeology of social boundaries, Smithsonian Institution Press: Washington and London (1998) pp. 232-263.

4. Gosselain, O.P. Social and technical identity in a clay crystal ball. In: Stark, M.T. (Ed.), The archaeology of social boundaries, Smithsonian Institution Press: Washington and London (1998) pp. 78-106.
5. Herbich, I. Learning patterns, potter interaction and ceramic style among the Luo of Kenya, The African Archaeological Review 5 (1987) 193-204.
6. Pfaffenberger, B. Social anthropology of technology, Annual Review of Anthropology 21 (1992) 491-516.
7. Childs, S.T. Style, technology and iron smelting furnaces in Bantu speaking Africa, J. Anthropol. Archaeol. 10 (1991) 332-359.
8. Chilton, E.S. The cultural origins of technical choice: Unraveling Algonquian and Iroquoian Ceramic Traditions in the Northeast. In: Stark, M.T. (Ed.), The archaeology of social boundaries, Smithsonian Institution Press: Washington and London (1998) pp. 132-160.
9. Dietler, M., Herbich, I. Tich Matek: The technology of Luo pottery production and the definition of ceramic style, World Archaeology 21 (1989) 148-164.
10. Goodby, R.G. Technological patterning and social boundaries: Ceramic variability in Southern New England, A.D. 1000-1675. In: Stark, M.T. (Ed.), The archaeology of social boundaries, Smithsonian Institution Press: Washington and London (1998) pp. 161-182.
11. Абрамова, М.П. О некоторых спорных вопросах хронтогии раннесарматской культуры. In: Евразийские Древности. 100 лет В. Н. Гракову, Москва (1999) pp. 98-107.
12. Афанасьев, Г.Е., Савенко, С.Н., Коробов, Д.С. Древности Кисловодской котловины. Москва. (2004).
13. Reinhold, S. Kislovodsk, Russische Förderation, Spätbronzezeitliche Fundplätze im kaukasischen Hochgebirge. In: Deutsches Archäologisches Institut (Ed.), e-Forschungsberichte des Deutschen Archäologischen Instituts 2014, Faszikel 2, eDAI-F 2014-2, (2014) pp. 82-88.
14. Peters, S., Borisov, A.V., Reinhold, S., Korobov, D.S., Thiemeyer, H. Microbial characteristics of soils depending on the human impact on archaeological sites in the Northern Caucasus. Quat. Int. 324 (2014) 162-171.
15. Reinhold, S. Die Spätbronze- und frühe Eisenzeit im Kaukasus: materielle Kultur, Chronologie und überregionale Beziehungen. Universitätsforschungen zur prähistorischen Archäologie 144, Habelt R.: Bonn (2007).
16. Reinhold, S., Korobov, D. S., Belinskij, A. B. Landschaftsarchäologie im Nordkaukasus. Habelt. R.: Bonn (2018).
17. Козенкова, В.И. Кобанская культура: Субстрат и инновации в период формирования (последняя четверть 2 тыс. до н.э.). In: Междисциплинарные исследования культурногенеза Армянского нагорья и сопредельных областей, Ереван (1990b) pp 184-291.
18. Reinhold, S. Rund oder eckig? Überlegungen zu prähistorischen Siedlungen mit Rundemund ovalem Grundriss. In: Trebsche P., Müller-Scheeßel, N., Reinhold, S. (Eds.), Der gebaute Raum, Tübinger

Archäologische Taschenbücher 7, Waxmann-Verlag: Münster, New York, München, Berlin (2010) pp. 213-234.

19. Badylyan, R., Smith, A.T., Avetisyan, P.S. The Emergence of sociopolitical complexity in Southern Caucasia: An Interrim Report on the Research of Project ArAGATS. In: Smith, A.T., Rubinson, K. (Eds.), Archaeology in ten border lands, investigation in the Caucasus and beyond, University of Exeter Press: Los Angeles (2003) pp. 114-166.

20. Козенкова, В.И. Козенкова, Культурно-исторические процессы на Северном Кавказе в эпоху поздней бронзы и раннем железном веке (Узловые проблемы происхождения и развития кобанской культуры), Москва (1996).

21. Dally, O., van Hoof, L., Huy, S., Il´jaschenko, S., Larenok, P. A., Larenok, V. A., Schlöffel, M., Schunke, T., Schütt, B. Deutsch-russische Ausgrabungen am Don. Ergebnisse der Kampagnen 2008–2010. Archäologischer Anzeiger 2012/1 (2012) 139–205.

Chapter 3. Materials and methods

3.1. Materials

The archeological survey and excavations at Ransyrt 1 in 2013 and 2015 yielded 50,000-60,000 ceramic sherds and 10,000 ceramics were reported from the excavations at Kabardinka 2 in 2007 and 2008. These sherds were classified by optical investigations according to the color, texture, size and minerals. Finally, 80 samples for Ransyrt 1 and 70 for Kabardinka 2 were selected respectively. They represent ceramics with a different texture, color, cross section profile, size and minerals exposed to the surface qualitatively in macroscale. In order to compare to the mountain ceramics, 21 ceramic samples from Levinsadovka and Saf'janovo in the coast of Sea of Azov were investigated as well.

3.2. Methods: General description

In order to clarify the resource gathering strategy, firing and shaping techniques in the ceramic pottery production at each site, samples were analyzed by various instruments and methods according to the purpose of each topic. As heterogenous composite material, archaeological ceramics contain various structural and compositional elements. This makes it difficult to determine and to measure the proper elements according to the study. Above all, most ceramics are sampled and investigated based on the huge amounts of the excavated sherds, in order to answer the socio-technical and socio-economic questions about the previous societies. From these reasons, this study employed multiproxy and multiscale approach combining step-by-step, scale-up procedure and analysis in various observation scales for the topics (Figure 3-1).

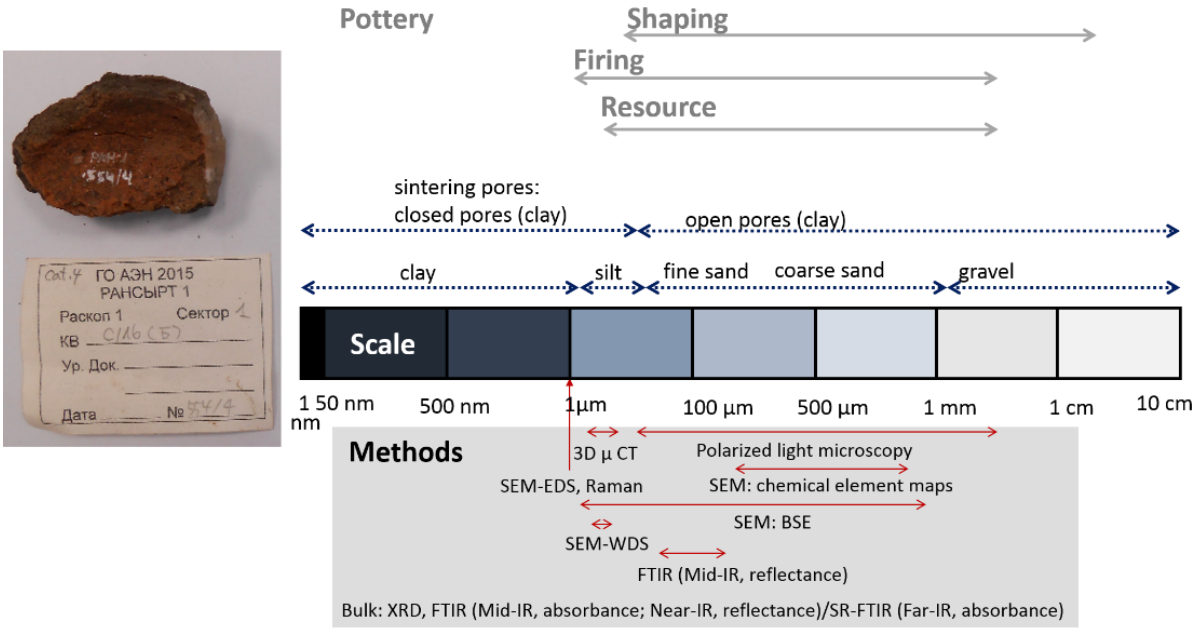

Figure 3-1. Example of a ceramic sherd with the sample name and the scheme of the multiproxy- and multiscale approach of this project (photo by the author).

In general, polarized light microscopy (PM), Scanning electron microscopy with wavelength-dispersive spectroscopy (SEM/SEM-WDS) and X-ray powder diffraction (XRD), Fourier transform infrared

spectroscopy (FTIR, absorbance and reflectance), Synchrotron (SR)-FTIR (absorbance) and image analysis using PM and three dimensional micro computed tomography (3D µ-CT) were employed for the characterization of the ceramic pastes. Shaping techniques were studied mainly by PM and 3D µ-CT, focusing on the inner structure formation. Firing techniques were investigated by the combination of SEM/SEM-Maps, XRD, FTIR/SR-FTIR (absorbance and reflectance) and Raman spectroscopy, image analysis using PM and 3D µ-CT.

In this chapter, general features and working principles of each analytical instrument are briefly presented. The details of the measurements for this project follow in the second part.

3.2.1. Polarization light microscopy (PM)

By PM on the polished thin section, mineralogy of grains and size distribution of ceramic pastes upon firing can be estimated. Textural changes of pastes indicate the degree of water loss, deformation, shapes and orientation of pores and orientation of temper materials, distribution of density of the ceramic paste. Optical characteristics such as interference color and pleochroism, light refraction, double refraction and extinction positions in birefringent crystal sections are necessary to identify and distinguish various phases within ceramics. This instrument is employed for every subtopic in this study to get basic information.

3.2.2. Scanning electron microscopy with energy/wavelength-dispersive spectroscopy (SEM/SEM-EDS/WDS)

SEM provides information about surface topography, crystalline structure, chemical composition and electrical behavior. The electrons penetrate the specimen in a teardrop-shaped volume whose overall dimensions are determined by the energy of the electron beam, the atomic masses of elements in the specimen and the angle at which the electron beam hits the specimen (Figure 3-2) [1]. The penetration depth increases with higher electron-beam energy, incidence angle and lighter atomic mass. From the electrons produced by the interaction of the electron beam with the specimen, secondary electrons and backscattered electrons in various signals from the specimen are mostly collected for imaging.

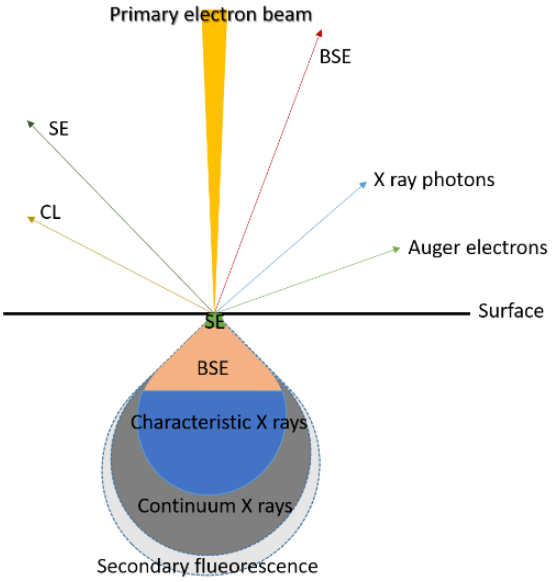

Figure 3-2. Interaction of highly energetic electrons (electron beam) with specimen (SE: secondary electron; BSE: back scattered electron; CL: cathodoluminescence).

Secondary electrons (SE) provide the highest spatial resolution images, as they can only escape from a

very shallow, near-surface layer of material and the signal comes from an area about the size of the electron probe. Backscattered electron (BSE) are those incident electrons that approach the nucleus of an atom sufficiently closely to be scattered through a large angle and reemerge from the surface. In BSE, elements of higher atomic mass give brighter contrast indicating compositional information.

In the ceramic research, detailed empirical knowledge on the behavior of materials of the potter and control of firing are acquired by the micro-mineralogy and morphology of the grains and pores in a high spatial resolution of BSE images. Chemical composition and its exchange between different phases in the samples can be measured semi-quantitatively/quantitatively for the specific points in the micrometer dimension by EDS/WDS. Other parameters imprinted by pyrotechnical practice are to extract from mineralogical reactions and morphological observations as well.

3.2.3. X-ray powder diffraction (XRD)

X-ray diffraction is the elastic scattering of x-ray photons by atoms in a periodic lattice [2]. The scattered monochromatic x-rays that are in phase give constructive interference. The Bragg's law allows to derive lattice spacings using x-rays by crystal planes [3-4],

$$n\lambda=2d\sin\theta \quad (3\text{-}1)$$

where n is an integer explaining the order of reflection, λ is the wavelength of X-rays, d is the characteristic spacing between the crystal planes of a given specimen and θ is the angle between the incident beam and the normal to the reflecting lattice plane (Figure 3-3). Using x-ray diffraction studies, the structures of crystals and molecules are often being identified.

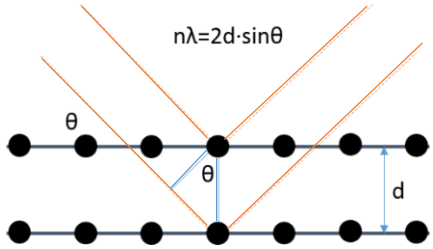

Figure 3-3. Bragg's law.

3.2.4. Fourier transform infrared spectroscopy (FTIR), synchrotron radiation Fourier transform infrared (SR-FTIR)

IR spectroscopy is an important and popular tool for structural clarification and compound identification in the sample and is even a common spectroscopic technique used for quantitative determination of compounds in mixtures.

In polyatomic molecules, vibrations store nearly all of the chemically available energy. The total number of those coordinates is $3N_{atom}$, for motion along the three Cartesian coordinates of each of the N_{atom} atoms in the molecule, translations, rotations, and vibrations [5]. Three translational coordinates account for motion of the center of mass along x,y,z and three rotational coordinates for θ and ϕ to specify the orientation of any given bond axis and a third angle of rotation about that bond if the molecule is nonlinear. The other coordinates of $3N_{atom}$-6 are vibrations (Figure 3-4). Corresponding energy from the absorbed infrared radiation is converted into different types of motions. However, the individual

vibrational motion is usually accompanied by other rotational motions. These combinations lead to the absorption bands, not the discrete lines, commonly observed in the middle IR regions.

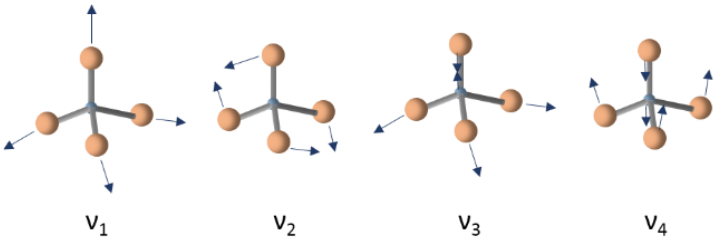

Figure 3-4. Normal modes of vibration of a tetrahedral TO_4 group. ν_1 and ν_3, represent the symmetric and asymmetric stretching modes, respectively, ν_2 and ν_4 the corresponding bending vibrations.

Figure 3-5 describes the principle of the specular reflection and transmission. Transmittance is the ratio of radiant power transmitted by the sample (I) to the radiant power incident on the sample (I_o). Absorbance is the logarithm to the base 10 of the reciprocal of the transmittance (T), $A=\log(T^{-1}) = -\log(I/I_o)$. Transmittance ranges from 0 to 100% Z whereas absorbance ranges from infinity to zero. Optical reflection spectroscopy in the IR permits in situ applications, and result in quantitative and structural information on a molecular level. There is a wide range of different spectroscopic reflection techniques distinguishing internal (total) and external reflection: Attenuated total reflection/internal reflection spectroscopy (ATR), diffuse reflectance, specular reflection spectroscopy (SRS), reflection absorption spectroscopy (RAS).

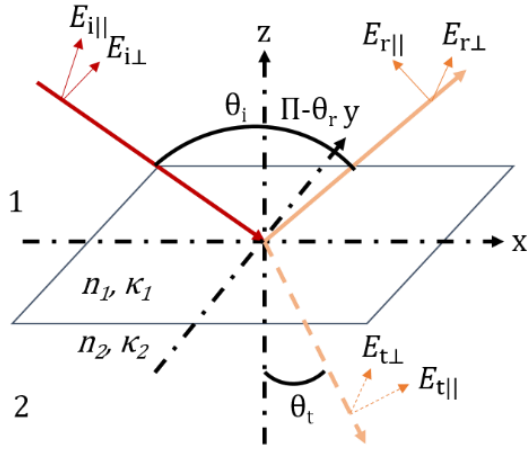

Figure 3-5. Specular reflection and transmission [6]**. The angles of incidence (i), reflection (r) and refraction (t) are denoted by θ_i, θ_r, θ_t, respectively. The corresponding electric field components are denoted by *E*. They are split into orthogonal portions. One parallel to the plane of incidence (x, z-plane) and the other perpendicular to this plane (parallel to y-axis). Accordingly, electric fields are referred to as parallel and perpendicular polarized n_1, n_2, κ_1, κ_2 denote the refractive and absorption indices in the two media.**

Synchrotron-radiation (SR) enables the higher spectral, spatial resolution and higher intensity in mid-Infrared (MIR) and far-Infrared (FIR)/THz than other sources. The IRIS beamline at Bessy II, Helmholtz Zentrum Berlin (HZB) uses radiation from the homogenous magnetic field of the dipole and its optical layout [7-8]. The energy range lies between 2 and 10,000 cm^{-1} and its resolution is 0.125 cm^{-1}. The beam polarization is linearly horizontal/vertical and circularly left- and right-handed.

3.2.5. Raman spectroscopy

Raman spectroscopy provides information about chemical structure, phase and polymorphism, crystallinity and molecular interactions. Raman techniques uses a molecule scattering by incident light from a high intensity laser light source, which is called Raman scattering (Figure 3-6). This is different from Rayleigh scattering containing same wavelength. This measurement has been used for the detection and characterization of the vitreous phase.

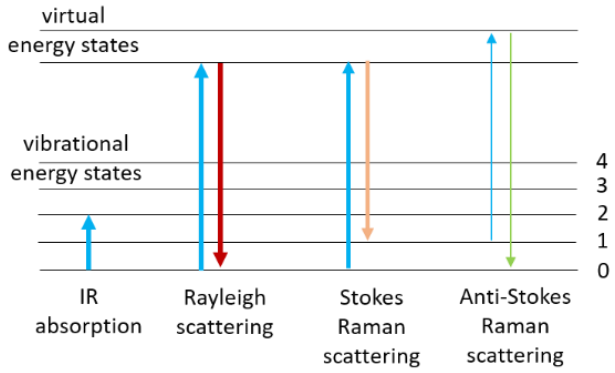

Figure 3-6. Energy-level diagram showing the states involved in Raman spectra.

3.2.6. Three dimensional micro computed tomography (3D μ-CT)

CT provides nondestructive three-dimensional visualization and characterization, creating images that map the variation of X-ray attenuation within objects, which relates closely to density (Figure 3-7). Because density transitions usually correspond to boundaries between materials or phases, these data are often straightforward [10-11]. The important variables in CT are the size of the focal spot, the spectrum of X-ray energies and the X-ray intensity. The focal spot size defines the potential spatial resolution by determining the number of possible source-detector paths. The energy spectrum defines the penetrative ability of the X-rays. The X-ray intensity directly affects the signal-to-noise ratio and thus image clarity. Higher intensities improve the underlying counting statistics, but often require a larger focal spot.

Detectors for CT influence image quality through their size and quantity, and their efficiency in detecting the energy spectrum generated by the source. In the acquisition of CT data, calibrations are necessary to establish the characteristics of the X-ray signal as read by the detectors under scanning conditions, and to reduce geometrical uncertainties. Reconstruction converts sonograms from each acquisition angle into stacks of two-dimensional slice images.

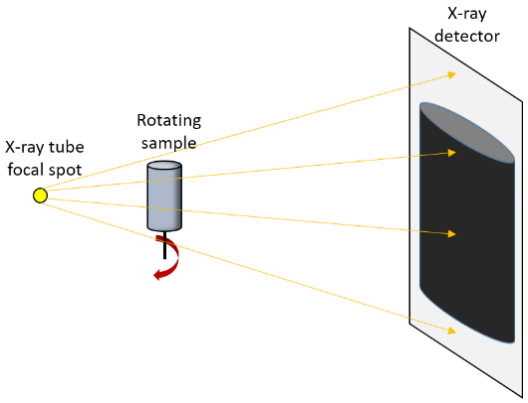

Figure 3-7. Schematic diagram of a typical lab-based micro CT setup with a conical X-ray beam which allows geometric magnification.

3.3. Methods in this study

3.3.1. Identification of the ceramic pastes

The mineralogical composition of grains in various sizes within the ceramic pastes was investigated by various analytical methods such as polarized light microscopy, XRD, SEM-EDS/WDS. First, XRD patterns of the whole 158 samples were collected by the diffractometer, Empyrean by PANalytical in

the measuring conditions of Cu Kα radiation (λ=1.542 Å), 40 kV, 40 mA, 2θ range between 3-60 °, 0.013 ° for the 2θ step size and 50 s/step in the rotating mode. The samples were pulverized in a Tungsten mill for 4 minutes after the removal of the altered surface layer and measured without pre-treatment so that the specific peaks from heated clay minerals during ceramic firing can be distinguished from the possible regenerated or newly intruded clays in ceramics. Same samples were prepared for thin cross section with the thickness of 30-35 µm for the polarized light microscopy, too. According to the XRD and petrography results, polished thin sections of 52 representative samples coated with carbon were further investigated by Field emission scanning electron microscope by Zeiss SUPRATM 40 VP Ultra (thermal field emission type) with acceleration voltage 10-15 kV and Oxford Instruments EDX-System to identify minerals. BSE images were taken with an aperture size of 120 µm. For the supplement, SEM-EDS, JEOL JXA 8200 Superprobe with 15 kV acceleration voltage were employed, too.

In order to identify the dominant clay mineral in the original ceramic pastes, FTIR transmittance measurements (Paragon 1000 PC by Perkin Elmer) were performed for supporting XRD data from above. 34 samples which contain less deformed structures were selected from 158 samples. 2-4 mg powder from each sample was mixed with KBr, pelletized and dried at 170 °C for 60 hours, in order to reduce the water amount adsorbed to pastes. After the dehydration, the samples were measured with 128 scans and 2 cm^{-1} spectral resolution between 450 and 4000 cm^{-1}. Due to the higher noise ratio in 3000-4000 cm^{-1}, it was necessary to apply the Savitzky-Golay filter with number of 13 points, in order to show the main clay phases clearly.

FIR spectra were acquired using infrared synchrotron radiation from the IRIS beamline [8,12] at the third-generation electron storage ring BESSY II of the Helmholtz-Zentrum Berlin and a vacuum Fourier-Transform spectrometer Bruker 70/v and a liquid helium cooled Si-bolometer as detector. To measure the absorption spectra the powder sample material was compressed by diamond compression cell of an aperture size of 1 mm^2. Spectra ranging between 20 and 550 cm^{-1} were acquired by co-adding again 128 scans with a spectral resolution of 4 cm^{-1}.

NIR reflectance spectra of powdered samples for have been obtained between 3000 and 12000 cm^{-1} by diffuse reflectance infrared Fourier transform spectroscopy (DRIFTS) with a spectral resolution of 16 cm^{-1} in a Bruker 80/v FTIR spectrometer utilizing a tungsten bulb as source, a CaF_2 beam splitter and a N_2-cooled InSb detector. The sample were placed in small cups and placed in a Seagull™ Variable Angle Reflection Accessory (Harrick Scientific). Measurements were done at a 20 ° angle of incidence and reflection. Before measuring the sample surface was leveled according to the cup rim. Spectralon was taken as a reflectance reference. 128 spectra of three different sample areas were co-added and averaged.

The chemical composition of the ceramic matrix was measured by SEM-WDS, JEOL JXA 8200 Superprobe using 5 crystal spectrometers for the major earth elements in an oxidized form and weight % (Na_2O, BaO, FeO/Fe_2O_3, MgO, CaO, MnO, Al_2O_3, K_2O, TiO_2, SiO_2, P_2O_5). The 52 polished thin

sections from above were selected. Due to the porosity and (crystal-)water content in the ceramics, the total amount in weight % is normalized to 100.

In order to characterize sand grains in the ceramics, two-dimensional polarized light micrographs were acquired with a pixel size of 3.27^2 and 10^2 µm^2 for the total area of the cross thin sections. The images by the plane polarized light were used for the analysis and those by the cross polarized light for the comparison and confirmation of the components. 17 samples for Ransyrt 1 and 20 samples for Kabardinka 2 were measured for the identification.

The 3D image processing of sand grains was performed for selected samples using the 3D µ-CT (nanotom 180NF, GE phoenixIx-ray) with tube voltage and current of 140 kV and 96 µA, respectively, so that the differences between the shape parameters calculated from the 2D images and those from the 3D images can be investigated [13]. A total of 1080 images were taken at angular steps of 0.33 degree and with an acquisition time of 1000 msec/image. The voxel size of 9.49^3 µm^3 was determined, in order to compare to the 2D image analysis using 10^2 µm^2 per pixel. Considering the heterogeneity of prehistoric ceramics, the ROI was set for the whole area and volume of the sample. The selected magnification of the sample as well as pixel/voxel size were enough to represent the corresponding sample. The acquired images were reconstructed as a volume file using the phoenix datos|x reconstruction software with a beam hardening correction (BHC) factor 8. Each voxel stored values in a 16-bit integer. An edge enhancement filter was applied for the reconstruction.

3.3.2. Formation of the ceramics

The ceramic formation technique was estimated from the inner structure of 14 samples from Ransyrt 1 and 19 samples from Kabardinka 2 scanned by 3D µ-CT (Table 3-1). The three dimensional alignment of sand grains and large pore complexes existing in the inner structure were taken into considerations for estimating their macroscale formation. Angle, layout and size of those structural elements were investigated in the range of mm to cm, qualitatively. Therefore, the whole ceramic sherd should be within the ROI and this caused a relatively larger voxel size of 9.493–30.273 µm^3. The corresponding condition was set to tube voltages of 102–140 kV, currents of 70–103 µA, acquisition time of 500–1250 msec/image according to the sample. The acquired images were reconstructed by the phoenix datos|x reconstruction software with a BHC factor 8, voxel values in a 16-bit integer and the edge enhancement filter.

For the pore topology, 1080 images were taken. Four images for each angle were gathered and the first two images were skipped. The CT images were reconstructed as a volume using the edge enhancement filter and BHC factor 8.

Sample no.	Voltage (kV)	Current (µA)	Acquisition time (mS)	Magnification	Voxel size (µm^3)
Ran1_278_x	132	102	750	1.687	29.63^3
Ran1_527_20	127	100	750	1.950	25.64^3
Ran1_313_2	131	101	750	1.652	30.27^3
Ran1_538_16	130	100	750	1.656	30.19^3
Ran1_449	127	90	750	2.500	20.00^3

Ran1_619_23	137	99	750	1.897	26.35^3
Ran1_601_7	140	93	1000	1.721	29.05^3
Ran1_514_2	140	96	1000	5.271	9.49^3
Ran1_489_46	140	99	1000	2.586	19.33^3
Ran1_N18_49	132	80	1000	1.674	29.88^3
Ran1_541_11	130	80	1000	1.739	28.75^3
Ran1_167_4	133	70	750	4.857	10.29^3
Ran1_298_3	104	80	750	3.043	16.43^3
Ran1_225_4	104	70	750	2.755	18.15^3
Kab2_1697_1	135	100	750	1.700	29.37^3
Kab2_482_13	130	92	750	2.000	25.00^3
Kab2_1260_4	122	100	750	2.349	21.29^3
Kab2_482_1	110	87	750	2.500	20.00^3
Kab2_1396_4	122	78	500	2.641	18.93^3
Kab2_1763_1	135	103	750	1.951	25.62^3
Kab2_1408_1	114	100	750	2.214	22.58^3
Kab2_1235_1	131	90	750	2.000	25.00^3
Kab2_1195_6	130	79	750	2.000	25.00^3
Kab2_1976_1	139	90	750	1.849	27.04^3
Kab2_650_10	105	80	750	3.539	14.13^3
Kab2_1587_1	140	98	1250	1.977	25.29^3
Kab2_853_1	140	90	1000	2.194	22.79^3
Kab2_2258_5	104	80	750	2.500	20.00^3
Kab2_1253_3	121	70	750	2.480	20.16^3
Kab2_1603_4	125	80	750	2.267	22.06^3
Kab2_416_9	130	70	750	2.000	25.00^3
Kab2_516_26	102	70	750	2.889	17.31^3
Kab2_294_1	131	70	750	2.000	25.00^3

Table 3-1. Measurement condition of the 3D µ-CT for the alignment of the pore complex and sand grains.

3.3.3. Identification of the ceramic firing

Three main analytical methods are employed for the estimation of the firing degree: XRD focusing on the specific peaks of clay minerals, FTIR transmittance and reflectance measurements, micromorphological changes observed in BSE images from SEM.

FTIR measurements were performed with Paragon 1000 PC by Perkin Elmer in transmission mode. For the sample preparation, powder from 116 ceramics selected from 158 samples were mixed with KBr and pelletized. The MIR curve is taken with 128 scans and a spectral resolution of 2 cm^{-1} for wavenumbers between 450 and 4000 cm^{-1}. For this purpose, no smoothing filter was necessary. In order to focus more on the clay matrix within the heterogeneous mixed state of ceramic pastes, an IR-microscope (Bruker Hyperion 2000) attached to a Vertex 80v FTIR-spectrometer and a MCT detector was employed to perform reflectance point analysis on the polished cross thin section of the 52 samples without carbon coating. Our main goal was the observation of Si-O stretching mode located between 900 and 1200 cm^{-1}. The IR aperture size was fixed to 70x70 μm^2, as this size was found to minimize the IR signal of the sand and silt grains and to maximize the signal of clay minerals. We performed 1024 scans with a spectral resolution of 2 cm^{-1}. A silver mirror was used as reference for the IR reflectance experiments. Additional MIR reflectance measurements with a spectral resolution of 2 cm^{-1} have been performed on sample cross sections utilizing a purged infrared microscope Nicolet iN10 and a liquid

nitrogen cooled mercury cadmium telluride (MCT) detector. 128 scans have been co-added. The investigated area on the sample was 70 x 70 μm^2. A gold surface was used as a reference.

FIR spectra and Diffuse NIR reflectance spectra for the estimation of the thermal deformation and transformation degree were acquired with the same setting variables for the identification of the ceramic pastes described in the section 3.3.1.

The degree of high firing ceramics containing glassy phases was estimated from the Raman spectra obtained by a Horiba ISA Dilor Labram micro-confocal Raman spectrometer using the internal 532.15 nm Nd-YAG laser. The spectra were taken with a focal length of 300mm and a slit of 100 µm which yielded a spectral resolution of up to 3.5 cm^{-1}. The acquisition time was 30 seconds and the spectra were accumulated twice.

The pore topology of the ceramic matrix influenced by the firing process was measured by SEM, JEOL JXA 8200 Superprobe with an acceleration voltage of 15 kV for the 2D analysis. The area of 300×300 µm2 was scanned with a pixel size of 12 μm^2, which allowed to capture various types and sizes of pores in the ceramics. In a 2D matrix, BSE images are presented for each pixel of ROI. The 3D porosity was measured by µ-CT with different tube voltages of 103-129 kV and currents of 70-80 µA according to the sample. The acquisition time for 1080 images ranged from 750 to 1000 msec/image and the voxel size from 1.053 to 3.853 μm^3 as well. For the image reconstruction, the BHC factor was set to 9-10, in order to minimize artifact effects. 13 samples for Ransyrt 1 and 15 samples for Kabardinka 2 were measured for the 2D image analysis. Three from these samples were selected for the investigation of the 3D porosity (Table 3-2).

For the pore topology, 1080 images were taken. Four images for each angle were gathered and the first two images were skipped. The CT images were reconstructed as a volume using the edge enhancement filter.

Sample no.	Voltage (kV)	Current (µA)	Acquisition time (mS)	Magnification	Voxel size (μm^3)	BHC
Ran1_329	103	70	750	13.000	3.85^3	9
Ran1_KB3kc1	129	80	1000	14.546	3.44^3	9
Ran1_549_1	109	80	750	13.637	3.67^3	9
	120	80	1000	47.503	1.05^3	10

Table 3-2. Measurement condition of the 3D µ-CT for the pore topology of three samples.

3.3.4. Image segmentation and parameterization

For the image segmentation and parameterization performed for the parts described above, 3.3.1. Identification of the ceramic pastes, 3.3.2. Identification of the ceramic firing and 3.3.3. Formation of the ceramics, the acquired 2D and 3D images were calculated with MATLAB (2018b) (Table 3-3).

	2D analysis	3D analysis
Image visualization	imread(); dlmread(); imshow()	fopen(); fread(); reshape(); imshow(), isosurface(); patch();
Conversion of image data type	rgb2gray(); im2bw(); size()	Int16(); double(); imbinarize(); size(); dim(); gpuArray(); gather()

Image data modification	imfill(); imdilate(); imerode(); imcomplement() including calculation and logical decision of arrays	histeq(); imfill(); imdilate(); imerode(); imcomplement(); sum(); A(~B) = 0; imclearborder() including calculation and logical decision of arrays
Acquisition of target properties	bwconncomp(); regionprops()	Bwconncomp(); regionprops3(); labelmatrix(); ismember()

Table 3-3. Examples of main functions used for the image analysis by Matlab in this study.

For the quantification of sand grain shapes in 2D, the plane polarized micrographs were converted to the gray scales to reduce the color variances and to raise the accuracy in segmentation of heterogeneous phases. Various image filters and retouching the images were used as well, in order to achieve precise and fast segmentation. After segmentation, numeric properties of shapes and pores in 2D were calculated by the CPU using eight-connectivity/neighborhood of pixels (Figure 3-8; 3-9), while the calculations of 3D objects were performed by CPU and GPU using six- and 26-connectivity/neighborhood of voxels (Figure 3-10). The connectivity of pixels and voxels determines a same region by counting adjacent unit cells. Eight-connectivity defines the 2D area sharing same vertices. In 3D image processing, the same region calculated by six-connectivity shares identical faces with the adjacent cells, while that by 26-connectivity shares edges, faces and vertices. The details of each parameter will be discussed in the following.

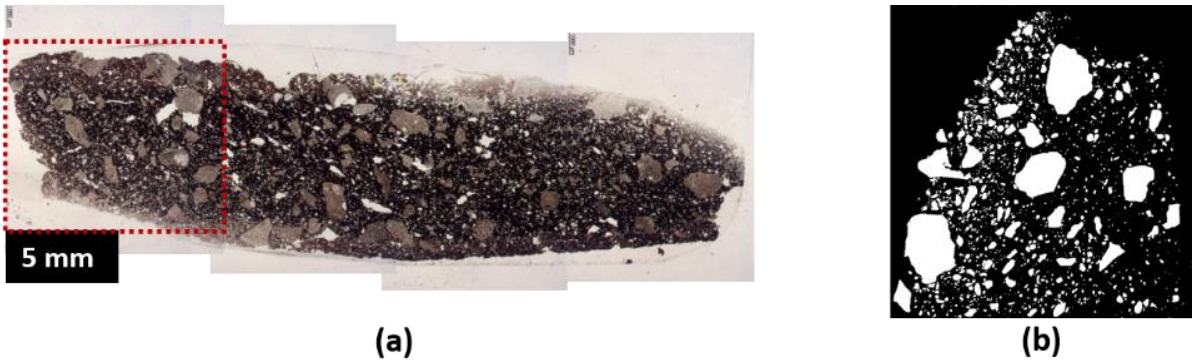

Figure 3-8. (a) Polarized light microscopic images (plane polarized light) of the cross section; (b) segmented image of sand grains (white).

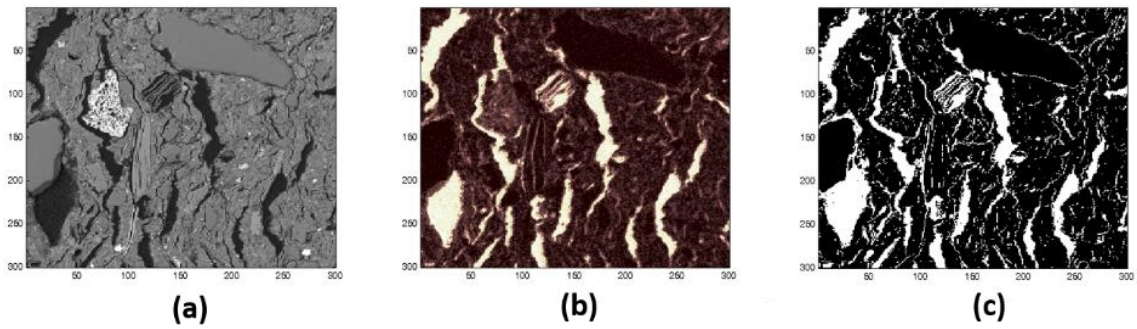

Figure 3-9. Visualization of the 2D matrix according to the intensity of (a) BSE and (b) Carbon and segmented image of pores from the matrix (measurement area=300x300 µm^2).

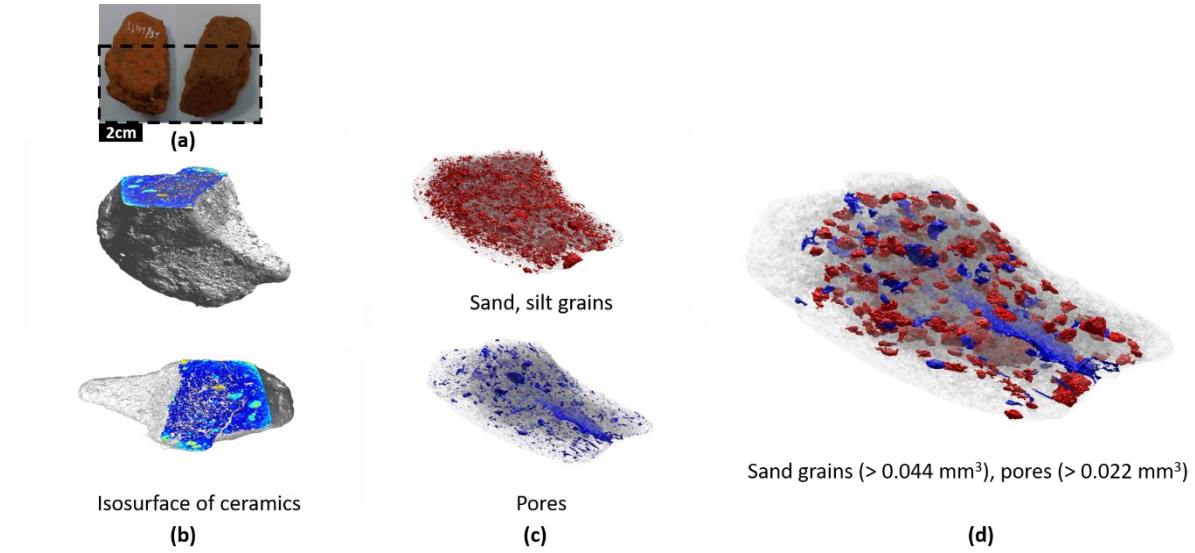

Figure 3-10. (a) Original ceramic sherd and its ROI in the box of the black dashed line; (b) Isosurface of the sample with Isocaps of the exposed cross section; (c) Segmentation of sand/silt grains and pores; (d) Segmentation of sand grains and pores with the specific volume size.

3.4. References

1. Vernon-Parry, K.D. Scanning electron microscopy: an introduction. III-Vs Review 13(4) (2000) 40-44. https://doi.org/10.1016/S0961-1290(00)80006-X.

2. Chatterjee, A.K. Chapter 8 - X-Ray Diffraction. In: Ramachandran, V.S., Beaudoin, J.J. (Eds.), Handbook of Analytical Techniques in Concrete Science and Technology, William Andrew Inc.: Norwich, NY. (2001) pp. 275-332. https://doi.org/10.1016/B978-081551437-4.50011-4.

3. Bragg, W.L. The Crystalline State I. The Macmillan Company: New York (1934).

4. McQuarrie, Donald A. Physical Chemistry: A molecular Approach. University Science Books: Sausalito (1997).

5. Beran, A., Voll, D., Schneider, H. IR spectroscopy as a tool for the characterization of ceramic precursor phases. In: Beran, A., Libowitzky, E. (Eds.), EMU Notes in Mineralogy 6, European Mineralogical Union and the Mineralogical Society of Great Britain and Ireland (2004) pp. 189-226.

6. Stern, F. Elementary of optical properties of solids. Solid State Phys. 15 (1963) 327-340.

7. W.B. Peatman, U. Schade, A brilliant infrared light source at BESSY. Rev. Sci. Instrum. 72(3) (2001) 1620-1624. https://doi.org/10.1063/1.1347976.

8. Schade, U., Ortolani, M., Lee, J. Technical Report: THz Experiments with Coherent Synchrotron Radiation from BESSY II. Synchrotron Radiation News 20(5) (2007) 17-24. http://dx.doi.org/10.1080/08940880701631351.

9. Ketcham, R.A., Carlson, W.D. Acquisition, optimization and interpretation of X-ray computed tomographic imagery: applications to the geosciences. Comput. Geosci. 27 (2001) 381-400. https://doi.org/10.1016/S0098-3004(00)00116-3.

10. Cnudde, V., Boone, M.N. High-resolution X-ray computed tomography in geosciences: A review of the current technology and applications. Earth-Sci. Rev. 123 (2013), 1-17. https://doi.org/10.1016/j.earscirev.2013.04.003.

11. L. Puskar, U. Schade, The IRIS THz/Infrared beamline at BESSY II. Helmholtz-Zentrum Berlin für Materialien und Energie. Journal of large-scale research facilities 2 (2016) A95. http://dx.doi.org/10.17815/jlsrf-2-95.
12. Zähle, M.A. Kinematic Formula and Moment Measures of Random Sets. Math. Nachrichten 149 (1990) 325–340.

Chapter 4. Identification of the ceramic pastes

4.1. Sand/silt grains in the ceramics

4.1.1. Mineralogical composition

Most sand and silt grains in the ceramics are lithoclasts derived from volcanic, metamorphic or sedimentary rocks. Various mineralogical combinations in the ceramic pastes besides clay minerals were identified by optical petrography, XRD and SEM-EDS and it is summarized according to the archaeological site (Figure 4-1). The chemical composition of all the alteration products were measured by the point analysis using SEM-WDS (Table 4-1). According to the results, those alteration products in the ceramic pastes were identified as mica-chlorite mixed layers (Table 4-1: Ransyrt1_Bt_Chl_1-11; Kabardinka2_Bt_Chl_1). The mica-chlorite intergrowths in the Kabardinka 2 samples have more K contents than those from Ransyrt 1. The other phases (Table 4-1: Ransyrt1_alteration_1-6; Kabardinak2_alteration_1-10) are mostly dominated by SiO_2, MgO, Fe_2O_3 and CaO. There are a few ceramic sherds containing diopside. In Kabardinka 2, the ceramics have vitreous and very porous Si rich grains (Table 4-1: Kabardinka2_X1-4). Numerous closed pores with a globular shape in a relatively big size could be produced by the fluid inclusions or during the melting phase.

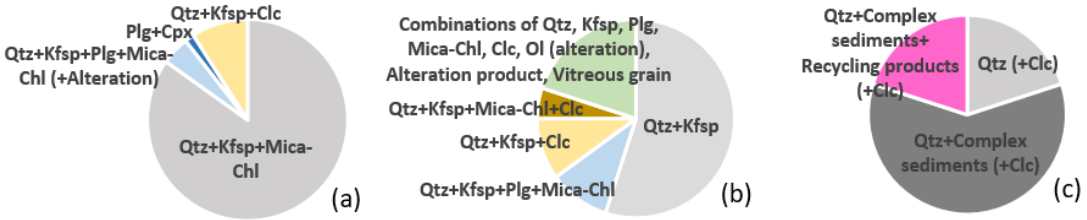

Figure 4-1. Dominant mineralogical combinations of the ceramics from (a) Ransyrt 1, (b) Kabardinka 2, (c) Levinsadovka-Saf'janovo (Clc: calcite, Cpx: clinopyroxene, Kfsp: K-feldspar, Mica-Chl: mica-chlorite mixed layers, Ol: olivine, Plg: plagioclase, Qtz: quartz).

Sample No.	SiO2	TiO2	Al2O3	FeO	MnO	MgO	CaO	Na2O	K2O	BaO	F	Cl	Total
Ransyrt1_Bt_Chl_1	37.69	2.39	18.06	19.53	0.62	10.71	0.74	0.32	6.67	0.19	2.26	0.10	**98.31**
Ransyrt1_Bt_Chl_2	40.67	3.02	20.62	14.35	0.41	9.15	1.11	0.40	6.41	0.16	1.78	0.15	**97.43**
Ransyrt1_Bt_Chl_3	38.70	2.01	18.86	20.42	0.21	7.31	0.92	0.34	8.12	0.15	0.77	0.02	**97.50**
Ransyrt1_Bt_Chl_4	36.03	0.17	23.04	28.30	0.73	6.86	1.78	0.13	1.23	0.07	0.00	0.05	**98.36**
Ransyrt1_Bt_Chl_5	38.69	0.00	22.57	21.70	0.38	10.52	2.06	0.30	1.66	0.13	0.31	0.02	**98.19**
Ransyrt1_Bt_Chl_6	36.96	0.35	21.59	24.84	0.39	12.29	2.30	0.17	0.72	0.06	0.21	0.00	**99.80**
Ransyrt1_Bt_Chl_7	38.78	0.00	23.44	21.72	0.40	10.65	1.90	0.10	0.68	0.11	0.19	0.05	**97.93**
Ransyrt1_Bt_Chl_8	38.91	0.00	19.25	24.08	0.24	11.55	2.70	0.09	0.30	0.05	0.34	0.01	**97.37**
Ransyrt1_Bt_Chl_9	38.62	0.31	19.74	24.71	0.26	12.14	2.72	0.17	0.48	0.08	0.18	0.01	**99.33**
Ransyrt1_Bt_Chl_10	37.73	10.01	15.44	15.27	0.15	6.12	13.45	0.05	0.33	0.22	1.50	0.02	**99.67**
Ransyrt1_Bt_Chl_11	38.59	0.00	19.13	23.61	0.14	12.88	2.58	0.17	0.52	0.10	0.06	0.01	**97.77**
Ransyrt1_alteration_1	51.03	0.54	3.90	5.67	0.06	15.82	23.32	0.16	0.03	0.00	0.08	0.00	**100.58**
Ransyrt1_alteration_2	50.89	0.52	3.91	5.74	0.07	16.18	23.02	0.19	0.05	0.02	0.00	0.00	**100.59**
Ransyrt1_alteration_3	50.00	0.57	4.64	6.88	0.08	15.34	22.10	0.22	0.00	0.04	0.25	0.00	**100.00**
Ransyrt1_alteration_4	46.12	1.60	8.50	14.88	0.32	13.92	12.32	1.44	0.76	0.00	0.61	0.00	**100.20**
Ransyrt1_alteration_5	46.27	1.70	8.20	13.51	0.26	13.41	12.32	1.53	0.77	0.00	0.65	0.00	**98.33**
Ransyrt1_alteration_6	48.86	0.98	5.83	9.33	0.16	14.93	18.62	0.71	0.32	0.01	0.32	0.00	**99.94**

Kabardinka2_Bt_Chl_1	39.44	4.51	13.06	19.05	0.17	13.59	2.21	0.26	4.76	0.05	0.65	0.09	**97.55**
Kabardinka2_ alteration_1	45.15	1.48	8.08	18.38	0.26	12.21	12.38	1.33	0.82	0.03	0.30	0.00	**100.30**
Kabardinka2_ alteration_2	44.41	1.97	9.16	17.73	0.36	10.83	12.47	1.55	0.95	0.00	0.64	0.00	**99.78**
Kabardinka2_alteration_3	45.63	1.40	8.23	18.10	0.30	11.66	12.43	1.50	0.95	0.00	0.34	0.00	**100.40**
Kabardinka2_alteration_4	44.53	1.97	9.36	17.74	0.30	10.93	12.21	1.57	0.81	0.06	0.34	0.00	**99.67**
Kabardinka2_alteration_5	44.58	1.98	9.97	12.57	0.11	15.20	12.44	1.83	0.75	0.03	0.80	0.00	**99.94**
Kabardinka2_alteration_6	45.67	1.95	9.40	12.44	0.15	15.60	12.01	1.67	0.66	0.04	1.36	0.00	**100.36**
Kabardinka2_alteration_7	43.95	2.82	10.56	13.07	0.14	14.08	12.31	2.07	0.79	0.03	1.10	0.00	**100.45**
Kabardinka2_alteration_8	38.25	0.14	24.07	12.73	0.19	0.08	24.35	0.00	0.12	0.00	0.08	0.04	**100.00**
Kabardinka2_alteration_9	38.34	0.16	24.28	12.57	0.32	0.02	24.28	0.00	0.05	0.00	0.00	0.00	**100.01**
Kabardinka2_alteration_10	38.24	0.11	24.28	12.68	0.25	0.00	23.91	0.01	0.07	0.02	0.04	0.04	**99.64**
Kabardinka2_X_1	70.94	0.49	13.09	1.63	0.01	0.40	1.39	1.81	1.62	0.01	1.06	0.21	**92.17**
Kabardinka2_X_2	73.00	0.16	13.68	1.69	0.03	0.43	1.54	2.16	2.84	0.05	0.16	0.00	**95.65**
Kabardinka2_X_3	73.13	0.48	13.68	1.66	0.03	0.40	1.54	2.20	2.99	0.02	0.00	0.00	**96.13**
Kabardinka2_X_4	74.47	0.22	13.78	1.80	0.01	0.41	1.35	2.16	3.49	0.07	0.00	0.00	**97.75**

Table 4-1. Quantitative analysis of mica-chlorite, alteration products and vitreous grains from Ransyrt 1 and Kabardinka 2.

Sand grains in the ceramics from Ransyrt 1 are categorized into four groups: (1) quartz and K-feldspar, mica-chlorite intergrowths with traces of albite and kaolinite; (2) quartz and K-feldspar, mica-chlorite intergrowths and plagioclase (from anorthite to albite, anhedral) and alteration products; (3) Plagioclase (albite, euhedral in altered volcanic glass) and clinopyroxene (diopside, euhedral/subhedral); (4) quartz, K-feldspar and calcite (Figure 4-2.a-c,g). In many samples, quartz and K-feldspar build a fine mixture in grains (Figure 4-2.a). Ceramics excavated at Kabardinka 2 contain different combinations: (1) quartz and K-feldspar (anhedral) often accompanied by kaolinizing phases; (2) quartz, K-feldspar, mica-chlorite intergrowths and plagioclase, mostly Ca-plagioclase from anorthite to labradorite in a subhedral or euhedral form located in the altered volcanic glass and kaolinizing phases; (3) quartz, K-feldspar, calcite; (4) quartz, K-feldspar, calcite and mica-chlorite intergrowth; (5) random combinations of quartz, K-feldspar, plagioclase (Ca-dominant, subhedral), mica-chlorite intergrowths, calcite, kaolinizing phases, alteration product similar to olivine or amphibole, clinopyroxene, and SiO_2-rich porous and vitreous grains (Figure 4-2.d-f,g).

The Samples found at Levinsadovka-Saf'janovo have simpler combinations: (1) quartz dominant; (2) quartz and sediments composed of quartz, K-feldspar and various alteration phases (Figure 4-2.i). In those sediments, there are grains containing thermally transformed clays, quartz and K-feldspar (Figure 4-2.i-k). Several calcite grains were observed in all samples.

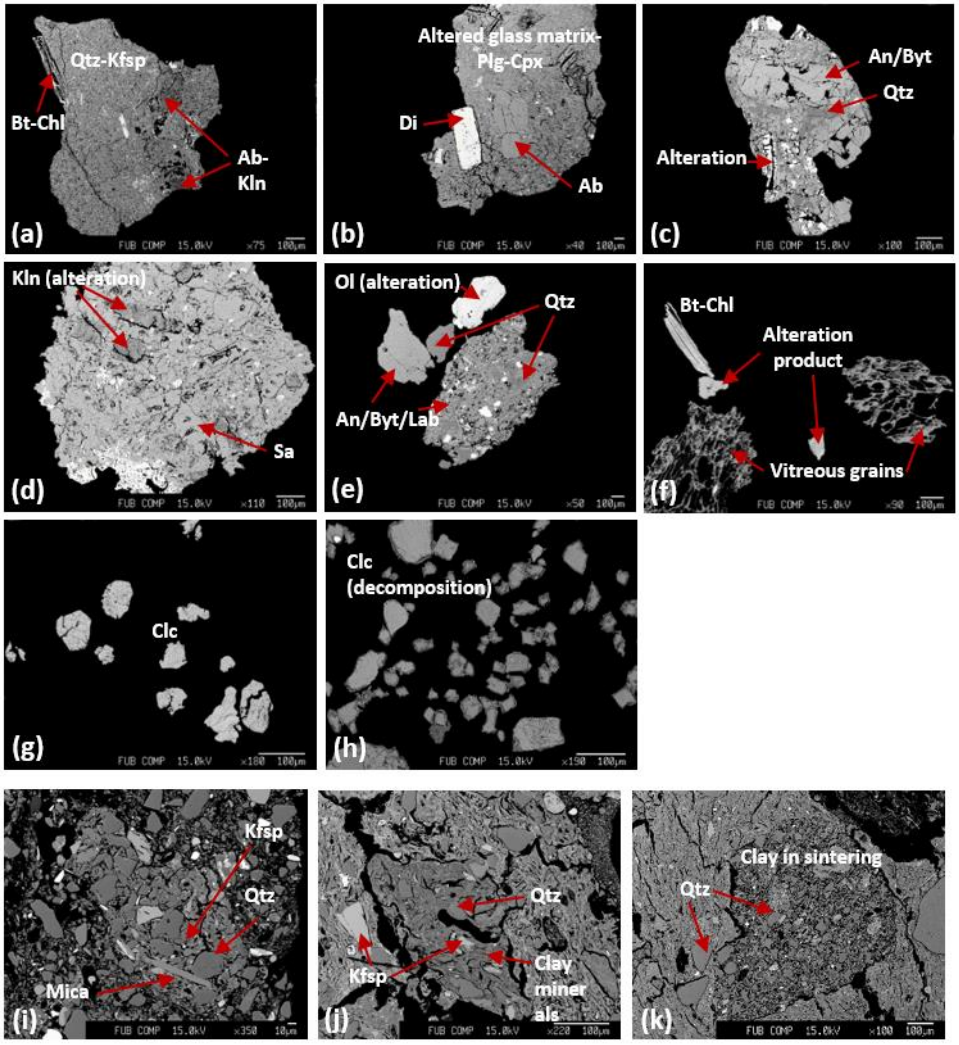

Figure 4-2. Mineralogical composition of sand grains in the ceramic paste (all scales for 100 µm): (a) quartz and K-feldspar matrix, biotite-chlorite and kaolinite-albite as alteration trace; (b) diopside and albite in altered glass matrix; (c) anorthite-bytownite, quartz and alteration product; (d) sanidine and kaolinite (alteration); (e) anorthite-bytownite-labradorite, quartz, olivine (alteration); (f) biotite-chlorite, alteration product, vitreous porous grains; (g) calcite; (h) calcite in thermal decomposition; (i) Lithoclasts composed of K-feldspar, quartz and mica; (j) aggregate composed of clay, K-feldspar and quartz; (k) aggregate composed of clay in sintering, quartz (Ab: albite, An: anorthite, Byt: bytownite, Bt: biotite, Chl: chlorite, Clc: calcite, Cpx: clinopyroxene, Di: diopside, Lab: labradorite, Ol: olivine, Plg: plagioclase, Qtz: quartz, Sa: sanidine).

4.1.2. Shape parameters of sand grains

Most ceramic pastes in the ancient material production contain sand grains. Especially, coarse sand grains composed of lithoclasts bigger than 250 µm reflect the environment where they are originated well and keep their form during the firing of the ceramics by the grain size effect. Moreover, they can be taken easily from the cross thin sections in 2D which are prepared in many ceramic studies. According to the mineralogical and chemical analysis, grain forming dominant minerals are presented in Figure 4-1 [1]. Because most sands in a ceramic object are composed of various mineralogical phases in various textures and the shapes of these poly-mineral grains were changed during the sedimentation process, shape parameters of the sand grains should be calculated for each grain and not for each single mineral phase. In the samples, lithoclasts and sedimentary aggregates composed of similar mineral phases exist

in various sizes, indicating a possibility that the resource were gathered in the sediments accumulated by the natural depositional process.

In this study, we calculated the following shape parameters: maximum length, circularity, sphericity 1 and sphericity 2 of an idealized ellipse that has the same normalized second central moments as the segmented object. They were defined as [2-4]:

$$\text{Circularity: } \frac{4\pi A}{P^2}, \tag{4-1}$$

$$\text{Sphericity 1 (elongation): } \frac{D_{F,max}}{D_{F,min}}, \tag{4-2}$$

$$\text{Sphericity 2 (elongation): } \frac{a}{b}, \tag{4-3}$$

where A and P mean area and perimeter, D_F is Feret diameter, a and b are major axis minor axis of an idealized ellipse of the grains, accordingly.

Figure 4-3 illustrates different size distribution, circularity, sphericity 1 of the coarse sands according to the archaeological sites and the dominant mineral groups in the sand grains in the ceramics. The average and standard deviation of the shape parameters of individual grains in each sample were calculated according to the site at Ransyrt 1 (Figure 4-3.a), Kabardinka 2 (Figure 4-3.b) and Levinsadovka–Saf'janovo (Figure 4-3.c). In general, the ceramics found at Ransyrt 1 contained bigger sized grains with a wider size distribution and less circular shapes than the other sites. The ceramics excavated at Levinsadovka and Saf'janovo have more rounded and finer sands. Despite the high distribution of the mean sand size, there is a tendency that the size and angularity of coarse sands in the ceramic pastes decrease from higher mountains through middle plateau to the alluvial sea coast.

The highest elongation degree of the grains of a sample group representing for Ransyrt 1 is bigger than those in the ceramics from the other sites. At the same time, the shape parameters of the sherds are varying within each site, where two or three groups can be classified within the ceramics from the same site. It is possible that the distribution of the mean value of the calculated shape parameters becomes smaller, if the measurement area is bigger or the several sherds originated from a single pottery are analyzed. Concerning the relation between the mineralogical combination of the coarse sands and their shape parameters, the Ransyrt 1 samples show this correlation in the circularity very slightly, while this is found in the size distribution and sphericity 1 for the samples from Kabardinka 2. However, those parameters derived from the 2D image processing would represent a relative value regarding the three dimensional alignment of grains in the ceramics. Figure 4-4 shows the comparison between the grain size distribution, sphericity 1 and sphericity 2 calculated with the 2D and 3D image analysis of an example. In comparison to the 2D data, the elongation degree of the coarse sands from the 3D images is higher and this attests to the fact that elongation vertical to the observed sample surface is detected in 3D but not in 2D. The alignment of sands can therefore influence the results of 2D image analysis.

Although the ceramic pastes could be prepared by the addition of various sediments and removal of specific components by the potters, the grain size distribution of the coarse sand grains in the ceramics reflect the soil development of each site concerning the sedimentation process from the mountains to

the alluvial zones [1,5]. The circularity and sphericity of coarse sand grains show site specific geological setting as well. Because Ransyrt 1 on the higher plateau has less soil than Kabardinka 2 on the lower plateau and the sites around the alluvial zone, the potters would have gathered resource for the preparation of ceramic pastes around the settlement sites.

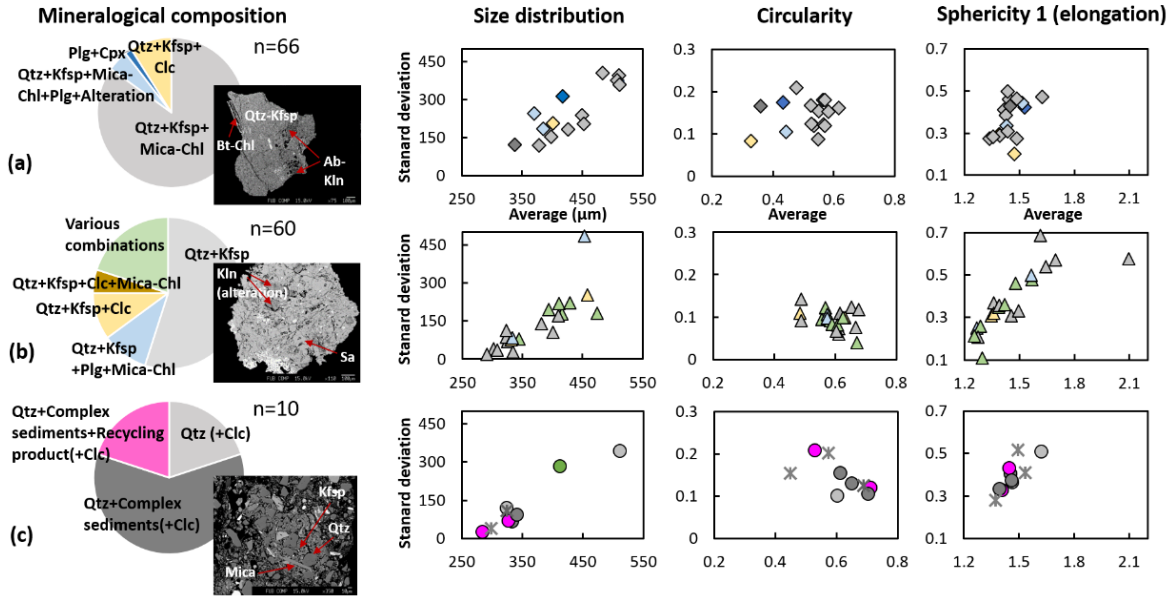

Figure 4-3. Mineralogical composition of dominant grain groups of the samples for the sites, (a) Ransyrt 1, (b) Kabardinka 2, (c) Levinsadovka–Saf'janovo with the back scattered electron (BSE) images of the representative grains [1] is compared to the size distribution, circularity and sphericity 1 of coarse sand grains (>250µm, lithoclasts) present in the selected samples (Clc: calcite, Cpx: clinopyroxene, Kfsp: K-feldspar, Sa: sanidine, Mica–Chl: mica–chlorite mixed layers, Bt: biotite, Ol: olivine, Plg: plagioclase, Qtz: quartz, Kln: kaolinite). Each mineralogical grain groups presented in different colors (Qtz + Kfsp + Mica – Chl/Qtz + Kfsp/Qtz (+Clc): light grey, Qtz + Kfsp + Plg + Mica Chl + Alteration/Qtz + Kfsp + Plg + Mica – Chl: light blue, Plg + Cpx: blue, Qtz + Kfsp + Clc: light yellow, Qtz + Complex sediments (+Clc): dark grey, various combinations: light green).

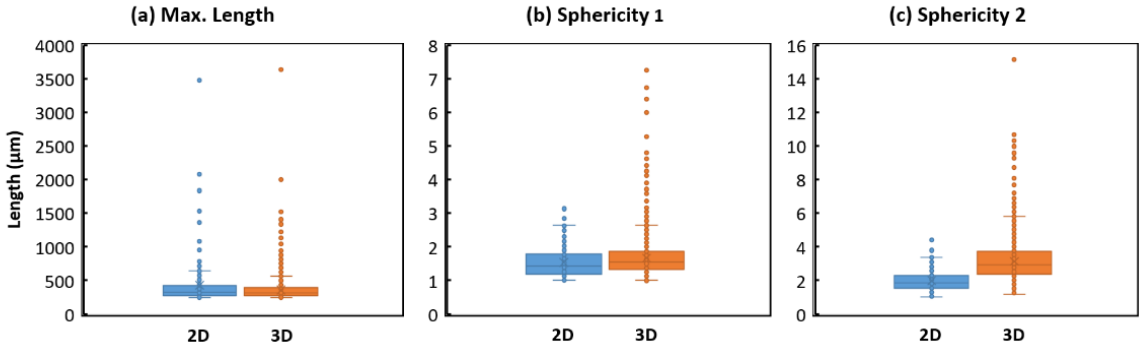

Figure 4-4. (a) Grain size distribution (max. length), (b) sphericity 1 and (c) sphericity 2 derived from 2D (blue) and 3D (orange) image analysis of the coarse sand grains (>250 µm) in the ceramic sherd (Ran1_514_2). Pixel size of 10^2 µm^2 and grain numbers/A (area) = 1.501 ea/mm^2 for the 2D images. Voxel size of 9.49^3 µm^3 and sand grain numbers/V (volume) = 12.182 ea/mm^3.

However, every archaeological site has various groups of samples according to each shape parameters. This means that the potters used different strategy in the gathering, preparation or control of ceramic pastes. Grain-like cavities proved in a few samples by the 3D scanning are possibly produced by the thermal decomposition of calcites during firing (Figure 4-5) [6]. This informs us that calcite grains were used intensively in a few ceramics.

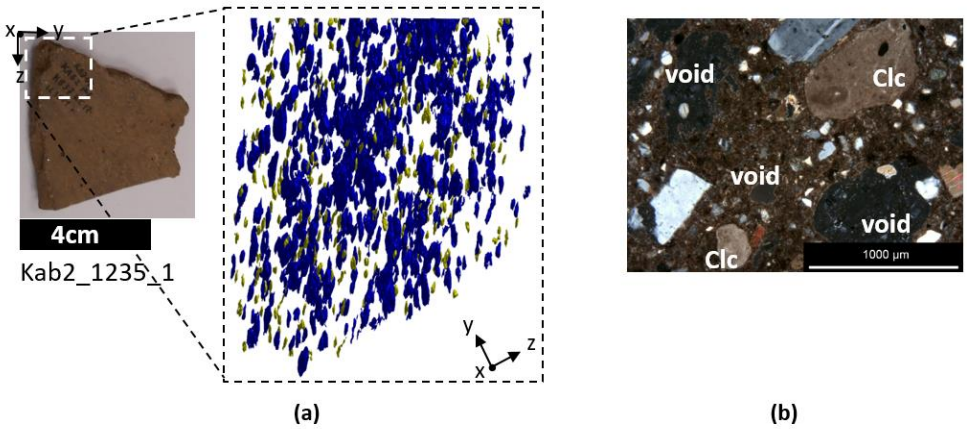

Figure 4-5. (a) Original ceramic sherd and segmented grain like cavities, calcite ghosts in the sample (blue and yellow) (voxel size: 25.00^3 µm^3). (b) A cross polarized light micrograph of the cross thin section shows coexisting calcite grains and closed type of voids in different sizes (Clc: calcite).

4.2. Chemical compositions of the ceramic matrix (grains < 50µm)

Chemical composition of the ceramic matrix provides the background for estimating the evolution of the ceramic matrix under heating. In order to avoid the grain size effect, only grains smaller than 50 µm were measured to characterize the ceramic matrix using SEM-WDS. The results were normalized to 100% concerning porosity and (crystal-)water content of the matrix (Table 4-2).

Ceramic No.	SiO2	TiO2	Al2O3	BaO	FeO	MnO	MgO	CaO	Na2O	K2O	P2O5	Total
Ran1_dmp1	61.70	0.62	22.64	0.11	6.52	0.15	1.91	1.66	1.10	3.25	0.34	100
Ran1_549	60.34	0.77	23.85	0.13	7.38	0.08	1.87	2.07	0.49	2.50	0.52	100
Ran1_329	62.30	0.61	21.41	0.14	6.82	0.13	1.61	2.02	0.99	2.89	1.06	100
Ran1_527_1	61.05	1.00	18.77	0.07	8.21	0.14	1.69	3.84	1.08	2.91	1.24	100
Ran1_514_2	59.65	0.72	22.25	0.05	7.95	0.15	1.67	2.87	1.32	2.55	0.83	100
Ran1_370_1	59.42	1.01	17.51	0.06	5.40	0.06	5.02	6.49	0.66	3.52	0.84	100
Ran1_514_3	64.52	0.75	18.86	0.06	6.66	0.10	1.64	3.18	0.78	2.42	1.02	100
Ran1_449	59.90	0.75	19.34	0.05	6.86	0.09	2.43	5.14	0.63	4.40	0.41	100
Ran1_514_1	63.46	0.75	18.23	0.06	6.44	0.11	2.05	3.88	0.88	2.84	1.29	100
Ran1_KB3kc1	63.20	0.87	20.05	0.05	7.44	0.13	1.76	2.41	1.07	2.56	0.45	100
Ran1_437_83	49.18	0.81	16.40	0.04	6.72	0.12	3.64	18.19	0.50	1.83	2.58	100
Ran1_167_4	62.00	0.59	20.83	0.04	8.56	0.09	1.58	2.49	1.57	2.00	0.25	100
Ran1_17_2	64.42	1.20	18.60	0.06	7.73	0.07	1.30	2.35	0.82	2.64	0.81	100
Ran1_6_9	76.73	0.36	11.59	0.01	4.64	0.03	2.44	3.73	0.22	0.11	0.13	100
Ran1_225_4	57.45	0.80	25.79	0.05	7.78	0.13	1.23	3.20	0.55	2.31	0.72	100
Ran1_261_40	60.51	0.95	22.67	0.06	6.08	0.04	2.76	1.95	0.50	4.00	0.47	100
Ran1_357_20	63.53	0.75	19.15	0.05	7.06	0.14	2.07	2.22	1.32	2.85	0.87	100
Ran1_278_x	58.11	0.83	20.58	0.06	8.38	0.15	2.86	4.30	0.38	2.69	1.64	100
Ran1_217_17	62.00	1.03	22.86	0.06	5.54	0.13	0.96	2.81	0.86	2.64	1.12	100
Ran1_244_9	62.63	0.89	18.12	0.05	6.95	0.27	2.95	4.43	1.04	2.48	0.20	100
Ran1_326_9	61.73	0.77	19.54	0.07	6.55	0.29	2.34	4.82	0.69	2.36	0.84	100
Ran1_306_5	59.68	0.75	15.53	0.05	6.54	0.09	5.07	8.74	0.98	2.23	0.34	100
Ran1_111_1	60.31	0.92	22.49	0.04	8.36	0.10	1.09	2.63	1.17	2.29	0.58	100
Ran1_224_9	64.03	0.83	19.82	0.07	7.35	0.19	1.46	1.94	0.88	2.76	0.67	100
KAE_650_10 (body)	67.78	0.74	16.44	0.05	8.07	0.21	1.65	1.36	0.64	2.96	0.10	100
KAE_650_10 (slip)	67.76	0.97	16.76	0.06	7.43	0.12	1.55	1.59	0.77	2.83	0.15	100
KAE_1578_4	66.41	0.83	15.60	0.06	9.01	0.17	1.54	2.04	0.83	3.21	0.31	100
KAE_2113_1	62.42	1.28	26.94	0.04	3.10	0.06	0.80	1.63	0.72	2.85	0.15	100
KAE_844_1	64.07	0.84	19.78	0.04	8.72	0.03	1.10	1.29	1.07	2.67	0.38	100
KAE_633_1	63.85	0.87	17.80	0.06	9.10	0.07	1.78	2.16	0.57	2.83	0.92	100
KAE_2008_641_1	60.04	0.96	24.86	0.06	5.99	0.03	0.65	2.23	0.62	2.69	1.86	100
KAE_483_3	66.58	1.03	16.25	0.06	8.42	0.18	1.46	1.73	0.78	2.87	0.65	100
KAE_516_26	67.76	0.83	15.74	0.08	7.25	0.25	1.27	2.26	0.67	2.80	1.11	100
KAE_516_2	66.98	0.72	15.94	0.07	7.12	0.05	1.30	2.07	1.13	3.04	1.57	100
KAE_482_1	59.44	0.82	19.88	0.04	8.80	0.12	1.67	1.78	1.05	4.45	1.96	100
KAE_918_1	53.80	0.95	22.60	0.05	14.63	0.26	1.83	2.05	0.43	2.70	0.71	100
KAE_NN	67.28	0.72	15.35	0.09	7.08	0.44	1.38	2.82	0.78	2.74	1.33	100
KAE_1697_1	70.27	1.02	15.85	0.05	6.33	0.12	0.86	2.04	0.61	2.44	0.42	100
KAE_797_1	59.74	0.80	16.95	0.05	10.91	0.33	1.62	5.69	0.89	2.66	0.38	100
KAE_1162_1	65.53	1.15	22.26	0.05	4.43	0.02	1.05	1.77	0.74	2.77	0.23	100
KAE_1195_6	61.08	0.98	20.46	0.07	8.91	0.38	1.44	2.61	0.89	2.35	0.82	100
KAE_28_2	64.07	1.04	18.48	0.06	7.48	0.05	1.52	2.88	0.74	2.91	0.77	100
KAE_1418_1	60.33	0.76	17.18	0.05	6.59	0.10	2.62	4.99	0.97	5.12	1.30	100

KAE_1235_1	66.02	0.91	16.45	0.07	6.30	0.03	1.49	4.38	0.83	2.70	0.81	100
KAE_1152_1	65.83	1.20	18.78	0.05	8.22	0.03	0.96	1.33	0.74	2.49	0.35	100
KAE_1021_1	58.68	1.00	23.27	0.04	9.45	0.16	1.16	2.76	1.18	1.83	0.48	100
Lev_7718	75.96	0.46	9.18	0.22	5.28	0.04	1.44	3.69	0.52	2.74	0.47	100
Lev_8653_1	75.13	0.12	9.07	0.16	4.67	0.05	1.29	5.00	1.19	2.84	0.47	100
Lev_8653_3	67.90	0.65	17.64	0.05	6.09	0.04	2.12	1.14	1.33	2.87	0.17	100
Saf_501_5	58.83	0.89	24.64	0.03	7.01	0.04	1.99	3.40	0.31	2.62	0.23	100
Saf_502_3	64.25	1.16	20.07	0.04	7.37	0.05	2.11	1.45	0.30	3.03	0.18	100
Saf_501_4	67.70	1.04	17.31	0.06	5.29	0.04	1.56	2.25	0.47	3.54	0.73	100
Lev_8653_5	64.41	1.03	22.16	0.04	5.88	0.02	1.62	2.24	1.10	1.32	0.19	100
Lev_9633	65.91	0.77	16.90	0.06	6.34	0.06	2.25	3.08	1.17	3.16	0.31	100

Table 4-2. Chemical composition of the ceramic matrix (grains < 50 µm) normalized to 100 wt%.

The projection to the SiO_2-CaO-Al_2O_3 system shows that samples from Levinsadovka and Saf'janovo have more SiO_2 and those from Ransyrt 1 site the least (Figure 4-6.a). In the at-f-alc system (at= CaO+MgO; f= Fe_2O_3; alc=K_2O+Na_2O) [7], Ransyrt 1 ceramics tend to have higher (Ca, -Mg) contents in the matrix, while those of Kabardinka 2 move toward Fe_2O_3 (Figure 4-6.b).

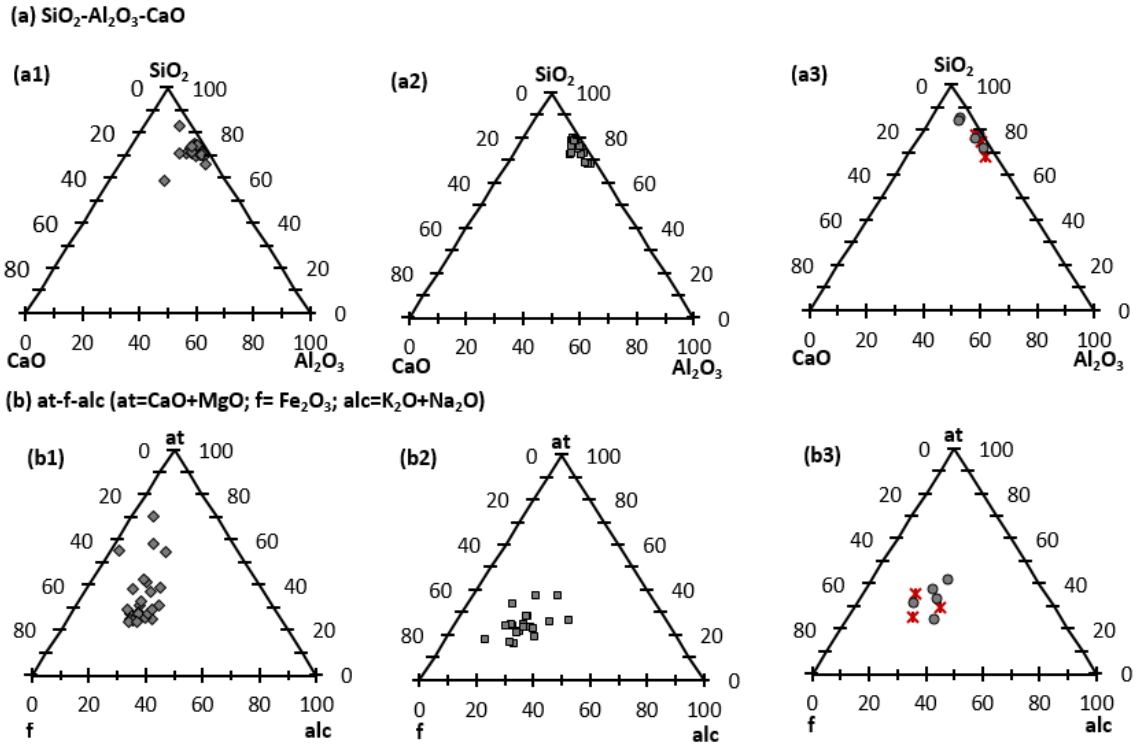

Figure 4-6. Chemical composition of ceramic matrix (grains < 50 µm) normalized to 100 wt.%: (a) SiO_2-Al_2O_3-CaO: (1) Ransyrt 1; (2) Kabardinka 2; (3) Levinsadovka-Saf'janovo; (b) at-f-alc (at=CaO+MgO; f= Fe_2O_3; alc=K_2O+Na_2O): (1) Ransyrt 1; (2) Kabardinka 2, (3) Levinsadovka-Saf'janovo.

4.3. Clay minerals in the ceramics

Identified by the specific XRD Bragg peaks representing illite 1M, such as set of 10 Å peak for (001), 4.98 Å for (002), 4.5 Å for (020) or 4.45-4.46 Å for (110), 2.58 Å for (130) or (13$\bar{1}$) lattice planes, illite is the main clay mineral of the studied ceramics (Figure 4-7). Their higher FWHM distinguished illite from mica [8]. Samples without illite phase are either highly deformed by firing or they do not include any clay minerals. Illite could be confirmed by the transmittance IR vibrations at 3623-3630 and 3690 cm^{-1}, too. The band occurring at 3623-3630 cm^{-1} is assigned to the stretching mode of the bond between Al and hydroxyl group which lies close to the SiO_4 tetrahedral structure, ν(Al-OH) [9-11]. Some samples show a band at 3653 cm^{-1} related with ν(Al-OH) neighboring with AlO_4 substitution of muscovite [12].

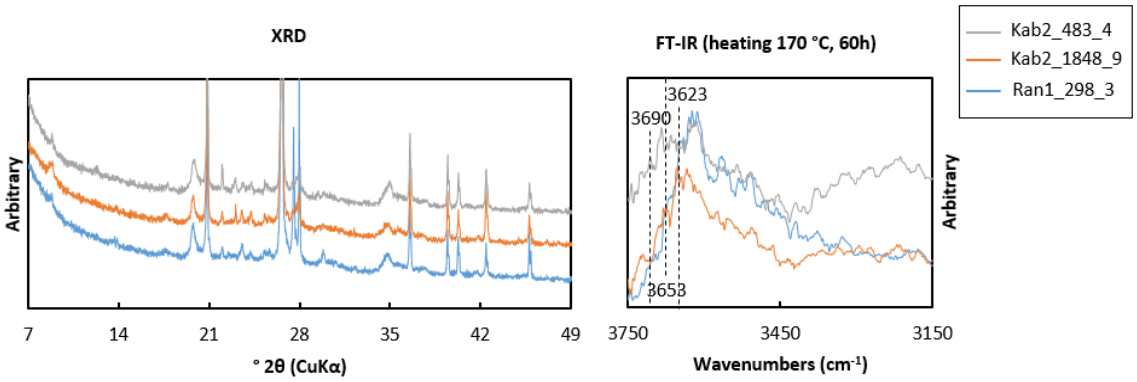

Figure 4-7. Representative XRD and FTIR (transmittance, samples heated at 170 °C for 60 hours) results of ceramic sherds excavated at Ransyrt 1 (blue) and Kabardinka 2 (orange, gray).

Although the peaks of quartz and feldspar present in all the ceramic samples overlap with those at ($\bar{1}11$) as well as ($\bar{1}12$)/($11\bar{2}$) and (112) lattice plane of illite, (020)/(110) peaks according to the polytype lie between 4.5 and 4.45 Å regardless of the thermal transformation (Figure 4-8) [13-15]. Because *cv*-/*tv*-1M polytypes have different dehydroxylation temperatures and most illite phases in the nature occur in a mixed form, the illite phases in the ceramic pastes would be mixed layers [16].

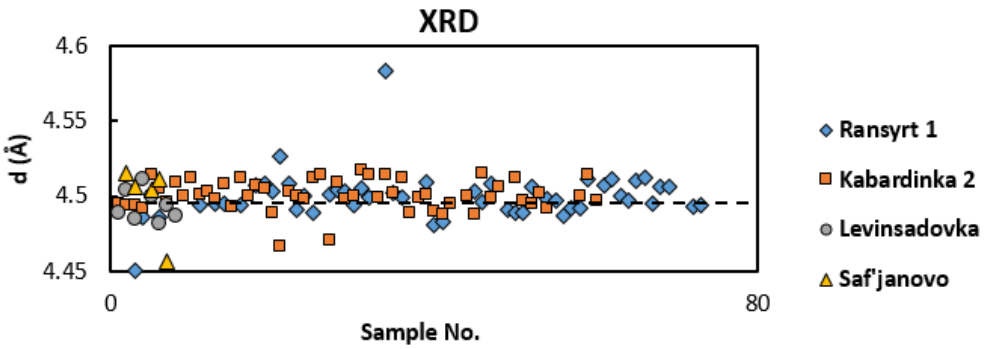

Figure 4-8. Illite d spacing at the lattice plane (020)/(110).

SR-FIR and DRIFT-NIR spectra of the representative samples in different pyrometamorphic states in this study confirmed that they are composed of mainly illitic clays without mixed layers (Figure 4-9). Moreover, these samples do not show the traces of other common clay minerals in Earth such as kaolinite or smectite series do not appear in the samples. The IR bands ranging between 100 and 90 cm^{-1} are assigned to the vibrations between K in the interlayer and OH^{-1} in octahedra confirm the main clay mineral of the samples is illite [17-22]. Simultaneously, the spectral features around 11000 cm^{-1} responsible for the transition between the 6-coordinated Fe^{2+} and Fe^{3+} in the clay mineral and the combinational vibration of Al/Mg/Fe-OH bonds at 4530, 4280 and 4500 cm^{-1} (2.2, 2.3, 2.5 µm, accordingly) with the small and rounded intensity and shapes support illite as the dominant clay in the measured samples as well [22-28]. These characteristics enable to distinguish illite from muscovite [27,29]. H_2O and OH reflectance of this clay mineral appear at 5230 and 7000 cm^{-1} (1.9 and 1.4 µm, accordingly) as well.

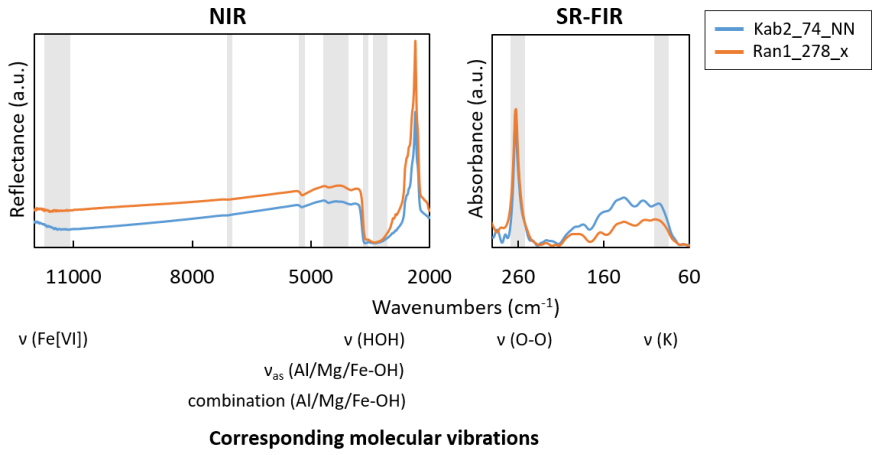

Figure 4-9. Comparison of SR-FIR absorption spectra and NIR diffuse reflectance spectra of the samples containing the lowest firing degree. (a) Ransyrt 1; (b) Kabardinka 2. Modified from *Park et al.* [1,22].

There were no distinguishable reflectance features related to the other Fe-bearing mineral phases such as goethite or ferrihydrite, similar to the XRD results of the same samples that no samples with less thermal deformation prove massive amounts of goethite, lepidocrocite or ferrihydrite in the ceramic paste [1].

4.4. Discussion: preparation of the ceramic pastes of the potters

The serial analysis of various analytical measurements provided information about the preparation of the ceramic pastes, too. The mineralogical composition of the sand and silt grains and their grain size distribution reflect the local geological setting of the site. This result indicates that the ceramic pastes were taken mostly from the naturally developed soil deposit. The potters at all the studied sites would prepare ceramic pastes using a sedimentary resource acquired from the local sites. Additionally, the ceramics from Ransyrt 1 contain less clay than Kabardinka 2 ceramics, which is probably influenced by the fact that Ransyrt 1 has fewer soils and clays than Kabardinka 2. Circularity and sphericity of the coarse sand grains reflect the geological setting of each sites, too. Ca-carbonates were more abundant in the samples found at Ransyrt 1 and Levinsadovka-Saf'janovo. However, some Ransyrt 1 ceramics contain clearly distinctive amounts of Ca in comparison to other samples from the same site and the Azov sea environment. It is possible that these Ca rich ceramics were made intentionally of very calcined clays by the potters at Ransyrt 1, while the other ceramics contain calcite grains that were originated from the natural soil deposit and these grains were not added by the potters. Besides, Levinsadovka yielded a sherd containing possible fragments of old pottery, because a few sediments in the samples contain thermally transformed clays, quartz and K-feldspar indicating possible older ceramic fragments. However, sharp edges proving breaking actions of the potters as possible intentional activity for producing temper materials, were difficult to find in this specific sherd. The local potters could recycle such possible old pottery fragments as weathered state as temper materials. The chemical composition of the ceramic matrix varies between the different sites as well as within a site. It indicates that the

potters prepared the ceramic pastes in various ways. The different grain groups in the ceramics from the same site support the possible existence of various recipes.

In the meanwhile, illite is detected as the dominant clay in almost all samples. It would be related to the potter's strategy to collect flexible soils in the close local environment. Because illite is formed normally in the highly altered place in the soil development process, illite rich clays would be the most common forming material. For the potters who lived in the semi-sedentary society, this type of clays could be one of the easiest options.

4.5. References

1. Park, K.S., Milke, R., Efthimiopoulos, I., Pausewein, R.R., Reinhold, S. Pyrometamorphic process of ceramic composite materials in the pottery production in the Bronze/Iron Age of the Northern Caucasus. Sci. Rep. 9 (2019) 10725, https://doi.org/10.1038/s41598-019-47228-y.

2. Wadell, H. Volume, shape, and roundness of quartz particles. J. Geol. 43(1932) 250–280.

3. Barrett, P.J. The shape of rock particles, a critical review. Sedimentol. 27 (1980) 291–303. https://doi.org/10.1111/j.1365-3091.1980.tb01179.x.

4. Krumbein, W.C. The Effects of Abrasion on the Size, Shape and Roundness of Rock Fragments. J. Geol. 49 (1941) 482–520.

5. Park, K.S., Reinhold, S., Milke, R. Pottery production technology and technological style in the North Caucasus (Russia) in the Bronze/Iron Age: Archaeological characterization from archaeometric results. (in prep.).

6. Fabbri, F., Gualtieri, S., Shoval, S. The presence of calcite in archaeological ceramics. J. Eur. Ceram. Soc. 34 (2014) 1899–1911. https://doi.org/10.1016/j.jeurceramsoc.2014.01.007.

7. Fabbri, B. and Fiori, C. Clays and complementary rawmaterials for stoneware tiles. Mineralogica Petrographica Acta 29A (1985) 535-545.

8. Carroll, D. Clay minerals: A guide to their X-ray Identification. The Geological Society of America, INC.: Boulder, Colorado (1970). https://doi.org/10.1130/SPE126.

9. Alvarez-Puebla, R.A., dos Santos Jr., D.S., Blanco, C., Echeverria, J.C., Garrido, J.J. Particle and surface characterization of a natural illite and study of its copper retention. J. Colloid. Interface. Sci. 285 (2005) 41-49. https://doi.org/10.1016/j.jcis.2004.11.044.

10. Prud'homme, E., Michud, P., Joussein, E., Peyratout, C., Smith, A., Rossignol, S. *In situ* inorganic foams prepared from various clays at low temperature. Appl. Clay. Sci. 51 (2011) 15-22. https://doi.org/10.1016/j.clay.2010.10.016.

11. Yeşilbaş, M. and Boily, J. -F. Particle size controls on water adsorption and condensation regimes at mineral surfaces. Sci. Rep. 6 (2016) 32361. https://doi.org/10.1038/srep32136.

12. Madejová, J.W., Gates, P., Petit, S. IR spectra of clay minerals. In: Gates, W.P., Kloprogge, J.T., Madejová, J., Bergaya, F. (Eds.), Infrared and Raman Spectroscopies of Clay Minerals. Elsevier: Amsterdam, Oxford, Cambridge MA. (2017) pp. 107-149.

13. Drits, V.A., Weber, F., Salyn, A.L., Tsipursky, S.I. X-ray identification of one-layer illite varieties: application of the study of illites around Uranium deposits of Canada. Clays. Clay. Miner. 41(3) (1993) 389-398. https://doi.org/10.1346/CCMN.1993.0410316.

14. Grathoff, G.H. and Moore, D.M. Illite polytype quantification using wildfire© calculated X-ray diffraction patterns. Clays. Clay. Miner. 44(6) (1996) 835-842. https://doi.org/10.1346/CCMN.1996.0440615.

15. Drits, V.A., Zviagina, B.B., McCarty, D.K., Salyn, A.L. Factors responsible for crystal-chemical variations in the solid solutions from illite to aluminoceladonite and from glauconite to celadonite. Am. Mineral. 95 (2010) 348-361.

16. Drits, V.A., Beson, G., Muller, F. An improved model for structural transformations of heat-treated aluminous dioctahedral 2:1 layer silicates. Clays. Clay. Miner. 43(6) (1995) 718-731. https://doi.org/10.1346/CCMN.1995.0430608.

17. Ishii, M., Shimanouchi, T., Nakahira, M. Far infrared adsorption spectra of layer silicates. Inorg. Chim. Acta. 1(3) (1967) 387-392. https://doi.org/10.1007/BF00654345.

18. Angino, E.E. Far infrared spectra of montmorillonite, kaolinite and illite. Nature. (1964) 7(4958) 569-571.

19. Prost, R., Laperche, V. Far-Infrared study of potassium in micas. Clays. Clay. Miner. 38(4) (1990) 351-355. https://doi.org/10.1346/CCMN.1990.0380403.

20. Schroeder, P.A. Far-Infrared study of the interlayer torsional-vibrational mode of mixed layer illite/smectites. Clays. Clay. Miner. 40(1) (1992) 81-91. https://doi.org/10.1346/CCMN.1992.0400109.

21. Heath, C., Pejcic, B., Piane, C.D., Esteban, L. Development of far-infrared attenuated total reflectance spectroscopy for the mineralogical analysis of shales. Fuel. 182 (2016) 771-779. https://doi.org/10.1016/j.fuel.2016.06.056.

22. Park, K.S., Schade, U., Vrijmoed, J.C., Reinhold, S., Milke, R. Redox-thermal behavior of the archaeological ceramics from the North Caucasus (Russia, Bronze/Iron Age). J. Eur. Ceram. Soc. (in revision)

23. Sherman, D.M., Waite, T.D. Electronic spectra of Fe^{3+} oxides and oxide hydroxides in the near IR to near UV. Am. Mineral. 70 (1985) 1262-1269.

24. Ramanaidou, E., Wells, M., Lau, I., Laukamp, C. Characterization of iron ore by visible and infrared reflectance and Raman spectroscopies. In: L. Lu (Ed.), Iron Ore: Mineralogy, Processing and Environmental Sustainability, Woodhead Publishing: Cambridge, Waltham, Kidlington (2015) pp. 191-228. https://doi.org/10.1016/B978-1-78242-156-6.00006-X.

25. Clark, R.N., King, T.V.V., Klejwa, M., Swayze, G.A., Vergo, N. High spectral resolution reflectance spectroscopy of minerals. J. Geophys. Res.-Sol. Ea. 95(B8) (1990) 12653-12680. https://doi.org/10.1029/JB095iB08p12653.

26. Post, J.L., Noble, P.N. The Near-Infrared combination band frequencies of dioctahedral smectites, micas and illites. Clays Clay Miner. 41(6) (1993) 639-644. https://doi.org/10.1346/CCMN.1993.0410601.

27. Duke, E.F. Near Infrared spectra of muscovite, Tschermak substitution, and metamorphic reaction progress, and metamorphic reaction progress: implications for remote sensing. Geology. 22 (1994), 621-624. https://doi.org/10.1130/0091-7613(1994)022<0621:NISOMT>2.3.CO;2.

28. Cloutis, E., MacKay, A., Norman, L., Goltz, D. Identification of historic artists' pigments using spectral reflectance and X-ray diffraction properties I. Iron oxide and oxy-hydroxide-rich pigments. J. Near. Infrared. Spec. 24(1) (2016) 27-45.

29. Bishop, J.L., Lane, M.D., Dyar, M.D., Brown, A.J. Reflectance and emission spectroscopy study of four groups of phyllosilicates: smectites, kaolinite-serpentinites, chlorites and micas. Clay. Miner. 43 (2008) 35-54. https://doi.org/10.1180/claymin.2008.043.1.03.

Chapter 5. Formation of the ceramics (inner structure)

5.1. Ransyrt 1: Results and discussion

Despite of various reasons and factors generated by the potters during the production or natural resources, use of the ceramics or weathering process, 3D alignments of macro-pores and coarse sand grains in the samples can provide a possibility to assume the formations of the inner structure of ceramic bottom and wall respectively. Normally, the identification and categorization of such formations can be easily misled by the optical surface observation due to the weathering process and can be limited in size and scale by the investigation using destructive 2D cross sections of ceramics. Therefore, this case study focused on the images of structural elements acquired by the 3D µ-CT in a range from mm to cm.

Figure 5-1 shows a classification of the inner formation of the bottom and wall part representative for Ransyrt 1. In the bottom-wall fragments, four types of alignments were identified: (1) most pores existing in the bottom plate are not connected to those in the wall. Only one long pore complex continues from the bottom to the wall. In the bottom plate, the pores are aligned parallel in the horizontal direction (Figure 5-1.a.1); (2) The pores from the bottom link to the wall. The pores in the bottom are lying parallel to each other (Figure 5-1.a.2); (3) The pores in the bottom and wall do not connect to each other. The pores of the wall are vertically aligned starting from the side of the bottom part (Figure 6-1.a.3); (4) The bottom plate consists of two layers (Figure 5-1.a.4).

The wall fragments can be categorized into two groups in general: (1) irregular alignment of pores and sand grains, some grains showing specific orientation (Figure 5-1.b.1); (2) Most grains and large pores are oriented to the vertical direction (Figure 5-1.b.2). In general, the alignment of the pores and grains indicates the direction of the uniaxial compression and bending force applied by the potter in the walls during the modelling phase, where irregular directions of the pores and grains can be created easily by the hand shaping. Most inner structures of the selected samples were formed by these internal forces would be created by the pressing by potters with various intensities.

According to the combination of these identified alignments of pore complex and sand grains, representative shaping techniques for the bottom and wall fragments can be supposed accordingly: (1) The wall and bottom were formed into a separate part and the wall is added on the bottom later. Basically, both parts were shaped by pressing, to the horizontal direction for the bottom part; (2) The wall and bottom part were built together. The bottom was flattened by pressing from inward out; (3) The wall was pulled out or pinched slightly to the vertical direction and was added to the side of the bottom plate; (4) The wall and bottom were built separately and bound together later; (5) The bottom plate of the ceramic pottery was formed by two layers for the bottom plate. It is probable that the potters shaped the walls usually by hand. At the end, they pressed the wall, probably with the fingers or palms, for the compactness and finishing and bent. Regarding the ratio of coarse sand grains in the paste identified in the chapter 4 of this project, tensile stress created by pulling

would not be employed for the shaping of a pottery, because the paste would not be so flexible. The combination of several parts composed of coarse grains with similar orientation could be interpreted that the potters added the wall fragments side by side or stacked them from the bottom to the upside part such as coiling (Figure 5-1.b.1).

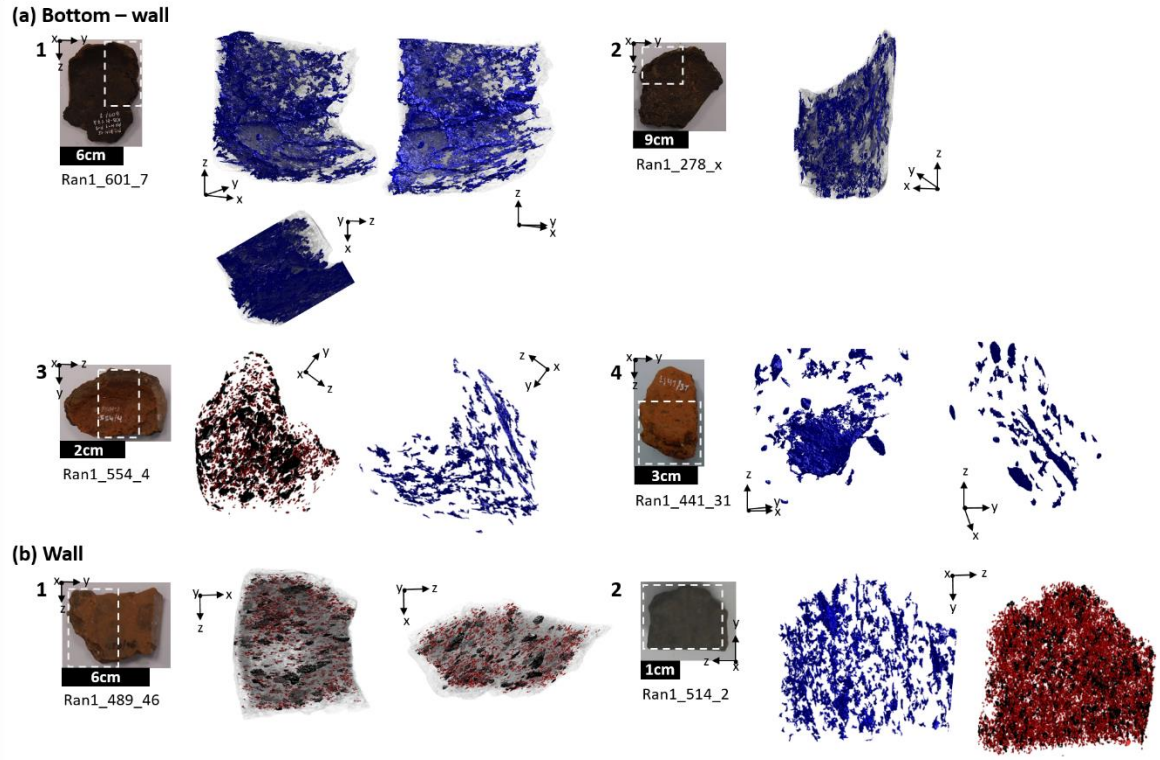

Figure 5-1. Photos of original ceramic sherds and segmented images of the large pore complex (blue) and sand grains (red and black) of the ceramics discovered at Ransyrt 1 (connectivity = 26). Region of interest (ROI) in the box of the white dashed line. (a) Bottom-wall fragments: 1. Separate formation of the bottom and wall part (wall on the bottom), oriented parallel pressure/stress from the surface (voxel size: 29.05^3 µm^3); 2. Continuous formation of the bottom and wall part (voxel size: 29.63^3 µm^3); 3. Separate formation of the bottom and wall part (wall next to the side of the bottom) (voxel size: 24.31^3 µm^3); 4. Two layers for the bottom building (voxel size: 28.21^3 µm^3); (b) Wall fragments: 1. Mixture of regular and irregular alignment of sand grains (voxel size: 19.33^3 µm^3); 2. Vertical orientation of the large pores in comparison to the alignment of the sand grains (voxel size: 9.49^3 µm^3).

5.2. Kabardinka 2: Results and discussion

In the similar way described above, the ceramics found at Kabardinka 2 can be categorized into a few groups of formation as well (Figure 5-2). Three types were identified for the main layout of the bottom—wall part: (1) the large pores connect both parts (Figure 5-2.a.1); (2) The pores from the bottom and wall part are not connected. The pores in the bottom show a rounded form, while the pores in the wall are elongated in the vertical direction (Figure 5-2.a.2); (3) The pores in the bottom part are not linked to the wall part. The bottom part contains pores aligned in parallel. Some of them on the surface are very sharp cuts (Figure 5-2.a.3).

The wall fragments excavated at this site contain clearer traces of their making than those found at Ransyrt 1 due to the finer grain size distribution of the ceramic pastes: (1) The pores are aligned in the vertical

direction (Figure 5-2.b.1); (2) The pores are aligned in the vertical direction from the side view, while from the front they are oriented in irregular direction (Figure 5-2.b.2).

The similar alignment of grains and pores indicate that the potters at Kabardinka 2 shaped the bottom and wall part of the ceramics using the same compression and bending force in similar ways: (1) Both parts were built separately and pressed together. The bottom was flattened leaving round traces and the wall was formed to a vertical direction. Some of the bottom plate was done by a tool with a sharp edge; (2) The wall part was drawn, pinched or bent from the bottom part; (3) Both parts were formed separately and the bottom was flattened by pressing into the horizontal direction.

There are no ceramic sherds containing any sign for the rotational kinetic energy which would let the grains in the pastes aligned in the second direction with 5–60° and which would prove the application of the wheel-throwing/shaping [1-4]. Thus, the ceramics from both sites were basically made by hand and shaped by the formation of the whole objects or by the modular slab building.

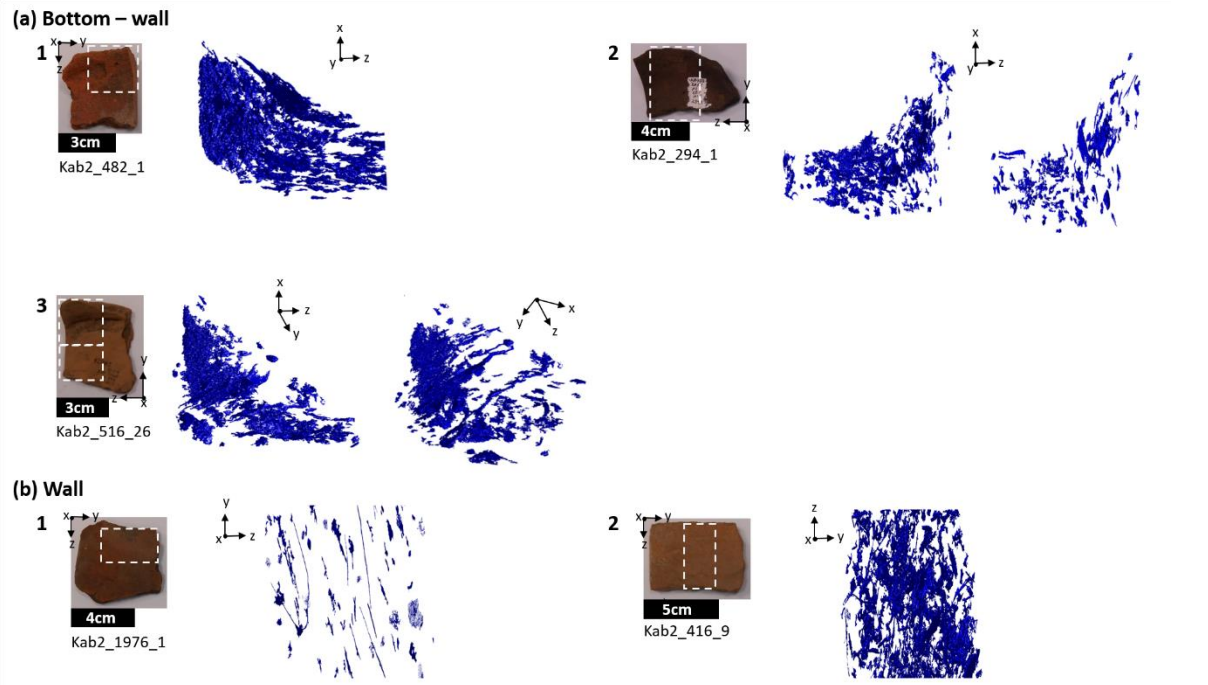

Figure 5-2. Photos of original ceramic sherds and segmented images of the large pore complex (blue) of the ceramics discovered at Kabardinka 2 (connectivity = 26). ROI is in the box with the white dashed line. (a) Bottom-wall fragments: 1. Continuous formation of the bottom and wall part (voxel size: 20.00^3 µm^3); 2. Separate formation of the bottom and wall part (wall next to the side of the bottom) (voxel size: 25.00^3 µm^3); 3. Separate formation of the bottom and wall part, oriented parallel pressure/stress from the surface (voxel size: 17.31^3 µm^3); (b) Wall fragments: 1. Alignment of the pores to the vertical direction (voxel size: 27.04^3 µm^3); 2. Rough alignment of the pores to the vertical direction with the random direction from the front view (voxel size: 25.00^3 µm^3).

5.3. References

1. Courty, M., Roux, V. Identification of wheel throwing on the basis of ceramic surface features and microfabrics. J. Archaeol. Sci. 22 (1995) 17–50. https://doi.org/10.1016/S0305-4403(95)80161-8

2. Roux, V., Courty, M.A. Identification of wheel-fashioning methods: Technological analysis of 4th-3rd Millennium BC oriental ceramics. J. Archaeol. Sci. 25 (1998) 747–763. https://doi.org/10.1006/jasc.1997.0219.

3. Carr, C. Advances in ceramic radiography and analysis: Applications and potentials. J. Archaeol. Sci. 17 (1990) 13–34. https://doi.org/10.1016/0305-4403(90)90013-U.

4. Berg, I. Looking through pots: Recent advances in ceramics X-radiography. J. Archaeol. Sci. 35 (2008) 1177–1188. https://doi.org/10.1016/j.jas.2007.08.006.

Chapter 6. Identification of the ceramic firing

6.1. Firing behavior of the illite based ceramics by the direct measurements of XRD, FTIR, SEM and Raman spectroscopy

The samples could be qualitatively ordered with respect to the decreasing illite XRD intensity that is taken as measure of increased thermal degradation (Figure 6-1). While illite peaks are decreasing in intensity, new minerals are crystallizing in the ceramics. Once the peak at 2.58 Å of illite is dispersed, a new peak of hematite (110) lattice plane starts to grow. The main peak of natural hematite at (104) occurs later as a sub peak, as the illite peak decrease and the hematite peak for (110) gains more intensity. In highly modified ceramics by firing, the intensities of the both peaks for hematite become equal. Reddish color caused by hematite formation indicates oxidizing firing during ceramic production. Higher firing degree is confirmed by spinel peaks of (113) and (004). Dark gray or blackish-brown samples show decrease of illite peaks without hematite crystallization, so that it is assumed that they were fired in the reducing atmosphere. If the samples contain calcite, gehlenite is detected corresponding to the decreasing illite peaks. In some samples containing hematite or spinel, the XRD background is smoothly increased between 15 and 35° for 2θ° indicating a vitreous phase. Other minerals such as K-feldspar, anorthite or clinopyroxene were not counted as the indicator of the thermal transformation in ceramics, because of they already existed in the ceramic pastes in various sizes.

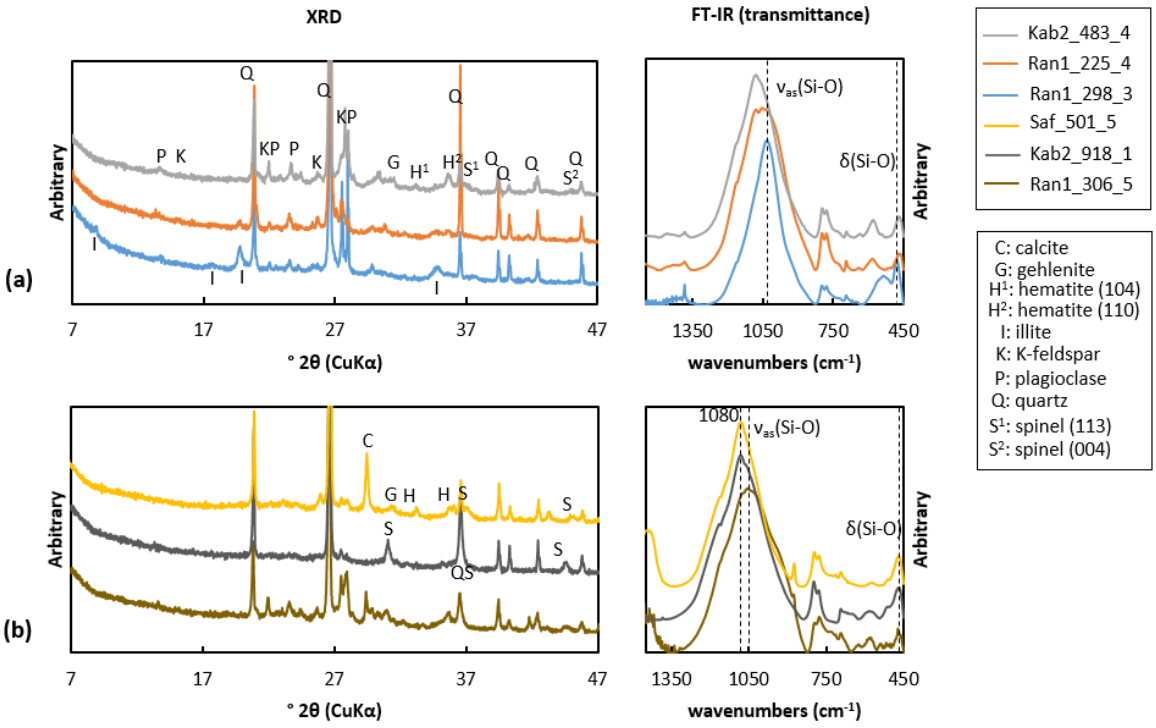

Figure 6-1. Example of comparison between XRD and FTIR according to firing conditions: (a) Three ceramic sherds from Ransyrt 1 fired in the oxidizing atmosphere with the estimated firing temperature of 300-675 °C (blue), 675-750 °C (orange), 1050-1300 °C (light grey); (b) Three ceramic sherds fired at over 1050 °C (estimation) in Ca-rich matrix/reducing atmosphere (dark yellow), Ca-poor matrix/oxidizing atmosphere (dark grey); Ca-rich/oxidizing atmosphere (yellow).

The main IR band in the transmission mode for the matrix ranges between 900 and 1080 cm^{-1}, mainly affected by the asymmetric stretching mode of Si-O bonds in clays, ν_{as}(Si-O). As proven by heating experiments [1-4], samples with strong XRD peaks for illite have the main IR band between 1027-1030 cm^{-1}, which is similar to the unfired illite, while samples with weaker illite peaks have this band shifted to the higher wavenumbers. Samples including hematite or spinel have often the main band at 1080 cm^{-1} assigned for quartz and sub band between 1050 and 1080. In some partly molten samples, only the main band at 1080 cm^{-1} appears without sub bands between 900 and 1100 cm^{-1}, thereby indicating the total collapse of the illite structure. The changes of wavenumbers and spectral shapes of the main band visible between 1027/1030 and 1080 cm^{-1} coincide with the changes in wavenumbers assigned to the bending mode of Si-O-Si and O-Si-O bonds, δ(Si-O-Si) and δ(O-Si-O) from the higher to lower wavenumbers within 460-480 cm^{-1}. This indicates that upon firing asymmetric deformation occurs in length and angle of Si-O bonds in the tetrahedral sheet. In Ca-rich ceramics containing gehlenite, the main FTIR band shifts to the lower wavenumbers close to 920-930 cm^{-1} that is related to Ca-aluminosilicates [5]. The clay dominant area could be focused by reflectance IR using a 70 µm aperture size. It was performed on polished cross sections of the same samples and yields similar spectra to the transmittance IR in all cases (Figure 6-2).

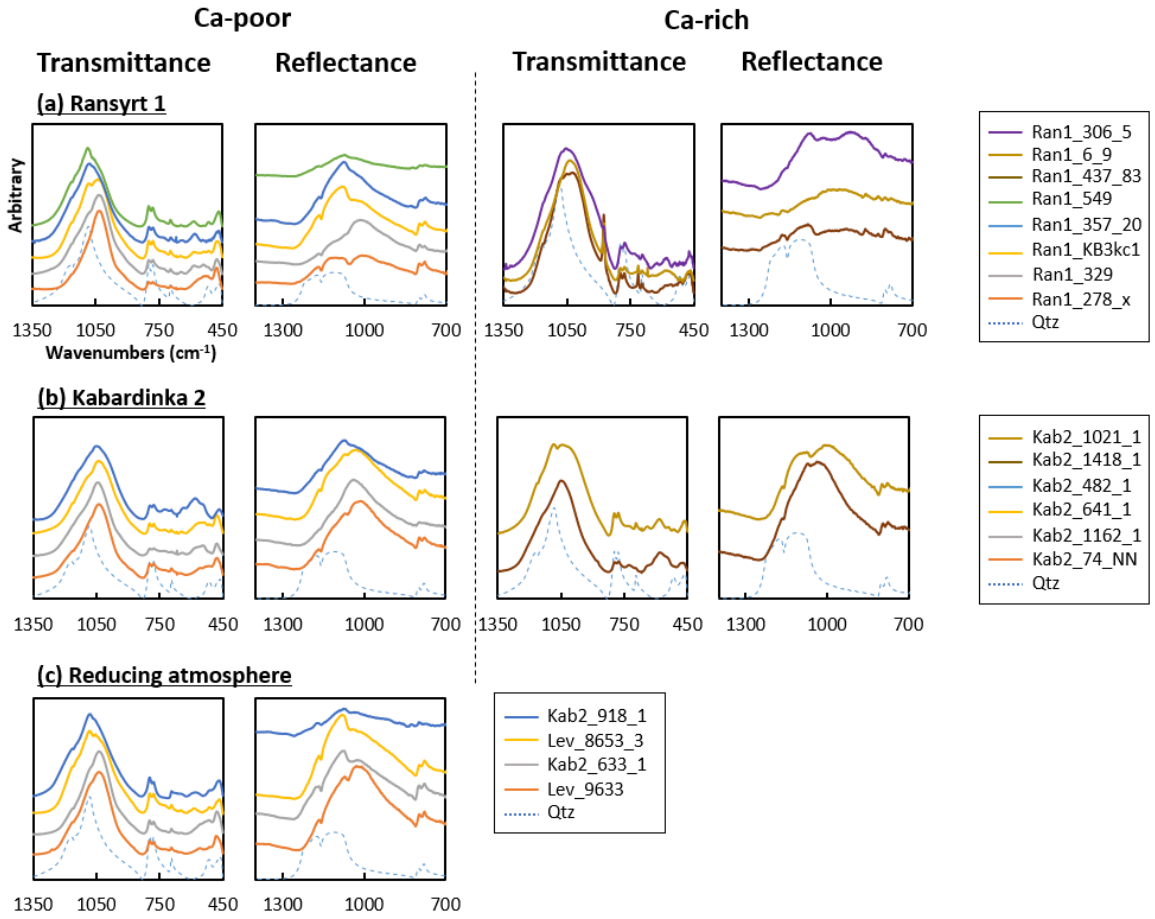

Figure 6-2. Comparison of FTIR spectra in the transmittance mode (intensity normalized to 1) and reflectance mode (intensity from a 70 µm aperture size) of representative samples ordered according to the estimated firing degree: (a) Ransyrt 1 ceramics: Ca-poor matrix by transmittance and reflectance IR; Ca-rich matrix by transmittance and reflectance IR; (b) Kabardinka 2 ceramics: Ca-poor matrix by transmittance and reflectance

IR; Ca-rich matrix by transmittance and reflectance IR; (c) Ceramics fired in the controlled reducing atmosphere: Ca-poor matrix by transmittance and reflectance IR.

SR-FIR and DRIFT-NIR spectra of the representative samples in different pyrometamorphic states in this study showed corresponding changes in illite specific vibrations for the far/mid/near IR range between 60 and 12000 cm^{-1} (Figure 6-3). In case of the samples from Ransyrt 1, the unsharp reflectance band shapes characteristic for illite, in comparison to muscovite, appear more clearly in the low fired ceramics and they lose their intensity in the high firing state, characteristic for its dehydroxylation process. However, illite specific FIR absorptions for the ceramics excavated at Kabardinka 2 show irregular changes which might be due to the impurities in quartz, mica or calcite. The significant IR bands for ν (H_2O) between 3000-3400 cm^{-1} and ν_{as} (Al/Mg/Fe-OH) at 3623 cm^{-1} in diffuse reflectance and their decrease according to the degree of the dehydroxylation were observed in the MIR absorbance spectra [6].

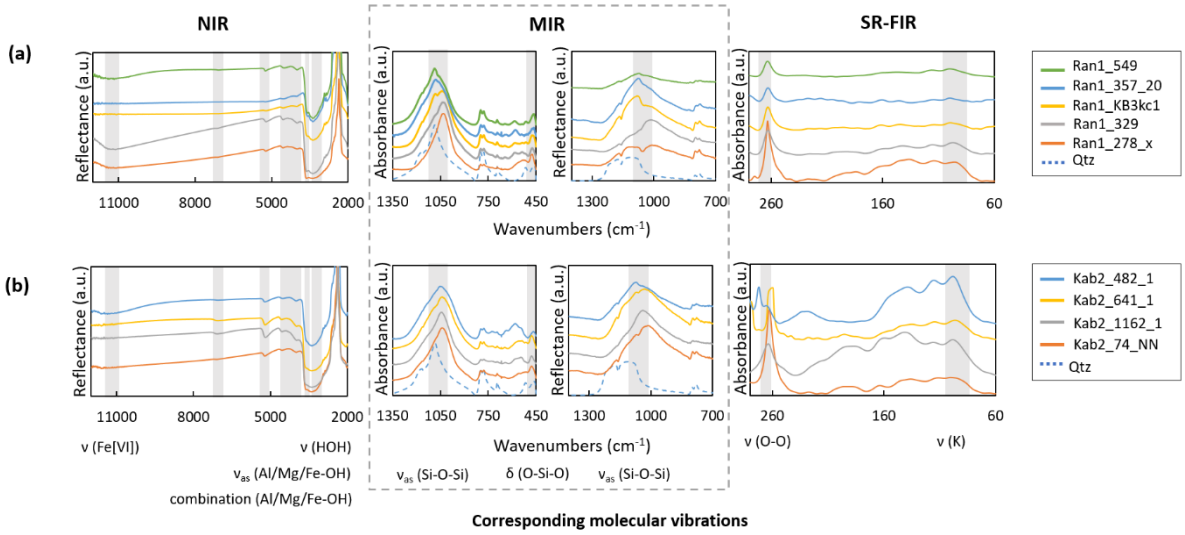

Figure 6-3. Comparison of SR-FIR absorption spectra, MIR specular reflectance and absorption spectra and NIR diffuse reflectance spectra of the representative samples for the different firing degrees excavated at (a) Ransyrt 1; (b) Kabardinka 2. In each IR range, the samples from both sites are ordered from the lower to higher firing degree. MIR data are taken from *Park et al.* [6].

Figure 6-4 shows the NIR diffuse reflectance spectra as a function of wavelength. The spectra in the wavelength scale show more clearly the changes due to the firing history. Especially in the Ca-poor samples, the reflection bands representing for the transition between Fe^{2+} and Fe^{3+} which became weaker according to the degree of firing, appears again in the samples fired at the high temperature (Figure 6-4.a-b) [7]. However, its spectral shape is much smaller and isolated in comparison to that of the structured Fe such as that in the octahedral layer and it indicates independent growth of the 6 coordinated ferric ion bearing mineral, hematite in the ceramics [8-10]. Moreover, this tendency of the shape change looks different, according to the absence and presence of Oxygen during firing. While the shape of the reflection band until the wavelength of 1 µm changes from a linear, then concave and then to flat after ν (H_2O) in the oxidizing atmospheric conditions (Figure 6-4.a,b), the band shape of the samples fired in the reducing condition showed the change from concave to linear increase (Figure 6-4.c). Regarding the pyrometamorphic degree, the vibrations for the combination mode of Al/Mg/Fe-OH bonds of the Ca-

poor samples loose in reflectance intensity as well, except of the samples containing newly crystallized hematite. Between the Ca-poor samples, the Ransyrt 1 ceramics show broader changes from lower to higher pyrometamorphic degree (Figure 6-4.a: Ca-poor) than those for Kabardinka 2 (Figure 6-4.b: Ca-poor), indicating that the thermal deformation and transformation of the Kabardinka 2 ceramics in the oxidizing atmosphere were not huge in comparison to the similar firing products at Ransyrt 1. Additionally, there were no distinguishable reflectance features related to the other Fe-bearing mineral phases such as goethite or ferrihydrite, in agreement with the XRD results of the same samples [6]. However, the reflectance spectra of the Ca-rich ceramics from both archaeological sites present an irregular pattern regarding the thermal conversion state by the firing (Figure 6-4.a,b: Ca-rich). The reflectance band from 1.38 nm to 0.88 nm which appear in these ceramics developed in the broader and more smooth form than the bands around 1 μm in Ca-poor samples under oxidizing firing. This broad reflection is more similar to that of the relatively Ca-rich ceramic object fired under reducing atmosphere (Figure 6-4c: Kab2_918_1) [6]. Another reduced firing object in the state of the liquid sintering shows almost flat and linear reflectance (Figure 6-4c: Lev_8653_3). The weakest trace of these IR bands was observed in this sample excavated at Levinsadovka in the Minus Peninsula. However, the highest firing temperature estimated by the Raman spectra would be given by the firing product in the oxidizing condition (Figure 6-4.a: Ran1_549; Figure 6-5). The appearance of the peak around 755 cm^{-1} indicates the early stage of the transformation of the clay ceramics into silica rich glass, which occurs between 1150 and 1250 °C in the experimental illite firing [11]. The fragile, thin and micrometer sized partial melts are composed mainly of aluminosilicates, measured by SEM-EDS, despite the possible consumption of Al at the octahedral site for the formation of spinel during the break-down of the clay mineral [11].

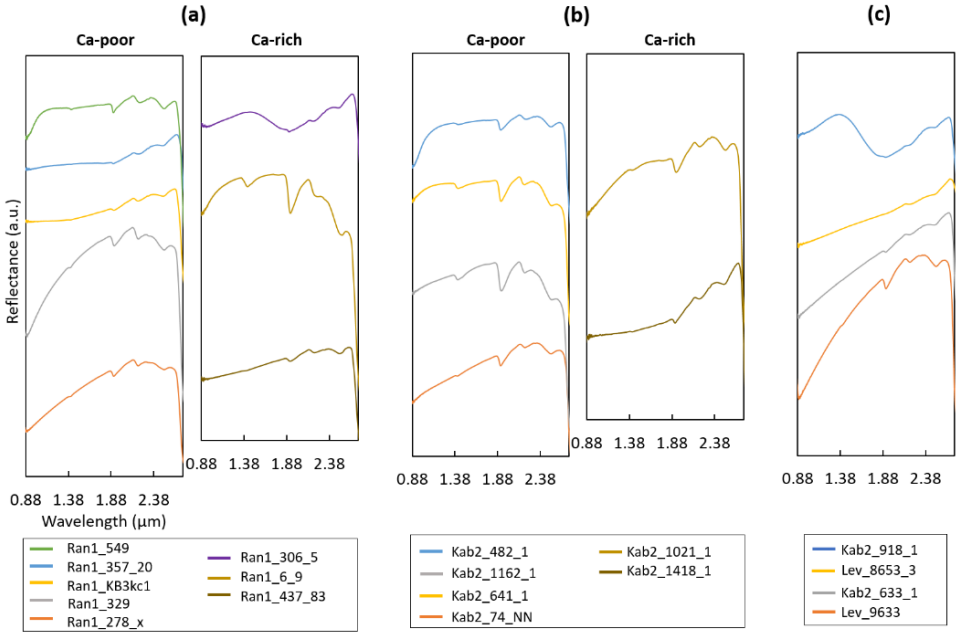

Figure 6-4. NIR diffuse reflectance spectra of the selected samples representing various pyrometamorphic states. The order of the spectra for the graph from lower to higher firing state. (a) Ca-poor and Ca-rich samples excavated at Ransyrt 1; (b) Ca-poor and Ca-rich samples excavated at Kabardinka 2; (c) Samples fired in the reducing atmosphere.

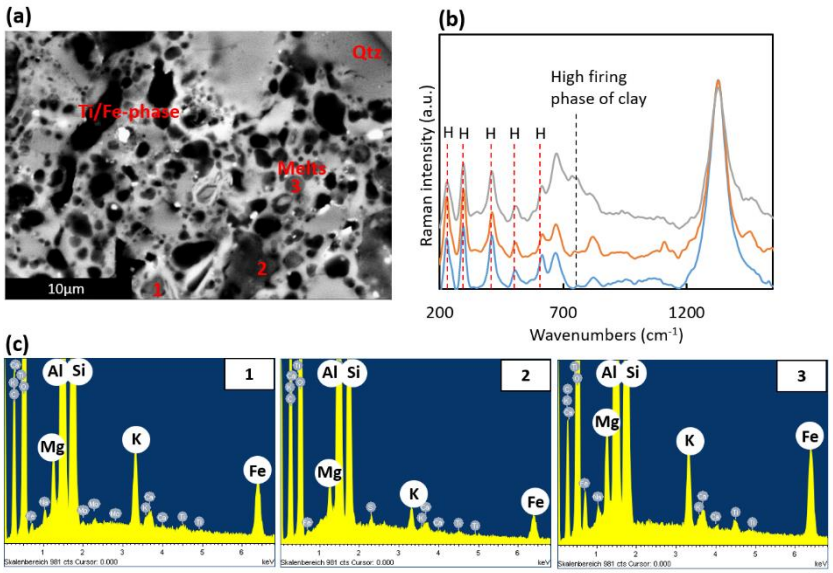

Figure 6-5. (a) BSE image and (b) corresponding Raman spectra of the ceramic sherd excavated at Ransyrt 1 (Ran1_549); (c) Closed pores filled by aluminosilicate melts (1-3 in (a)) (H:hematite; Qtz:quartz).

Micromorphology of the ceramic matrix as visualized by BSE images and chemical element maps supports this relation between thermal transformation and crystallization observed by the XRD and FTIR. This is summarized in figure 6-6, based on the parallelization of all three lines of evidence. If samples have strong illite XRD peaks and the main IR band close to 1027-1030 cm^{-1}, their ceramic matrix features open pores with elongated shapes. If the samples have weak illite peaks and their main IR band occurs at higher wavenumbers, the fabric is characterized by globular and closed pores, often filled with aluminosilicate melts containing Mg, Fe and Ca as minor components, as SEM-EDS proved. The compositional ratio of (Fe+Mg+Ca)/Al or Si is ≤ 0.3 wt. %. In element distribution maps of Ca-poor samples containing hematite, Al is enriched in closed pores indicating the formation of Al-rich melt. In samples devoid of hematite but with their main IR band occurring at similar wavenumbers to that of hematite containing samples, the fabric shows already less pores between quartz or feldspar sand/silt grains and clay matrix, although the clay structures still exist in the samples. In the element distribution maps of these samples, there are less gaps between sand grains and clay matrix, in spite of still existing huge open pores. Samples containing spinel without hematite and illite show a matrix with closed pores, too. In Ca-rich ceramics, Ca-carbonate combines with aluminosilicate clays and gehlenite is formed in a globular or tabular shape at the surface of calcite grains. Spinel appears in all kinds of ceramics with highly progressed partial melting. Slight variations in d-spacings indicate various spinel solid composition. In this project, most calcite grains are partly decomposed forming a reaction rim at the grain boundary and interdiffusion of Ca^{2+} ions from original calcite grain into the porous ceramic matrix[24] and Mg^{2+} ions from the clays into calcite occurs [12] (Figure 6-7). In case of calcite grains during firing over 650-700 °C in the ceramic paste, similar vibrational changes were observed (Figure 6-7.a). In the reaction rim, reflectance IR intensity of Ca-carbonate vibrations decreases, while the possible ν_{as}(Si-O) gains the intensity (Figure 6-7.b). Similar phenomena were reported for the ceramic pottery measured with FTIR (transmittance) and found the reason in Mg incorporation from clays into calcite. Ca and Mg distribution maps show the interdiffusion between these two elements through the

reaction rim (Figure 6-7.c) [12]. The chemical composition of calcite grains and grain boundaries was measured by SEM-WDS with a beam size 10 µm, in comparison to the total weight % of each point without contribution of CO_2. As a consequence, IR vibrations of $(CO_3)^{2-}$ groups, especially between 1430-1450 cm^{-1}, move to slightly higher wavenumbers forming a broader band shape [13-14].

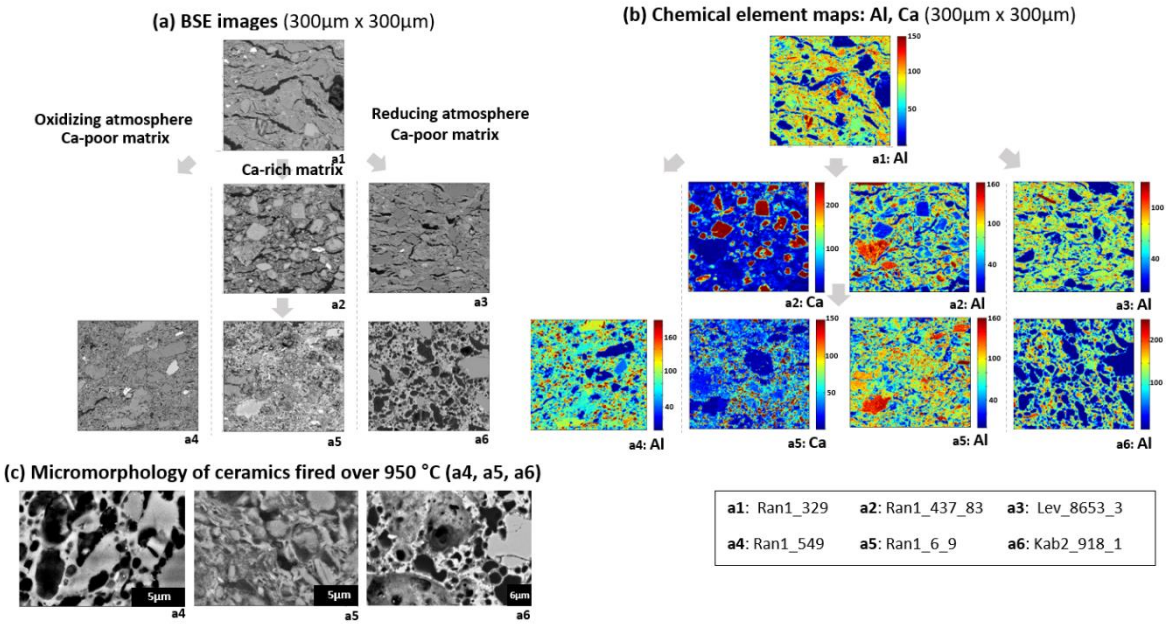

Figure 6-6. Comparison of general morphological changes of representative samples according to estimated firing temperature, Ca presence, and atmospheric conditions: (a) BSE images (300µm x 300µm); (b) Al distribution maps of together with Ca maps for Ca-rich matrix (300µm x 300µm); (c) comparison of micromorphology (BSE) between ceramic sherd fired over 950 °C (estimated).

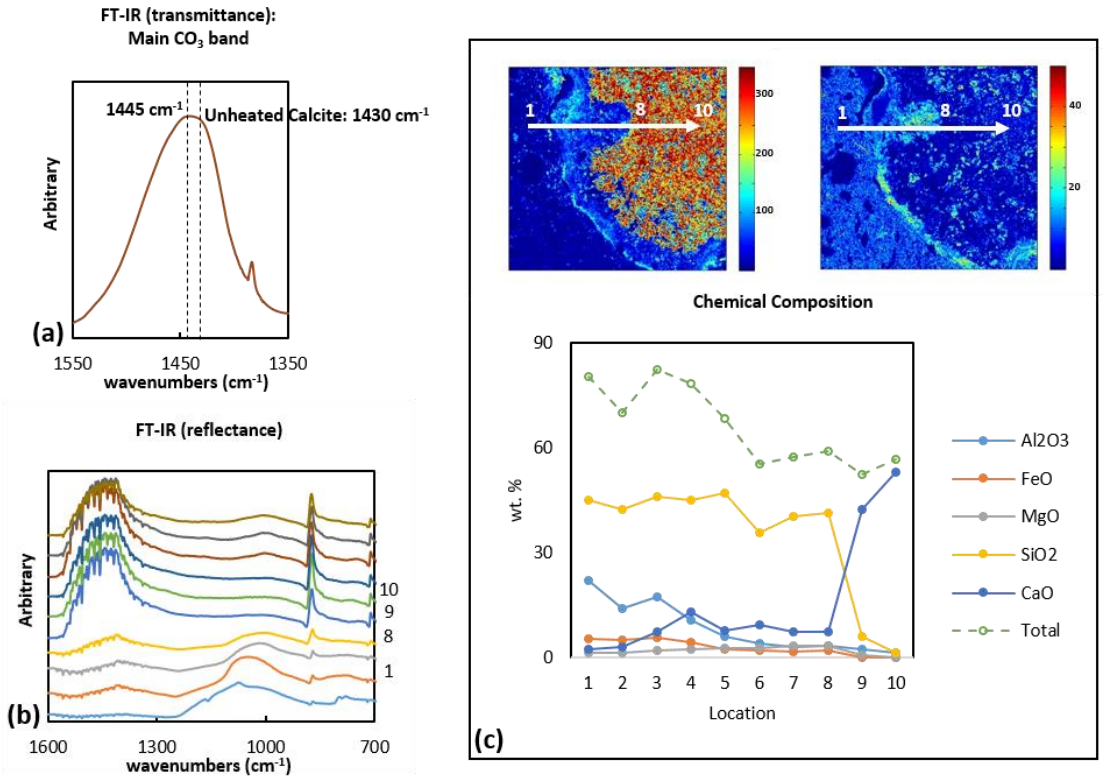

Figure 6-7. Thermal decomposition of calcite: (a) FTIR (transmittance) of the ceramic paste containing decomposed calcite grains; (b) FTIR (reflectance) from different positions from the boundary through the whole calcite grain (c); (c) Ca, Mg distribution maps (700 µm x700 µm) and chemical compositional changes according

to different positions from the boundary to the calcite core measured by SEM-WDS (beam size 10 µm, without CO_2 composition).

Table 6-1 summarizes the results from the micropore morphology analysis and XRD describing the presence and absence of indicator minerals, FTIR (transmittance) of bulk ceramic powder mixed with KBr, in relation to the macroscopic colors of ceramics cross sections for representative samples.

Sample No.	Ceramic color (cross section)	Micropore morphology	XRD (indicator minerals, peaks)	FTIR (transmittance, Si-O stretching, cm^{-1})
Ran1_437_83	red brown (surface), dark brown	elongated open	ill(020)/(110), clc, geh trace	1024 (main), 1052&1080 (sub)
Ran1_225_4	dark brown, brown	elongated open, closed	ill (020)/(110) (130)/(13$\bar{1}$) , hem (104) (110), clc	1054 (main), 1078 (sub)
Ran1_261_40	light brown	elongated open	ill (001) (002) (020)/(110) (130)/(13$\bar{1}$)	1035 (main)
Ran1_357_20	light/red brown	elongated open, closed globular	clc, geh, spl, hem (104) (110)	1079 (main), 1063 (sub)
Ran1_6_9	orange red	closed globular	ill (020)/(110), clc, hem (104) (110)	1034 (main)
Ran1_278_x	dark brown	elongated open	ill (001) (002) (020)/(110) (130)/(13$\bar{1}$)	1031 (main)
Ran1_554_4	brown (surface), dark brown	elongated open	ill (001) (002) (020)/(110) (130)/(13$\bar{1}$), hem (110) trace, clc	1028 (main)
Ran1_217_17	brown	elongated open	ill (001) (020)/(110) (130)/(13$\bar{1}$) hem (110) trace	1035 (main), 1080 (sub)
Ran1_244_9	red brown, dark brown	closed globular	hem (104) (110), clc	1035 (broad main between 1010 and 1050)
Ran1_326_9	light brown, gray brown	elongated open	ill (020)/(110) (130)/(13$\bar{1}$)	1034 (main), 1055 (sub)
Ran1_167_4	brown, gray brown, dark brown	elongated open, closed globular	ill (020)/(110) (130)/(13$\bar{1}$), hem (110) trace	1040 (main), 1050 (sub)
Ran1_509_9	gray brown	closed irregular	ill (020)/(110) (130)/(13$\bar{1}$), hem (110) trace	1034 (broad main between 1013 and 1053)
Ran1_17_2	light brown (surface), dark brown	elongated open	ill (001) (002) (020)/(110) (130)/(13$\bar{1}$), hem (110) trace	1034 (main)
Ran1_306_5	brown gray	closed globular	clc, geh, spl, hem (110)	1054 (main), 1076 (sub)
Ran1_549	orange red	closed globular	hem (104) (110)	1087 (main), 1062 (sub)
Ran1_470_ceramic	pink red	closed irregular	clc, hem (104) (110)	1080 (main), 1055 (sub)
Ran1_370_1	dark brown gray	elongated open, closed	hem (104) (110), clc, geh trace	1041 (broad main between 1030 and 1053)
Ran1_449	red brown, brown	elongated open	ill (001), (020)/(110), (130)/(13$\bar{1}$), hem (104) (110)	1041 (main), 1080 (sub)
Ran1_KB3kc1	red brown (surface), dark brown	elongated open	ill (020)/(110) (130)/(13$\bar{1}$), hem (110) trace	1039 (main), 1083 (sub)
Ran1_514_3	dark brown, brown	elongated open	ill (001) (020)/(110) (130)/(13$\bar{1}$), hem (110)	1039 (main), 1083 (sub)
Ran1_514_1	dark brown	elongated open	ill (020)/(110) (130)/(13$\bar{1}$), hem (110) trace	1035 (main), 1078 (sub)
Ran1_527_1	dark brown, brown	elongated open	ill (001) (020)/(110) (130)/(13$\bar{1}$), hem (110) trace	1034 (main), 1080 (sub)
Ran1_329	dark brown	elongated open	ill (001) (020)/(110) (130)/(13$\bar{1}$), hem (110) trace	1035 (main), 1074 (sub)
Ran1_514_2	dark brown	elongated open	none	1090 (main), 1040&1060 (sub)
Ran1_dmp1	red brown, dark brown	elongated open, closed globular	ill (001) (020)/(110) (130)/(13$\bar{1}$), hem (104) (110)	1053 (main), 1080 (sub)
KAE2007_2113_1	dark brown	elongated open	ill (001) (002) (020)/(110) (130)/(13$\bar{1}$), hem (110) trace	1085 (main), 1054 (sub)

KAE2008_844_1	light brown	elongated open	ill (001) (002) (020)/(110) (130)/(13$\bar{1}$), hem (110) trace	1084 (main), 1023 (broad sub 1005 and 1043)
KAE2008_633_1	black	elongated open	ill (020)/(110) (130)/(13$\bar{1}$), hem (110)	1039 (main)
KAE2007_1697_1	red brown (surface), dark brown	elongated open	ill (020)/(110) (130)/(13$\bar{1}$) trace	1084 (main), 1054 (sub)
KAE2007_1235_1	gray brown	elongated open	ill (001) (002) (020)/(110) (130)/(13$\bar{1}$) trace, clc	1039 (main)
KAE2007_1418_1	brown (surface), dark brown	elongated open, closed	ill (020)/(110) trace (130)/(13$\bar{1}$), hem (104) trace (110)	1049 (main)
KAE2007_NN	brown	elongated open	ill (001) (002) (020)/(110) (130)/(13$\bar{1}$)	1040 (main)
KAE2007_28/2	dark brown (surface), light brown	elongated open	ill (001) (002) (020)/(110) (130)/(13$\bar{1}$)	1038 (main)
KAE2007_797_1	red brown (surface), dark brown	elongated open	ill (020)/(110) (130)/(13$\bar{1}$) trace, clc	1041 (main), 1080 (sub)
KAE2007_918_1	dark gray	closed globular	spl	1084 (main), 1066 (sub)
KAE2007_482_1	dark red (surface), red	elongated open, closed globular	ill (130)/(13$\bar{1}$), hem (104) (110)	1053 (main)
KAE2008_1195_6	red brown (surface), dark brown	elongated open	ill (001) (002) (020)/(110) (130)/(13$\bar{1}$), hem (110) trace	1031 (main)
KAE2008_1162_1	black (surface), light brown	elongated open	ill (001) (002) (020)/(110) (130)/(13$\bar{1}$)	1030 (main)
KAE2008_516_2	red brown (surface), dark brown	elongated open	ill (001) (002) (020)/(110) (130)/(13$\bar{1}$), hem (104) (110)	1039 (main)
KAE2008_1021_1	light brown, gray brown	elongated open, closed	ill (020)/(110) trace	1084 (main), 1038 (broad sub between 1005 and 1055)
KAE2008_1152_1	light brown	elongated open	ill (001) (020)/(110) (130)/(13$\bar{1}$) trace	1020 (broad main between 1047-990), 1080 (sub)
KAE2008_516_26	light brown	elongated open	ill (001) (020)/(110) (130)/(13$\bar{1}$), hem (110)	1043 (main)
KAE2008_483_3	pink red (surface), dark gray	elongated open	ill (020)/(110) (130)/(13$\bar{1}$) trace	1080 (main), 1055 (sub)
KAE2008_641_1	light brown	elongated open	ill (020)/(110) (130)/(13$\bar{1}$), hem (104) trace (110)	1045 (main)
Lev_9633	Black, dark brown	elongated open	ill (001) (002) (020)/(110) (130)/(13$\bar{1}$)	1039 (main)
Lev_7718	light brown (surface), dark brown	elongated open	ill (001) (020)/(110) (130)/(13$\bar{1}$)	1042 (main)
Lev_8653_1	light brown, black	elongated open	ill (001) (020)/(110) (130)/(13$\bar{1}$), clc	1031 (main)
Lev_8653_3	black, dark gray	elongated open	ill (020)/(110) (130)/(13$\bar{1}$) trace, clc	1084 (main), 1054 (sub)
Lev_8653_4	light brown (surface), dark brown	elongated open	ill (020)/(110)	1084 (main), 1058 (sub)
Saf_501_5	orange red	closed globular	clc, geh, hem (104) (110), spl	1085 (main), 1078 (sub)
Saf_502_3	red brown (surface), dark brown	elongated open, closed	ill (020)/(110) trace (130)/(13$\bar{1}$) trace, hem (104) trace (110) trace, clc	1085 (main), 1060 (sub)

Table 6-1. Description of cross section colors, micropore morphology, XRD peaks of pyrometamorphic minerals and main and sub bands of FTIR (transmittance) vibrations for the representative samples (clc: calcite, geh: gehlenite, hem: hematite, ill: illite).

6.2. Pore topology within the ceramics as indicator for the pyrometamorphic degree

Pyrometamorphism of archaeological ceramics indicating firing degree and conditions has been estimated by chemical and mineralogical changes and clay sintering by various analytical instruments such as XRD, SEM and FTIR [15-16]. Pore topology is one of the key variables related to the

pyrometamorphic degree of the ceramics, because firing temperatures and atmospheres change pore shapes and orientations caused by thermal expansion and sintering of clay minerals [17-19]. If particles with identical shape and composition are sintered, the interstitial topology changes in three steps: (i) the contact between neighboring particles; (ii) the interconnected channels with cylindrical pores; (iii) the formation of closed pores [17,18]. Clay sintering has a similar process as well [19]. The initial stage is the formation of sharply concave necks between the individual particles, while the intermediate stage forms a 3D interpenetrating network of solid particles and continuous-, channel-like pores with high curvatures. The final stage of sintered clay shows a huge decrease in porosity with isolated and closed forms. Because the prehistoric ceramics contain various scales and anisotropic shapes, the densification process and the coarsening process in the sintering will occur as a mixed process [19]. Despite of the difficulties in the morphological description of this heterogeneous system, the morphological changes in the clay matrix were described by several simplified steps during ceramic firing in the same study [20]: (i) drying and shrinking of the clay paste; (ii) dehydration in the low temperature firing interval between 100 and 200°C, creating interstitial pores; (iii) continuous increase in porosity by chemical reactions such as dehydroxylation of clay minerals between 400 and 800°C; (iv) liquid phase sintering forming interconnected pores of irregular shape and partial melts; (v) micro-fabric formation ranging from non-vitrified to completely vitrified final state. The selected ceramic samples were ordered according to the different micro-morphology and mineralogical changes, which range from low firing through thermal expansion and dehydroxylation to the early melting stage [6]. In general, the fabrics of the samples could be classified into four types in terms of micro-pores and colors of ceramic matrix as well: (1) elongated open pores with the matrix in dark brown/brown/gray/black; (2) closed end-elongated pores with the matrix in light brown/reddish brown/dark red; (3) open pores/closed end-elongated/closed globular pores with the matrix in light gray/light red; (4) closed globular pores in orange/dark gray.

The morphological changes led by clay sintering can be described by the shape parameters such as pore size/area/volume distribution, sphericity 1 and sphericity 2. Additionally, the complex pore geometry can be expressed by the pore topology function of the archaeological ceramics such as Minkowski functionals [21-22]. Especially, the Euler characteristic (χ) provides an unbiased estimation of pore topology, applied to a 3D cutout of arbitrary shape and volume [22]. It was calculated from 2D and 3D images using the following formula:

$$\chi_{2D} = n(\text{objects}) - n(\text{pores}), \quad (6\text{-}1)$$

$$\chi_{3D} = n(\text{objects}) - n(\text{tunnels}) + n(\text{cavities}), \quad (6\text{-}2)$$

where χ_{2D} and χ_{3D} represent the Euler characteristic in 2D and 3D and n(objects), n(tunnels) and n(cavities) are the total numbers of objects, tunnels and cavities, respectively. However, due to the complex structure of ceramics, these elements for the Euler characteristic in 2D and 3D are difficult to count directly. For the application of this characteristic in the heterogeneous ceramic structure, the

Equation (5) is replaced by the Euler–Poincaré formula based on a cubic form of the voxel which can be acquired directly from the reconstructed images [23-24]:

$$\chi_{3D} = n(\text{vertices}) - n(\text{edges}) + n(\text{surfaces}) - n(\text{volumes}), \quad (6\text{-}3)$$

where n(vertices), n(edges) and n(surfaces), n(volumes) mean the total number of vertices, edges, surfaces and volumes of the measured ceramic objects. Due to the very heterogeneous shapes existing in the samples, this calculation used the six-connectivity of voxels defining the areas of pores and ceramic matrix. The orientation of the pores which were mainly decided by the forming and shaping actions of the potters can provide additional evidence regarding the sintering stage. In 2D image analysis, the angle between the x-axis, the cross profile of the ceramic thin section, and the major axis of the ellipse that has the same second-moments as the pore region, referred as θ, was used. It ranges from –90 degrees to +90 degrees. In 3D data processing, Euler angles were taken for the x- (ϕ), y- (θ) and z-axis (ψ) based on the right-hand rule [25-26]. In order to normalize porosity acquired from the different areas and volumes of ROI, Euler characteristic is divided by the corresponding area of the object for 2D and volume for 3D. In 2D images for the area of 300x300 μm^2, average and standard deviation of sphericity 2 of individual pores become smaller due to clay sintering, while Euler characteristic suddenly decreases just before the beginning of the liquid sintering and after that it increases again (Figure 6-8). Due to the different grain size distribution, the numeric thresholds suggested by this Euler characteristic are formed differently according to the archeological sites.

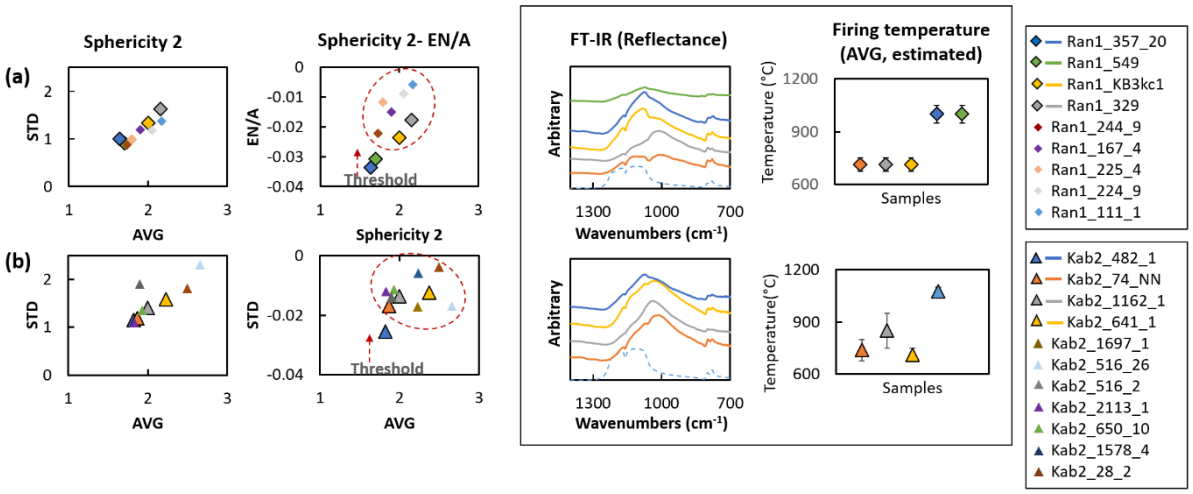

Figure 6-8. Average and standard deviation of sphericity 2 of pores and comparison between Euler number per unit area of the pores (A = 300x300 μm^2) in average and sphericity of pores in average. Calculated from the pores (2D) present in cross thin sections of the samples from (a) Ransyrt 1, (b) Kabardinka 2. These parameters of four samples for each site (bigger maker with a boundary border) were compared to the reflectance Fourier-transform infrared spectroscopy (FTIR) (aperture size: 70x70 μm^2, reference: silver mirror) [6].

In figure 6-9, the 2D images and 3D segmented pores of the same samples are compared to each other. According to the increase in the degree of sintering, the pore volumes decrease in size. These samples contain a relatively similar percentage of sand size distribution (Figure 6-10). The degree in orientation of the closed pores, θ decreases as well. The sample with the highest pyrometamorphic state (Ran1_549) shows the highest variations of the localized Euler characteristics. Interestingly, the Euler characteristic calculated from the 2D and 3D images does not show a linear relation and rather is related to the higher

interconnectivity of the pores and grains in the 3D images. This reflects the faster disappearance of pore connectivity in the x–y-plane of the wall fragment than in z-direction. These changes of the pore shapes to an ellipsoidal form is controlled by vacancies diffusion ruling pore morphology during sintering, because the large pores created with different curvatures favor this shape according to the increasing sintering degree [27]. Figure 6-11 shows a tendency of the closed pore networks in 3D volume to become more elongated in accordance with metamorphic degree, while their surface area and volumes decreases. The orientation degree, ψ, of the individual open and closed pores in the ceramics decreases according to the increasing pyrometamorphic degree. This means a rotation around the z-axis in the clockwise direction according to the increasing firing temperature.

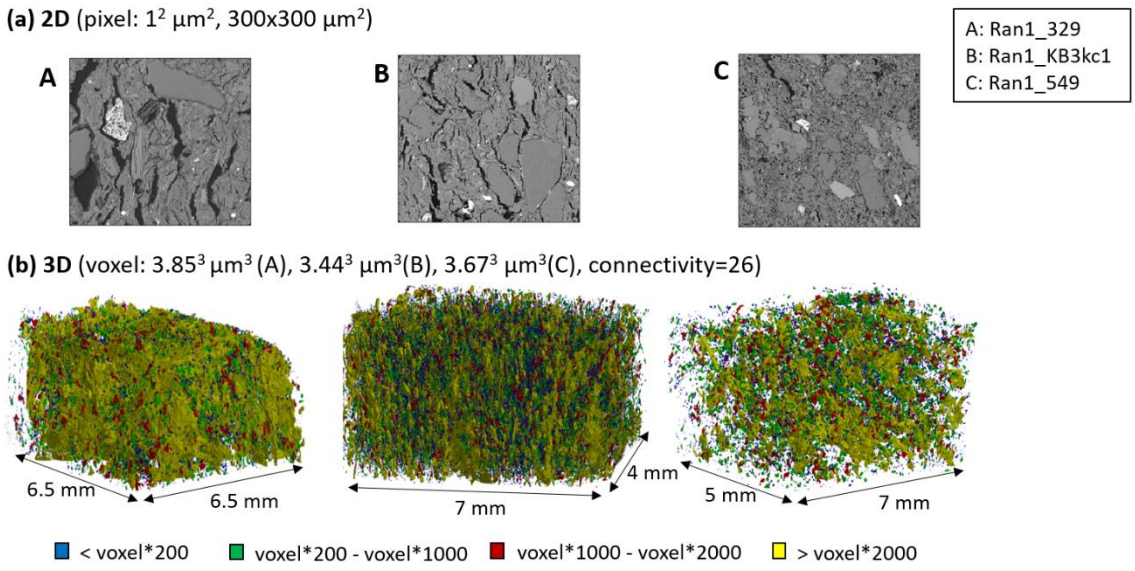

Figure 6-9. Comparison of the pore topology between (a) 2D and (b) 3D images of three samples varying in the degree of pyrometamorphic degree/sintering [6]. Estimated firing temperature for A: 700–850 °C, B: 700–850 °C and C: 950–1050 °C. The segmented pores show the difference of the firing degree between A and B more clearly.

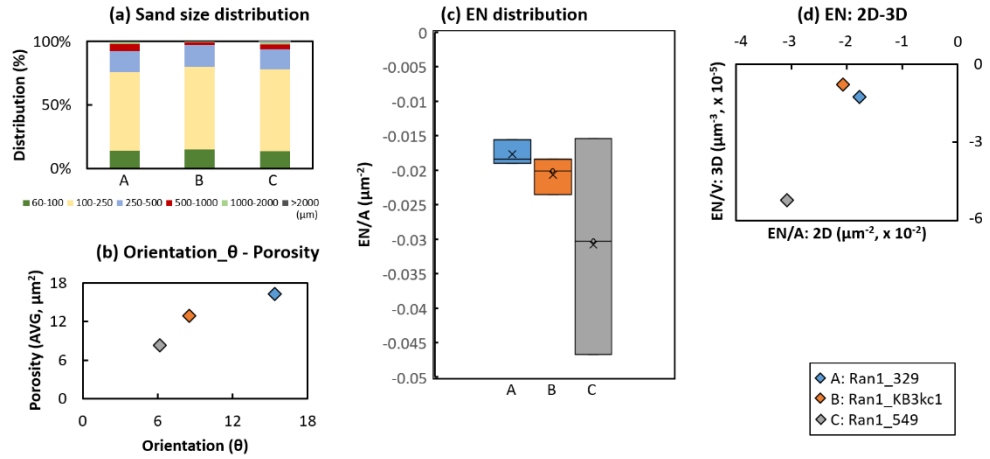

Figure 6-10. Comparison of sand size distribution calculated by (a) 2D images and (b) orientation of two-dimensional pores, (c) spatial distribution of the localized Euler number within a two-dimensional unit area and (d) Euler number (average) derived from 2D images and that from 3D images (connectivity = 6). Samples (A, B, C) from the Figure 6-9.

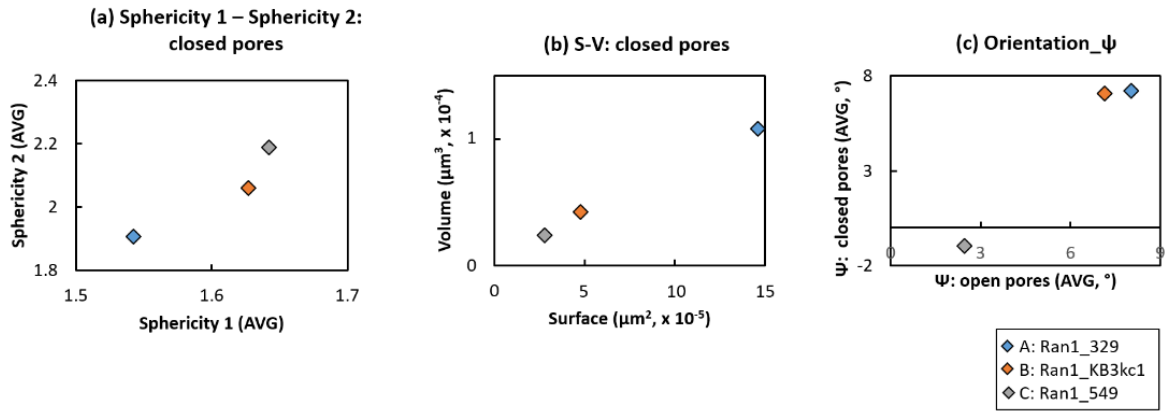

Figure 6-11. Relationship between the average of (a) sphericity 1 and sphericity 2 of closed pores and (b) surface area and volume relation of the closed pores and (c) the comparison of orientation degree ψ and the closed and open pores in average. All parameters derived from 3D scanning with the connectivity 26. Samples (A, B, C) from the figure 6-9.

These results show that the segmented pores in 2D and 3D and their parametrization according to the sintering stages are useful as an additional indicator supporting the estimation of the degree of pyrometamorphism of the archaeological ceramics. Although the parameter values from the 2D and 3D image analysis provide results slightly different from each other, which is probably caused by the different unit cell size and counting of the objects, they can both be employed for the classification of the archaeological ceramics according to the firing degree. The Euler characteristic provides the numeric thresholds of the sintering stages of each sample. Especially, the transition into the liquid sintering of the ceramic matrix can be distinguished by the huge decrease in this property, which is important for identifying high firing ceramics at the site. Despite the complex pore structure caused by the heterogeneous composition in the ceramic paste, ceramics with similar degree of heterogeneity can be analyzed by this parameter describing the pore topology and related sintering.

In comparison to the Ca-poor ceramics, the samples containing considerable amounts of Ca-carbonates contain additional pore type caused by the thermal dissociation carbonate grains [6]. This type of porosity is mainly controlled by a combination of the firing degree and the size of carbonate grains. Thus, the shape parameters of the Ca-carbonate rich ceramics cannot be compared to each other as well as the Ca-poor samples.

6.3. Spatial distribution of the pyrometamorphic degree within an archaeological ceramic object

Figure 6-12 shows the reflectance IR profile across a single sherd with a 70x70 µm^2 aperture size. Spatial distribution of different IR bands in terms of intensity, wavenumbers and shape was identified within a single sherd. The main band attributed to ν_{as}(Si-O) varies from the left to the right side on the cross section. The band intensity around 1020 cm^{-1} decreases, while the intensity around 1080 cm^{-1} assigned to quartz increases. BSE images from areas along this profile depict a parallel switch from open to closed pores in the matrix.

The pyrometamorphic degree of each selected sample measured by the reflectance FTIR (70x70 µm^2, silver mirror) and corresponding deformation degree estimated by multiproxy methods support this

parametric change [6]. However, this property has a dependency on the grain size and shape, thus ceramics found at Ransyrt 1 and Kabardinka 2 show a different distribution of Euler characteristic before the sintering. Moreover, the firing state within a single sample is heterogeneous, so that the average temperature of the whole ceramic sherd does not always coincide with the local firing state [6]. Despite of this high degree in the heterogeneity, these parameters provide thresholds of the sintering degree of the ceramic pastes, especially the beginning of the liquid sintering phase. The Euler characteristic calculated from each area within a same sample provides access to a spatial distribution that indicates the localization of the pyrometamorphic degree.

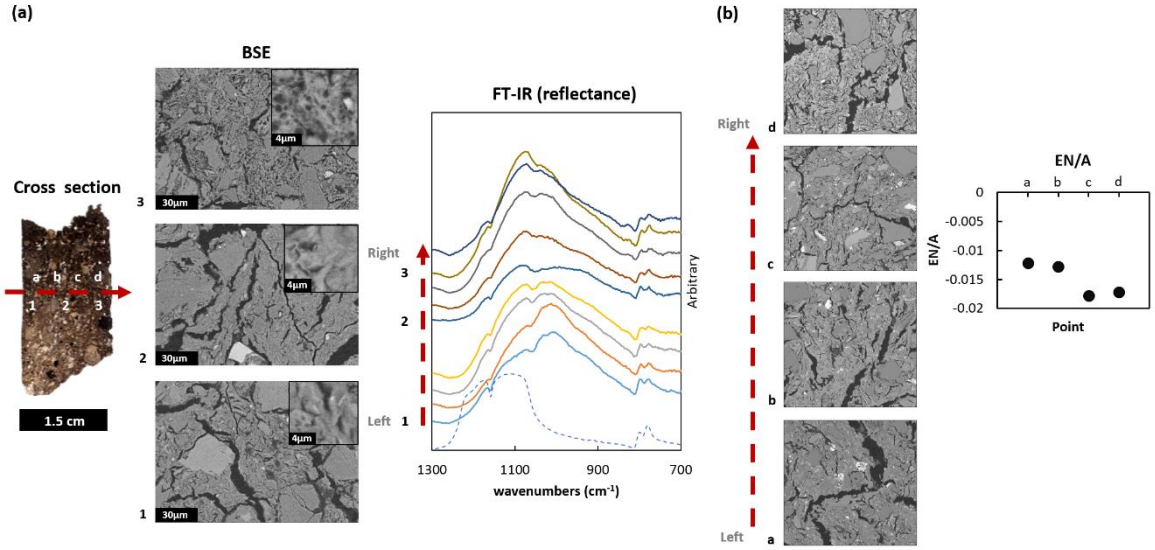

Figure 6-12. (a) Cross section profile of the reflectance FTIR (aperture size: 70x70 µm^2, reference: silver mirror, dashed ine in blue: quartz) [6] and corresponding BSE images for the left side (1), middle (2) and right (3) of the sample (Ran1_167_4); (b) Cross section profile of the Euler characteristic per unit area and related BSE images from the left side (a) through left middle (b) and right middle (c) to the right side (d) of the same sample in a same direction. Calculated from the two-dimensional area of 300x300 µm^2 on the cross thin section.

This method could distinguish the different ceramic part fired in the different atmospheric conditions. For example, a slip ware composed of a red-pink slip and grey body and excavated at Kabardinka 2 had very similar mineralogical and chemical composition both for the body as well as the slip part (Table 4-1). Only the mechanical separation and the differences in the pattern of Fe distribution indicated a separate process for the preparation of the both parts (Figure 6-13.a,c.1-3). Moreover, IR vibrations of ν_{as}(Si-O) could prove that the body part was fired in the reducing atmosphere and the slip part in the oxidizing (Figure 6-13.b).

In many cases, cross sections of the ceramic sherds excavated at both archaeological sites display the two or three optically distinguishable layers with brown/reddish/orange and black/dark gray/gray color (Figure 6-14). Some of them displaying layers of light gray and light reddish/orange color and show different degrees of thermal transformation and collapse depending on the layer, seen in BSE images or MIR reflectance for ν_{as} (Si-O) between 1030 and 1080 cm^{-1} (Figure 6-14.a.1-2: Ran1_dmp1; Figure 6-14.b.3: Kab2_483_3). Either the ceramic morphology has partly vitreous state or the intensity of ν_{as} (Si-O) decreased with the band shift to the higher wavenumbers. However, in ceramics with a similar layer

combination of the darker brown/black and reddish-brown colors, no changes in the morphology or MIR were observed (Figure 6-14.a: Ran1_KB3kc1; Figure 6-14.b: Kab2_516_2). This color distribution in the cross section is related to the black coring in the clay ceramics, caused by the oxidation of carbon at the expense of the valence charge of Fe structured in clay and preexisting Fe-bearing minerals such as goethite in the absence of oxygen [28-29]. Furthermore, the uneven distribution of the oxygen partial pressure and the reduction of ferrous minerals as a consequence lead to similar shapes of the reflection band assigned to ν_{as} (Si-O) of the ceramics fired in a reducing atmosphere (Figure 6-14.c). While the dark black ceramic sample was not highly transformed by firing (Figure 6-14.c: Kab2_633_1), the sample with light gray color in cross section shows highly a vitreous state with closed pores partially filled by melts characterized by the ν_{as} (Si-O) band shifts (Figure 6-14.c: Kab2_918_1). In addition to the thermal transformation and crystallization in the ceramics, BSE images and reflectance IR of many samples detected an alteration layer at the surface of the samples, developed during the deposition after use. Almost all of those layers are under 100 µm thick from the surface of the ceramics.

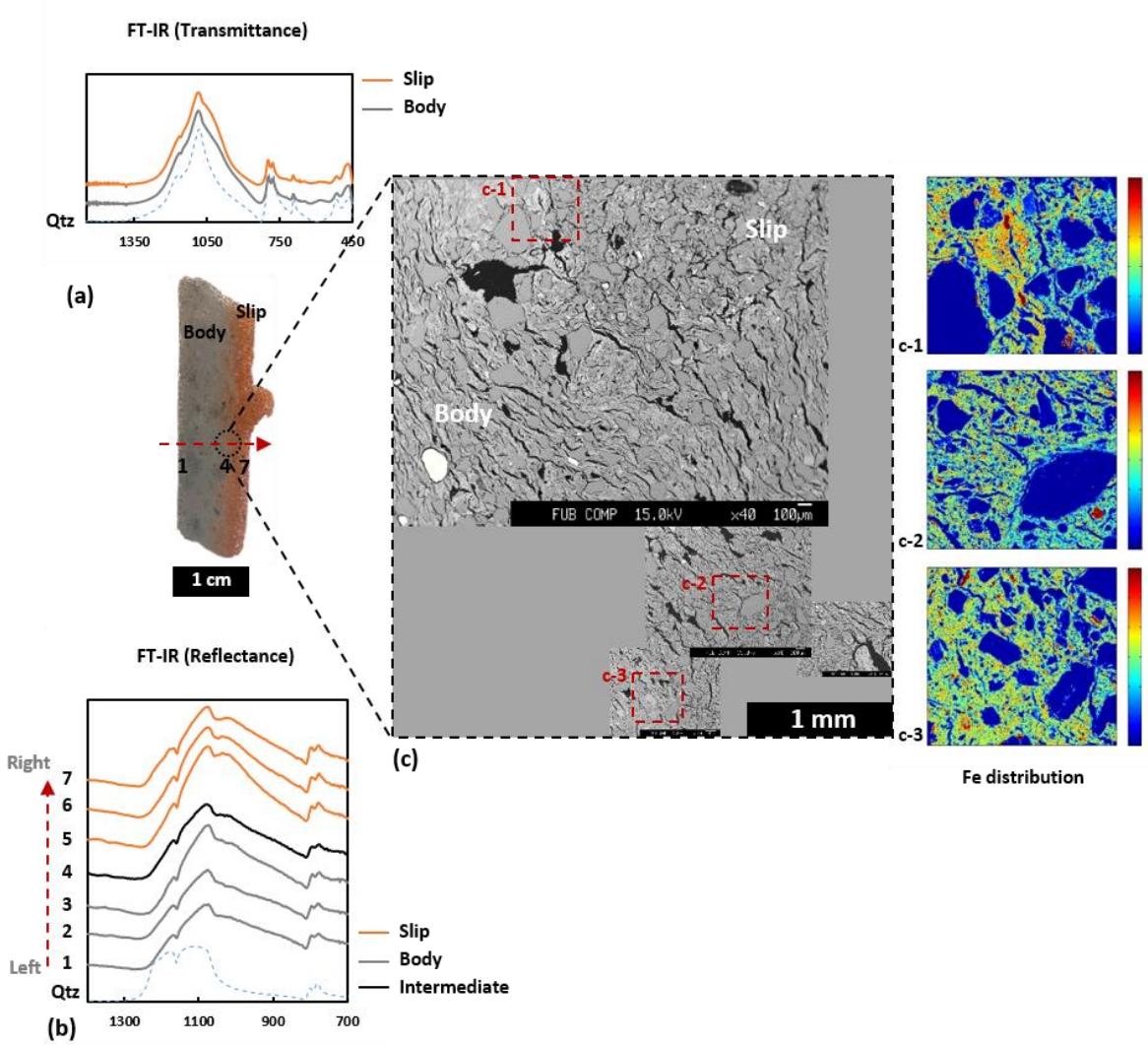

Figure 6-13. Cross section of a slip ware: (a) FTIR (transmittance) for the body and slip part; (b) FTIR (reflectance) across the cross section; (c) BSE images between the slip and body part and Fe element maps (c-1: 500µm x 500µm, c-2: 600µm x 600µm, c-3: 500µm x 500µm).

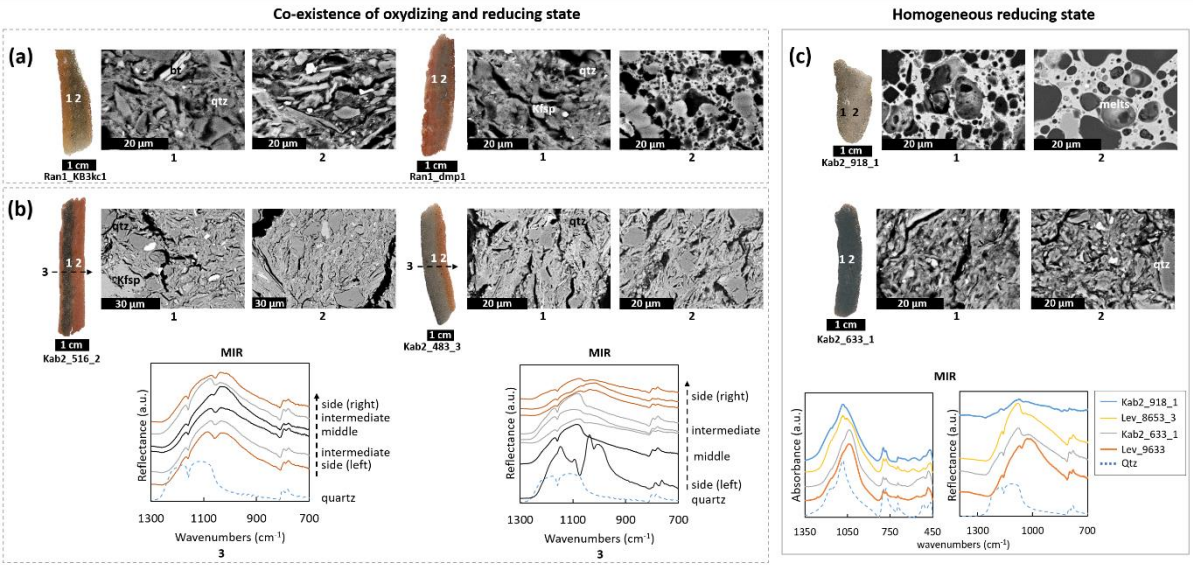

Figure 6-14. (a) Comparison of the cross section with different color profiles of Ransyrt 1 ceramics: Ran1_KB3kc1; Ran1_dmp1. BSE images for the middle/side part as indicated by the number 1 and 2. (b) Comparison of the cross section with different color profiles of the samples excavated at Kabardinka 2: Kab2_516_2; Kab2_483_3. BSE images for the middle/side part and FTIR reflectance spectra profile over the cross section taken along 3. The IR reflectance for the left side shows altered product/reconstructed clays.; (c) samples fired in the reducing atmosphere. The MIR graphs also show the spectra for quartz taken from quartz grains of the same sample for comparison. The Absorption and reflection spectra of of panel (c) for the reducing products are taken from *Park et al.* [6] (bt:biotite; qtz:quartz; Kfsp:K-feldspar).

6.4. Discussion 1: Pyrometamorphic process of the archaeological ceramics

Based on the serial employment of XRD, FTIR (transmittance and reflectance) and SEM-EDS/WDS measurements of the illite based ceramics, firing conditions of number of heterogeneous archaeological samples could be reconstructed from the macro- to microscale. First, decreasing intensity and dispersed shape of XRD peak at 2.58 Å related with octahedral cations of all the polytypes give qualitative knowledge about the dehydroxylation in the samples during ceramic firing. Peaks at (001), (002), (020)/(110) seem to lose the intensity qualitatively corresponding to the thermal transformation, although these specific structures could still remain until the total collapse of the whole structure at 950 °C. In the samples, it was difficult to find out traces of illite $2M_1$ polytype related with the geothermal environment over 300 °C. The reason would lie in the fast firing process of the ceramics. Clay layers could not have enough time to stack with a regular rotating like the $2M_1$ type, due to the rapid changes during firing. This thermal transformation during ceramic firing process influences on IR vibrations corresponding to ν_{as}(Si-O), δ(Si-O-Si) and δ(O-Si-O) in tetrahedral structure. This vibrational change becomes more visible after the beginning of illite dehydroxylation in the ceramic pastes. Water molecules derived from the reaction of two hydroxyl groups in the octahedral structure would cause clear deformation as they move out through the tetrahedral sheet and interlayer space or changes in from six to five Al-coordination in the octahedral structure influence of the structural deformation of the tetrahedral layer, too.

Before the total collapse of illite structure, the hematite peak at the (110) lattice plane appears in the decreasing illite XRD peaks as the result of oxidizing firing. Fe ions originated from illite would form hematite, because Mg and Fe substitute Al in octahedral sites or Fe replaces Si in tetrahedral sheet of

illite [30-31]. According to the crystallization environment, the XRD Bragg peaks of hematite look different from those of hematite formed in the nature which has its strong main peak at (104) reflected by Fe [32]. During ceramic firing, the peak at (110) related with oxygen atoms of the crystal appears earlier at the lower temperature than the main peak at (104). It could indicate a deficiency of iron atoms in the earlier stage of crystallization, while oxygen atoms already occupied the hematite structure, similar to the phase transformation from goethite to hematite [33-34]. It can be also assumed that the crystal shapes of hematite in the earlier synthetic stage were nanorod characterized by the strong intensity at (110) [35] which synthetic hematite shows as well [36-37]. This shape seems more likely to grow in the illite lath during illite dehydroxylation and solid state sintering stage. However, the lack of peak for (104) still indicates the Fe deficiency in the crystal and the lack of free ferric iron in the ceramic matrix. Maghemite peak at (311) which can also form through the dehydration and transformation of iron oxide/hydroxide, cannot be responsible for this peak, because no samples with less thermal deformation prove massive amounts of goethite, lepidocrocite or ferrihydrite in the ceramic paste, for which the dehydration of occurs earlier than the illite dehydroxylation. Those iron bearing minerals were observed only as individual aggregates often combined with anatase. The increasing degree of this peak doesn't fit to the other peaks of anorthite, either. The peak for (104) lattice plane appears first after illite peaks are considerably low and the peak at the hematite (110) lattice plane is clearly visible. This peak grows further during the collapse and melting of the illite structure. This tendency can indicate the filling of Fe(III) position and crystal growth. In the melts, Fe does not remain as tetrahedrally-coordinated. Rather it fills octahedrally coordinated hematite, so that it can precipitate. Morphologically, the open elongated pores in the matrix gradually decrease and illite begins solid state sintering forming the clay lath. The closed pores become gradually surrounded and filled with the melts, after illite begins the liquid phase sintering between 900 and 950 °C in general [38]. These new pores have a globular shape due to interfacial tension effects [39]. Spinel would be crystallized before the total collapse of illite under 950 °C, as Mcconvill and Lee (2005) proved with their topotactical crystallization in the clay lath with TEM [40]. However, this mineral grows massively in the melt during the liquid phase sintering, as the XRD peaks at (113) and (004) proved. These peaks appear in the slightly different 2θ ° according to the samples indicating different unit cell parameters of this mineral in each ceramic sample. This thermally induced crystallization could occur similarly in the biotite-chlorite intergrowth as well [16]. In the Al-Si-Fe-Mg system of the melt, the chemistry for the nano-sized spinel crystals would be Si-Al spinel ($2Al_2O_3 \cdot 3SiO_2$), Mg-Al spinel ($MgAl_2O_4$) or Mg-Fe-Al spinel ($(Mg,Fe)Al_2O_4$). In comparison to the spinel crystallization, mullite, one of the common high firing mineral was not detected in any samples containing the liquid phase sintering, although this mineral can start to crystallize in the melt at 1100-1150 °C [41]. The absence of this mineral means that the peak firing temperature of the ceramics was under 1100-1150 °C, because the massive development of mullite occurs at 1300 °C. Alternatively, the firing time might be too short for enough Al released for the mullite formation. The very porous structure in a micrometer scale of the most samples in this study is related with that non-densifying

mechanisms such as surface diffusion, lattice diffusion from the surface or vapor transport were stronger in this scale [42]. However, it is still unknown whether a densifying mechanism dominates the formation of illite laths in a nanometer scale, because shrinkage in the lath structure could cause porous fabrics for a micrometer scale.

In the Ca-rich ceramic paste, the pyrometamorphic process exhibits similarities to that of the Ca-poor matrix. At all the studied sites, Ca^{2+} ions were supplied from calcite, except of only one sample from Ransyrt 1 containing relatively high Mg contents which remind us of dolomite as the main bedrock building mineral of this site. According to the increasing firing temperature, hematite crystals grow and gehlenite is formed at the grain boundary of decomposing calcites. Because hematite can be developed in the high Fe_2O_{3tot}/CaO ratio, such as 0.7, the crystallization of hematite can prove the oxidizing firing of the Ca-rich ceramics [16]. In many cases, calcite and gehlenite, hematite and spinel (Mg-Al or Al-Si) coexist over 1050 °C, due to the heterogeneous mixed state of the ceramic pastes and huge grain size of calcite in the most ceramic pastes. If the local matrix in the paste has less Al and more Ca and Si, wollastonite is developed in a needle-like crystal shape, instead of gehlenite.

In the reducing atmosphere, lower $f(O_2)$, 1/T (absolute temperature) and Al/(Al+Si) stimulate the transformation of Fe into Fe(III) [43]. However, it is not crystallized as ferrous iron bearing minerals, but contributes to the earlier vitreous phases of the ceramic matrix cutting Si-O bonds like network-modifier in glass forming process [43-46]. Preexisting accessory phase composed of Fe/Ti oxides and hydroxides in the ceramic pastes, such as goethite would be transformed into magnetite, ilmenite or hercynite [47], although these minor phases were not visible by XRD or FTIR measuring the ceramic mixed powder.

Concerning on the whole observations in the ceramic sherds, the pyrometamorphic process in the illite based ceramics between 300 and 1200/1300 °C is summarized in figure 6-15. Following reactions are describing representative phases during the firing process in the oxidizing atmosphere:

1) Ca-poor matrix in oxidizing atmosphere

$$\underset{\text{illite}}{(K,H_3O)(Al,Mg,Fe)_2(Si,Al)_4O_{10}[(OH)_2,(H_2O)]} \longrightarrow \underset{\text{hematite}}{Fe_2O_3} + \underset{\text{spinel}}{(Mg,Fe)Al_2O_4} \text{ or } \underset{\text{amorphous}}{2Al_2O_3{\cdot}3SiO_2 + SiO_2 + \alpha} \quad (6\text{-}4)$$

2) Ca-rich matrix in oxidizing atmosphere

$$\underset{\text{illite}}{(K,H_3O)(Al,Mg,Fe)_2(Si,Al)_4O_{10}[(OH)_2,(H_2O)]} + \underset{\text{calcite}}{CaCO_3} \longrightarrow$$

$$\underset{\text{gehlenite}}{Ca_2Al(AlSi)O_7} + \underset{\text{hematite}}{Fe_2O_3} + \underset{\text{spinel}}{(Mg,Fe)Al_2O_4} \text{ or } \underset{\text{amorphous}}{2Al_2O_3{\cdot}3SiO_2 + SiO_2 + \alpha} \quad (6\text{-}5)$$

As minor phase, mullite in Ca-poor matrix and wollastonite in Ca-rich matrix could be present. In the reducing atmosphere, only spinel and amorphous silica were confirmed as main phase in the melts.

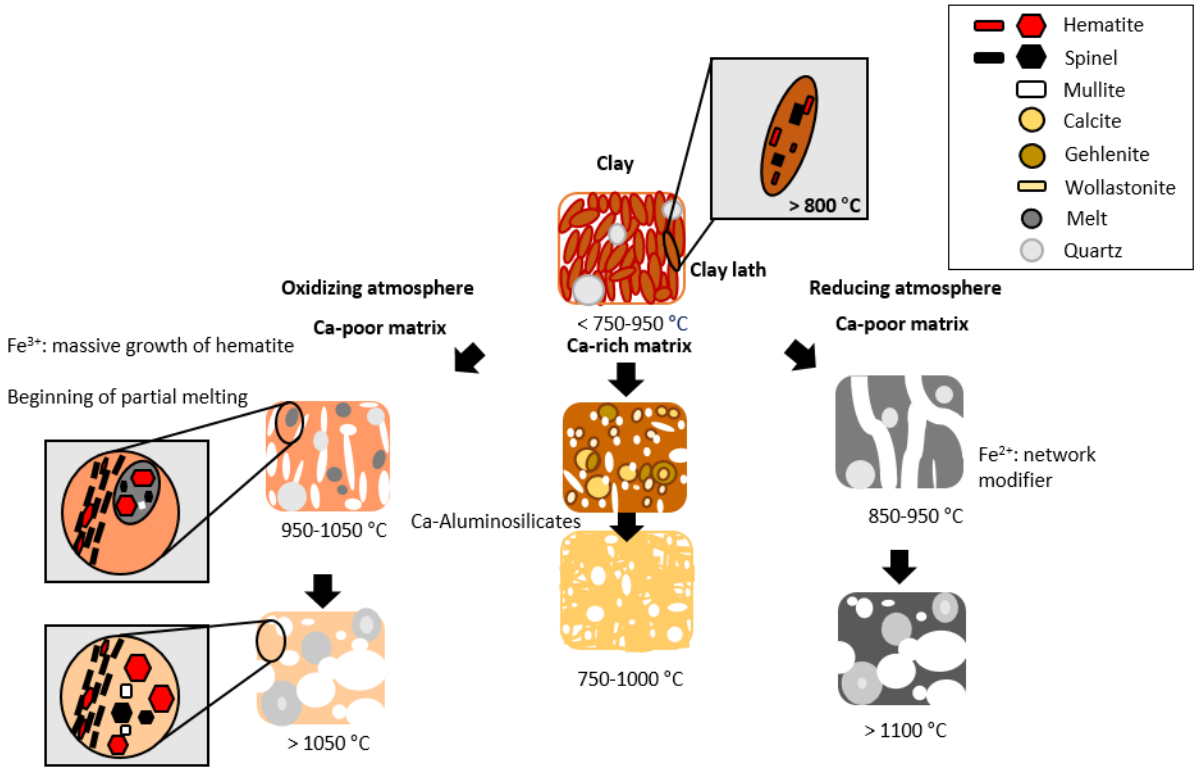

Figure 6-15. Morphological changes and new crystallization of ceramic materials under various firing conditions.

The defects in the dioctahedral layer of the 2:1 phyllosilicate occur, if the octahedral ions delivering the plus valence charge of 2 such as Mg^{2+} or Fe^{2+} replace the trivalent ions such as Al^{3+} or Fe^{3+} [48-50]. The ratio between the ferric and ferrous ions in the ceramic paste composed of such clay minerals changes according to the degree of oxygen partial pressure during firing. As consequence, the layer charge deficiency or surplus by the change of the valence charge of Fe will cause the distortion of the octahedral layer and dehydroxylation, which leads to the earlier total collapse of the clay structure [51-52]. If the conversion of preexisting Fe^{3+} to Fe^{2+} in the octahedral layer is dominant, it will lower the energy barrier for the dehydroxylation [52-53]. Furthermore, the free Fe^{2+} cuts the Si-O like network-modifier in glass forming process and contributes to the early vitreous phase as well, while Fe^{3+} migrated from dehydroxylated illite recrystallizes as hematite and aluminosilicates fill pores forming partial melts [54-56]. Based on the observations in the cross section of the highly fired ceramics with gray middle part influenced by the lower oxygen partial pressure and reddish part at both sides due to the presence of the higher oxygen amount, the localized redox state can contribute to the distribution of the different dehydroxylation degree of illite within a ceramic object. According to the simulation results, this difference is caused mainly by the volume ablation regime of the oxygen diffusion determined by the reaction rates between oxygen and reactants in the diffusing media [51]. In archaeological ceramics, the oxygen diffusion will be influenced by carbon-oxygen-iron reactions with the possible participation of water. The chemical and mineralogical composition of the samples excavated at both archaeological sites confirm that C- and Fe- bearing phases were rich in the ceramic pastes [6]. The grain size distribution of the ceramics indicated that the resource was gathered from the sediments containing considerable amounts of such reactants as well [57]. Therefore, the oxygen diffusion occurred as a rate

limiting step and left optically distinguishable different color profiles in the cross section. The ceramics found at Kabardinka 2 are more Fe rich and show more reddish colors in both sides, while the samples excavated at Ransyrt 1 have sometimes light brown or reddish brown sides because of the relative higher amounts of Ca-carbonates in the ceramics. If the degree of the volume ablation regime is not significant in the oxygen diffusion, other parameters such as open porosity, increasing rate of the firing temperature and sample thickness in the relatively short firing time will decide the general pattern of the diffusion. The ceramics from Ransyrt 1 with the bigger open porosity will have more homogeneous oxygen partial pressures than those from Kabardinka 2 containing less open pores due to the smaller grain size distribution [58]. In case of the Ca rich samples, it is possible that the diffusion pattern is difficult to estimate because of the grain size effect of calcite and the interdiffusion between Ca in calcite and Fe and Mg in the ceramic matrix during the dissociation of the carbonates. The heat transfer rate in the ceramics with the thickness between 0.5 and 1.5 mm is so fast, that the firing temperature and anisotropy factor by the orientation of the various porous components decide the temperature profile across the ceramic wall. If the sand grains are aligned randomly, ceramic matrix becomes highly connected according to the decreasing porosity, the thermal conductivity of porous ceramics will be relatively homogeneous with a small difference of temperatures within the sample and this will play a minor role in the local ferric and ferrous ion ratio distribution pattern.

6.5. Estimation of the firing conditions

6.5.1. Average firing temperature

The dehydroxylation temperature for illite polytypes are 600 °C for *tv*-1M [59], 750 °C for *cv*-1M [59] and 525 °C for $2M_1$ Illite [60]. Other mineralogical transformations and crystallizations in the ceramics often accompany this thermal transformation of illite, too: transformation of goethite into hematite at 250-300 °C; thermal decomposition of Ca-carbonate at 650-700 °C; massive growth of hematite and spinel at 750 °C and 950-1050 °C; mullite crystallization at 1125 °C and its massive development at 1300 °C [61-63]. Additionally, morphological changes in a micrometer scale are clearly visible after the solid and liquid phase sintering of illite over 950 °C [30]. After solid state sintering, all grains are in contact to other grains and build a three-dimensional network with interconnected pores of irregular shape in the matrix. At 1300 °C, it is degraded to a totally vitreous phase [64]. The changes in ν_{as}(Si-O) and δ (Si-O) by FTIR provided supplement data for the classification of the firing degrees. Figure 6-16 describes the distribution of average firing temperature depicted for each sample. The thicker red error bar for several samples indicates the spread of temperature detected within a cross section. In this estimation, ceramics from Kabardinka 2 were fired in more various temperatures in comparison to the other archaeological sites. Well controlled reducing firing could be detected at Kabardinka 2 and Levinsadovka. In the meanwhile, presence of calcite and its transformation to Ca-aluminosilicates as consequence in Ransyrt 1 ceramics, it is often difficult to confirm whether the potters pursued controlled

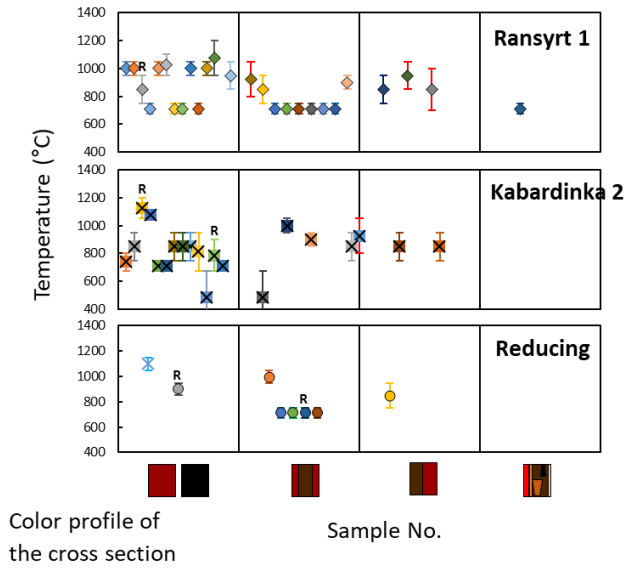

reducing atmosphere. The ceramics from all the sites were not fully vitrified indicating the firing temperature below 1200-1300 °C.

Figure 6-16. Average temperature of representative ceramic sherds according to the color profile of the cross section: (a) Ransyrt 1; (b) Kabardinka 2; (c) Levinsadovka-Saf'janovo (R: controlled reducing firing).

6.5.2. Kinetics of the dehydroxylation in the illite based ceramics

Dehydroxylation kinetics of clay minerals such as illite, one of the most abundant clay in the sediments were studied by heating experiments combined with XRD measurements [65]. A conversion factor, α accounting for the degree of the dehydroxylation was taken from the integrated area of the specific peaks, (001) and (020) was normalized by the peak area of the initial state,

$$\alpha = (A_{measurement} - A_0)/A_0 \,, \tag{6-6}$$

where $A_{measurement}$ and A_0 are the integrated area of the measured sample, after and before the beginning of the dehydroxylation, accordingly. In this study, the integrated area below the XRD peaks of the samples was normalized by that of the sample with the least dehydroxylation,

$$\alpha = (A_{measurement} - A_{min})/A_{min} \,, \tag{6-7}$$

where A_{min} is an integrated area of the sample with the least firing degree. This conversion ratio by XRD measurements was compared to that by the band shifts in the FTIR measurements (absorbance/MIR).

$$\alpha = (\nu_{as,\ measurement}\ (Si\text{-}O) - \nu_{as,\ clay}\ (Si\text{-}O))/(\nu_{quartz}\ (Si\text{-}O) - \nu_{as,\ clay}\ (Si\text{-}O)) \,, \tag{6-8}$$

$$\alpha = (\delta_{measurement}\ (Si\text{-}O) - \delta_{clay}\ (Si\text{-}O))/(\delta_{quartz}\ (Si\text{-}O) - \delta_{clay}\ (Si\text{-}O)) \,, \tag{6-9}$$

where $\nu_{as,\ clay}$ (Si-O) and ν_{quartz} (Si-O) are asymmetric vibration of Si-O bonding in the clay mineral and quartz, respectively.

For the isothermal environment, Arrhenius law is efficient to derive the reaction rate constant k,

$$k = A\exp[\frac{-Ea}{RT}] \,, \tag{6-10}$$

where the Arrhenius parameters E_a and A are apparent activation energy and the frequency factor, accordingly. The calculated conversion factor, α and the reaction constant are combined with one of the kinetic equations, the Avrami-Erofe'ev equation, $g(\alpha)$ which is effective in heterogeneous solid solutions [66] and the firing time can be derived,

$$g(\alpha) = k(t_{total} - t_{min}) = [-\ln(1-\alpha)]^{1/n} \,, \tag{6-11}$$

$$(t_{total} - t_{min}) = [-\ln(1-\alpha)]^{1/n}] \,/\, [A\exp[\frac{-Ea}{RT}]] \,, \tag{6-12}$$

where t_{total} accounts for the total firing time, t_{min} for the time needed to reach the lowest dehydroxylation degree of the measured samples including the induction time, R is the gas constant (R = 8.314 J/mol·K) and T the firing temperature (K) after t_{min} and T_{min}, respectively. The Avrami coefficient, n is estimated between 0.5 and 1 according to the rate limiting steps in the dehydroxylation of clays which vary according to the temperature.

During heating with the constant rate, the reaction rate constant can be taken as the integral form according to the time or temperature [67].

$$g(\alpha) = [-\ln(1-\alpha)]^{1/n} = \int_0^t kt\,dt = \int_0^T A\exp\left[\frac{-Ea}{RT}\right]dT\,, \qquad (6\text{-}13)$$

where n is the Avrami coefficient.

Concerning the relatively clear and reproducible changes according to the firing degree, the dehydroxylation degree of illite was calculated using the conversion factor acquired from XRD results of this project [6]. The shifts of the MIR band assigned to ν_{as} (Si-O) between 1030 and 1080 cm^{-1} and δ (Si-O) between 450 and 500 cm^{-1} presented in this project are comparable to the XRD results as well (Figure 6-17). The integrated area of XRD peaks at (001) and (110/020) of the samples was normalized to that of the sample with the least degree of dehydroxylation, because the changes in (001) peak area represent the collapse of the interlayer basal spacing of illite and those of (110/020) are related to the octahedral structure of the clay mineral (Figure 6-18). For modeling the conversion based on the band shifts of ν_{as} (Si-O), $\nu_{as,\ illite}$ (Si-O) was set as 1030 cm^{-1} and $\nu_{\ quartz}$ (Si-O) as 1080 cm^{-1} as reference. The increasing tendency of the conversion from the low to the high firing products appear in both XRD and FTIR based conversions. Each conversion factor indicates slightly different increasing degrees, because anisotropic vibrational changes in Si-O bonds in the tetrahedral layer occur in the different order and degree, in comparison to the rate of destructuralization of K in the interlayer.

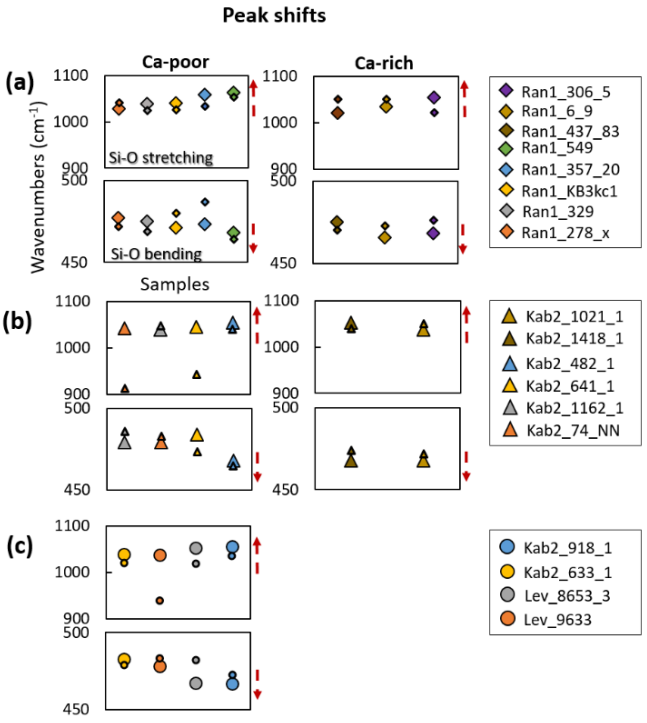

Figure 6-17. Comparison of the MIR absorbance band shifts of ν_{as} (Si-O) between 1030 and 1080 cm^{-1} and δ (Si-O) between 450 and 500 cm^{-1}. Major and minor band with bigger and smaller shape, respectively. Acquired from (a) the ceramics excavated at Ransyrt 1: Ca-poor; Ca-rich; (b) the ceramics found at Kabardinka 2: Ca-poor; Ca-rich; (c) the ceramics fired in the reducing atmosphere.

For the general approximation of the firing time and temperature both for the isothermal and non-isothermal firing processes, the conversion factor taken from the integrated area of XRD peak at (001) and (110/020) was used, because the diffraction changes in the interlayer and at (110/020) take place gradually like thermal decomposition of illite which occurs layer by layer without the formation of

intermediate phase [60,68-69]. Under isothermal conditions, the estimated firing temperatures of the samples from the combination of XRD, FTIR (MIR) and SEM were applied to the Arrhenius equation [6] and firing time was taken from the Avrami-Erofe'ev formula. For the non-isothermal ceramic firing, firing time and temperature were derived based on the conversion factor. The Avrami coefficient, *n*, 0.5 and 1 were employed separately for the calculation, in order to estimate the general ranges of the firing time and temperature of the heterogeneous composite materials. The reaction rate constant, *k* calculated by the Arrhenius equation was clearly different for both conditions (Figure 6-19). In general, the value of the rate constant in both firing conditions increased according to the increasing temperature. The increase of *k* in the isothermal run is much bigger and faster than that in the non-isothermal run.

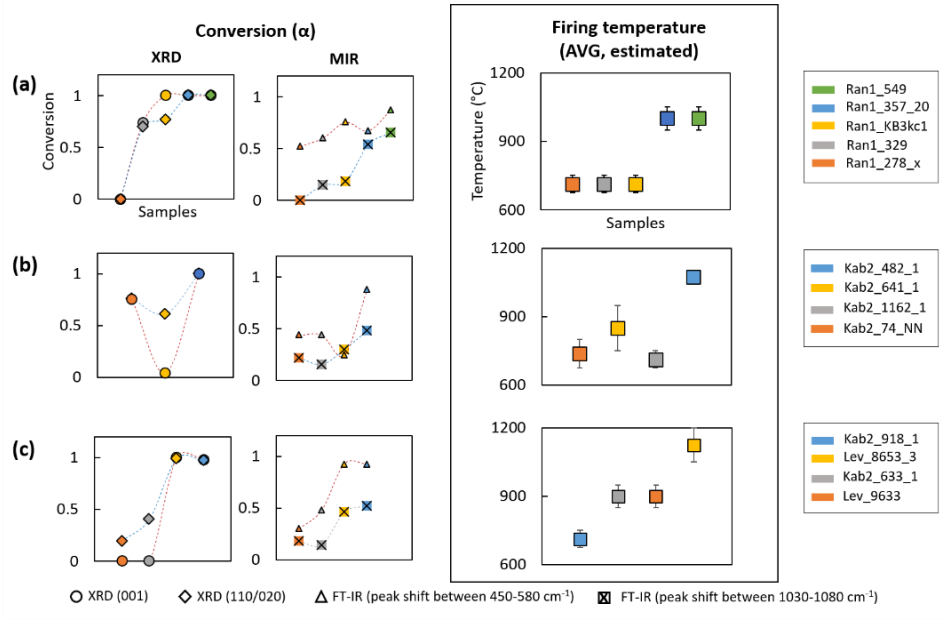

Figure 6-18. Conversion factor, α acquired from XRD peak at (001), (110/020) and α based on the MIR major band shifts of ν_{as} (Si-O) and δ (Si-O) between 1030-1080 and 450-580 cm^{-1}, accordingly. Comparison to the estimated average firing temperatures of the same samples [6]. Samples from (a) Ransyrt 1; (b) Kabardinka 2; (c) samples produced by the reduced firing.

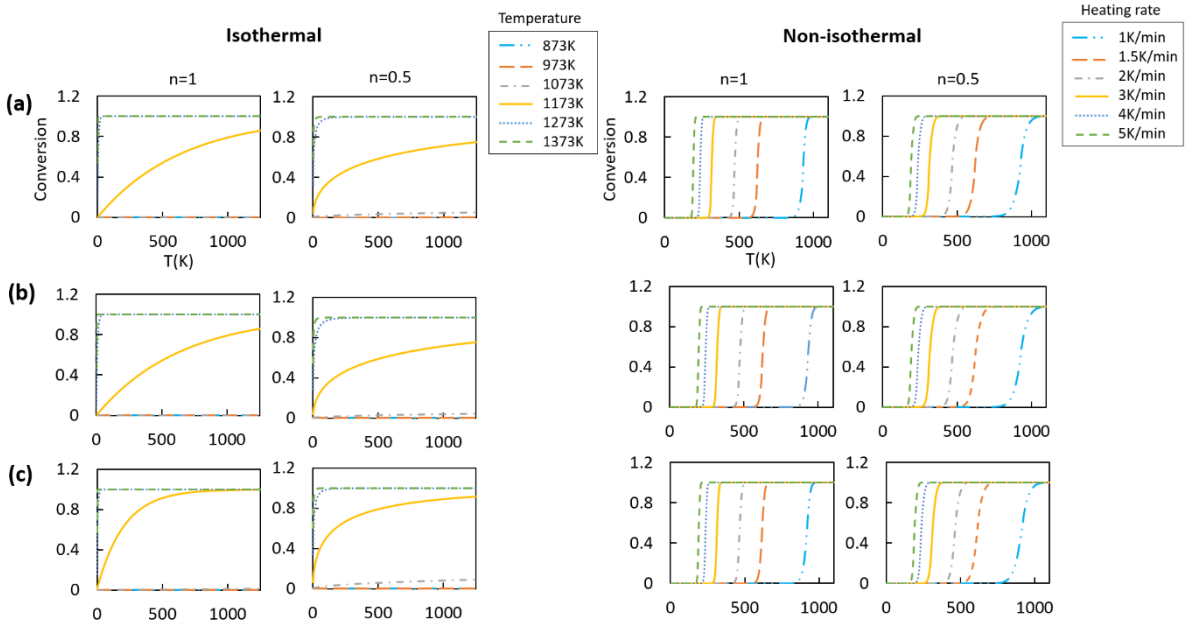

Figure 6-19. Reaction rate constant *k* according to the Avrami coefficient n=0.5 and n=1. Comparison between *k* calculated with the estimated average firing temperature for the isothermal run and *k* calculated with various constant heating rates for the selected ceramics excavated at (a) Ransyrt 1; (b) Kabardinka 2; (c) ceramics fired in the reducing atmospheric condition.

This tendency influenced the results of the required firing time and temperature for the conversion in the fired ceramics. During isothermal conditions, the firing time and its range was mainly determined by the conversion factor of each sample (Figure 6-20). The low and middle firing products require mostly long firing time of more than 10 hours to a few days, while the time range for the ceramics with the higher conversion ratio is drastically reduced to less than one hour.

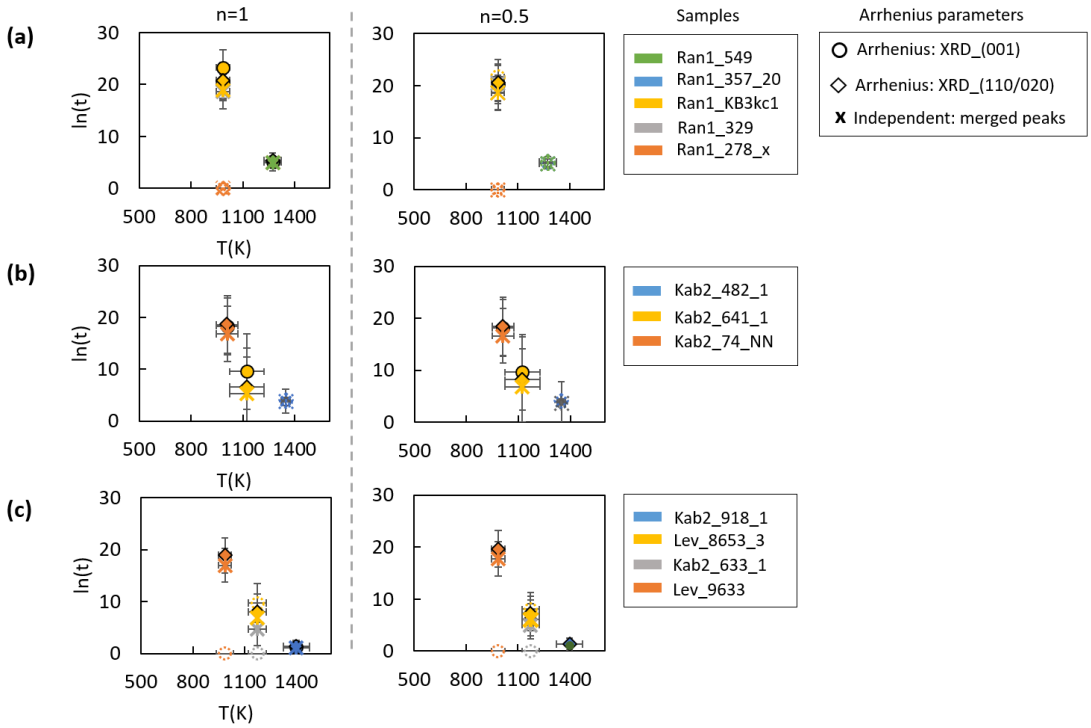

Figure 6-20. Firing time (min)-temperature (K) relation in the form of ln (time)–T(K) in the isothermal conditions calculated by the Avrami-Errofe'ev based on XRD peak at (001), (110/020) for the selected samples excavated at (a) Ransyrt 1; (b) Kabardinka 2; (c) ceramics fired in the reducing atmosphere.

In the non-isothermal runs with the constant increasing heating rate, the gap between the firing time of various temperatures is relatively smaller than that in the isothermal conditions for both Avrami coefficients (Figure 6-21). If the Avrami coefficient and the heating rate were 1 and 1K/min as slow process, 8-9 hours were required for the lowest firing degree and 16-17 hours for the highest firing degree at both archaeological sites. If the heating rate was 5K/min with the Avrami coefficient of 1, the firing step for all the products with the different firing degrees could be finished within 4-5 hours. In comparison to the objects from Ransyrt 1, the conversion factor, α of some ceramics excavated at Kabardinka 2 could not be calculated from the XRD measurements, due to the higher interruption of mica (Figure 6-21.b) [6]. In such case, it is expected that band shifts in MIR can provide alternative conversion factor for the kinetic calculation. The lower Avrami coefficient such as 0.5 in this study caused the bigger range of the firing time and temperature between the ceramics with different conversion ratios.

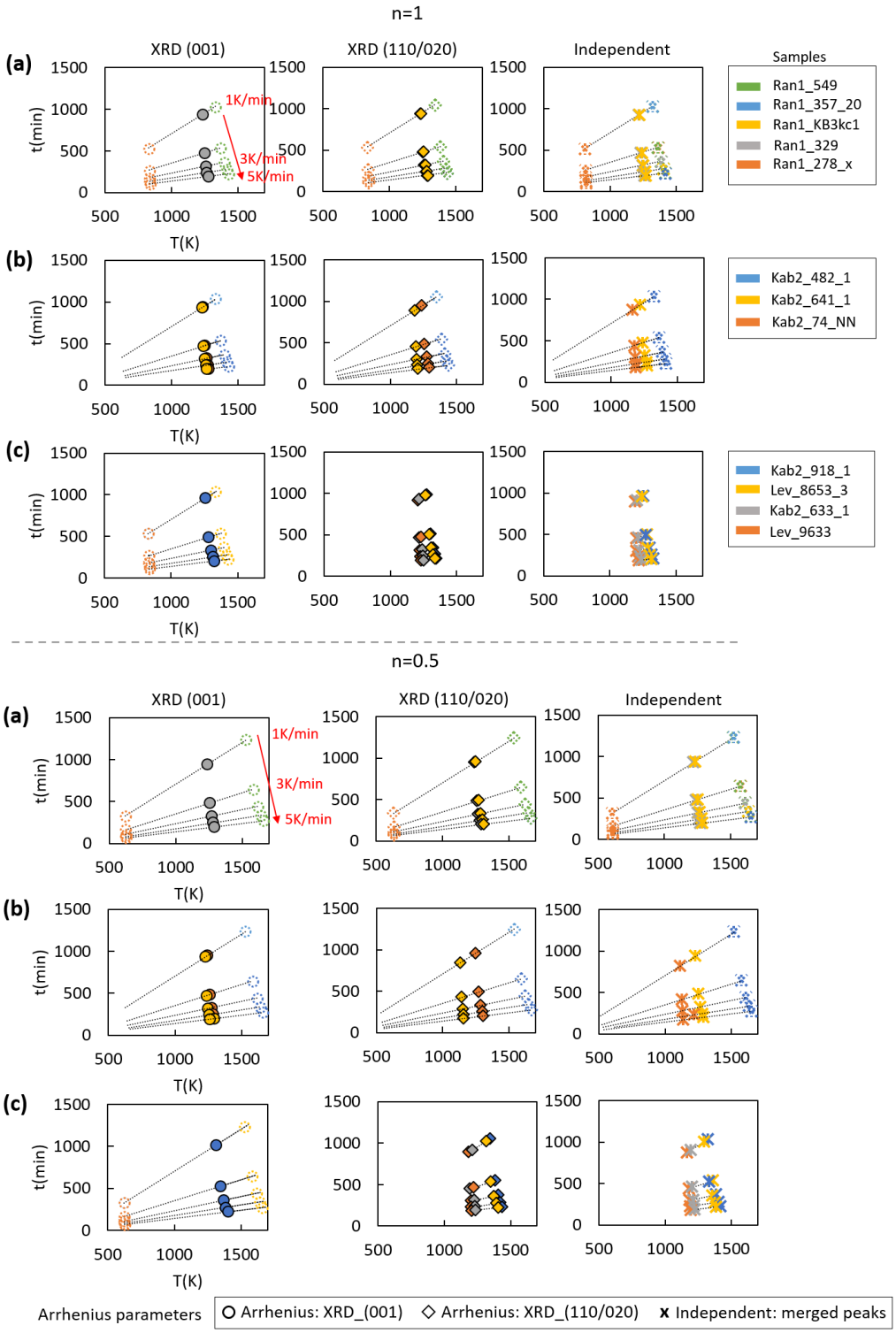

Figure 6-21. Firing time-temperature relations in the non-isothermal conditions calculated by the Avrami-Errofe'ev based on XRD peak at (001), (110/020) for the selected samples from (a) Ransyrt 1; (b) Kabardinka 2; (c) ceramics fired in the reducing atmosphere.

6.5.3. Heat transfer within the archaeological ceramic

The one-dimensional unsteady state conduction is described by Fourier's second law of heat conduction,

$$\frac{\partial T}{\partial t} = \alpha \frac{\partial^2 T}{\partial x^2}, \tag{6-14}$$

where T and t, x and α are firing temperature and time, 1-D distance and thermal diffusivity, respectively. The thermal diffusivity is given as the ratio,

$$\alpha = \frac{\lambda}{\rho c_p}, \tag{6-15}$$

thereby λ represent thermal conductivity, ρ density and c_p is specific heat capacity. The thermal conductivity of porous ceramics is calculated by the following model [70-72],

$$\lambda_{eff} = \lambda_s(1-\Pi)^{3/2} + \lambda_\Pi \Pi^{1/4}, \tag{6-16}$$

where λ_s and λ_Π are thermal conductivity contributions of solid phase and pore phase, accordingly and Π stand for the porosity. This model is valid for the whole range of porosity. The heat-barrier resistances M, is introduced to this model,

$$\lambda_{eff}=\lambda_s M(1-\Pi)^{3/2} + \lambda_\Pi \Pi^{1/4}, \tag{6-17}$$

$$M=M_{macr}M_{micr}, \tag{6-18}$$

where M_{macr} is the influence of macroscracks in the structures between 10^3-10^4 µm and M_{micr} accounts for the microcracks covering 10-10^2 µm. In this study, the one-dimensional (1-D) partial differential equation is solved by MATLAB (2018b) simulation using implicit finite difference methods (FDM) in 1-D.

The heat transfer was simulated by implicit FDM solving the partial differential equation for the heat conduction of porous ceramics in a 1-D transect over the sample. In order to calculate the thermal diffusivity of porous ceramics, thermal diffusivity of pores was taken from the thermal conductivity of air [73]. The solid phase is composed of the two representative mineral phases of the samples, illite and quartz. Thus, thermal diffusivity of quartz depending on the temperature [74] was combined with that of illite [75] or derived from the combination of the thermal conductivity [76-79], specific heat capacity [80-81] and density [82-87]. These physical properties vary according to temperature, approximated by the least square regression. The thermal conductivity of illite as raw clay mineral was set between 0.3 and 1.5 (W/m·K) as the constant variable, because it is different from each other depending on the geological context and the range of its change according to the temperature is relatively very small [81]. Another important variable, porosity of the ceramics was taken from the literature data [88-90]. Based on the negative linear relationship between the porosity and temperature, the changing porosity was approximated continuously to the temperature increase [89]. The heat contact resistance or heat barrier resistance of the thermal conductivity was changed mainly by the influence of the microcracks ranging from 10 to 100 µm, determined by the effective contact area in this study [91-92]. Boundary conditions describing the input temperature were set as same with the firing temperature which influence from both sides of the cross section. All these parameters were dependent on the local temperature for the simulation unit in the cross section, except of the anisotropy caused by the local geometries such as the direction of the grains or pores. In the homogeneous ceramic pastes, this anisotropy of the structural elements which influence the direction of the heat transfer can be defined as temperature dependent as well, because highly networked pore complex turns into the parallel to the pottery wall with elongated shapes losing the pore volumes and becomes globular closed pores gradually filled by melts in the sintering stage [88,93-96]. However, the huge grain size distribution in the most samples and the presence of water in the ceramic pastes, the direction of the sand grains composed of poly-mineral phases

and corresponding porosity were not easily estimated as the simple relation between the temperature, formation and anisotropy factor [90,97]. Depending on the orientation to the direction of the heat transfer to any structural elements in the composite materials, this factor closes to 1 [48,98-99]. In this study, it is randomly set between 0.001 and 1.

Regarding the simulation results, the heat transfer profile was very even over the cross section. In the time range of the minute, the temperatures in the middle and at both surfaces reach to the same level very fast, despite the various input values for the mineralogical composition of the grains or ratios between sand grains and clay minerals, thermal diffusivity of each phase or porosity. The changes in the thermal diffusivity of illite do not influence the distribution of temperature within a sample over the heating temperature range. Instead, the uneven boundary conditions with the different heating rate from the both sides, thickness of the samples and the randomly set anisotropy factor caused distinguishable changes within the calculated area (Figure 6-22). Especially, if the anisotropy factor decreases, the heat transfer rate becomes lower (Figure 6-22.a). In the thicker cross section with the longer firing time, the temperature difference was ca. 20-60 K depending on the anisotropic factor.

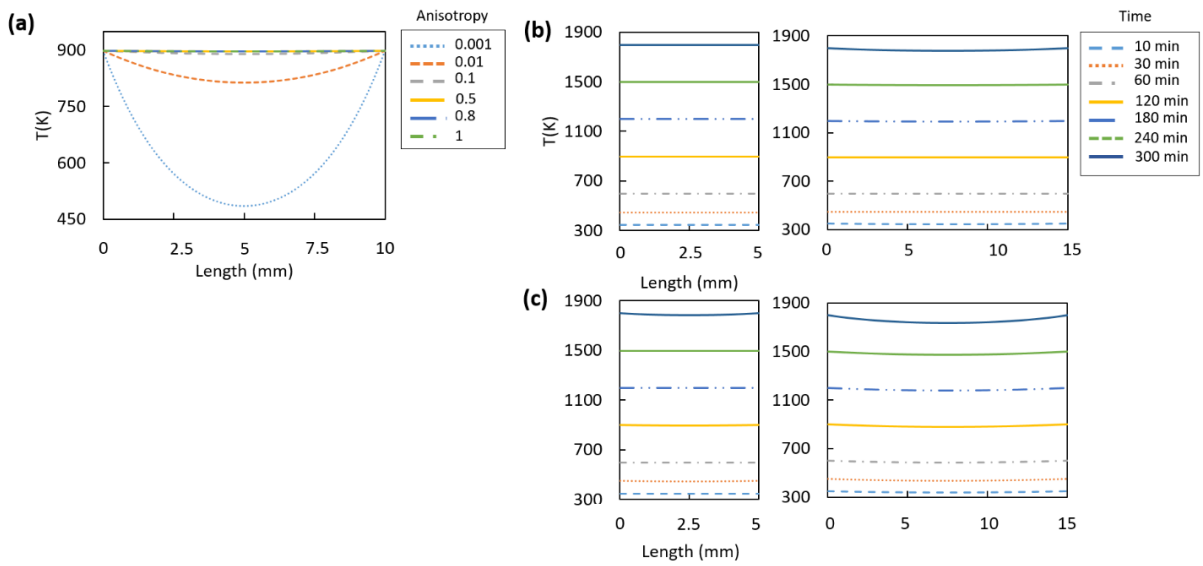

Figure 6-22. Temperature profile in the cross section by FDM of the heat conduction equation. Open porosity from [90]. Thermal diffusivity of illite=1. Heat flow from both boundaries with the constant heating rate=5K/min. quartz:illite=1:1.: (a) Comparison of the profile with various anisotropy factors. The unit length= 0.1mm for the total thickness of 10mm. Firing time of 120min.; (b) Comparison of the profile with various firing times and thickness. The unit length= 0.1mm. Anisotropy factor=0.5.; (c) Comparison of the profile with various firing times and thickness. The unit length= 0.1mm. Anisotropy factor=0.1.

6.5.4. Oxygen diffusion and corresponding redox states

Fick's second law describes the unsteady state molecular diffusion as the dominant diffusion regime in the µm scale [100].

$$\frac{\partial c_A}{\partial t} = D_{AB} \frac{\partial^2 c_A}{\partial z^2}, \tag{6-19}$$

where z and c_A are distance, concentration of A, respectively. D_{AB} is a gas diffusion coefficient of A into B (cm^2/s) depending on the pressure under which the diffusion coefficients were measured. A pressure independent diffusion coefficient for gas is suggested by *Fuller et al.* [101-102],

$$D_{A,B} = \frac{1.0868 \times T^{1.75}}{\sqrt{m_{AB}}(\sqrt[3]{V_A}+\sqrt[3]{V_B})^2}\,, \tag{6-20}$$

where D_{AB} is the diffusion coefficient of A in B (Torr cm^2/s) at the Temperature (K). m_{AB} is given by

$$m_{AB} = \frac{2}{(\frac{1}{m_A}+\frac{1}{m_B})}\,, \tag{6-21}$$

where m_A and m_B are the molecular weights (g/mol) of A and B, V_A and V_B are the dimensionless diffusion volumes of A and B, respectively. The diffusion volume of air is 19.7 and that of O_2 is 16.3 [103]. In porous media, the diffusion coefficient is influenced by the porosity and corresponding tortuosity as well [104-106]. The effective diffusion coefficient in this case is given as [81],

$$D_{eff} = \frac{\varepsilon}{\eta} D_{AB}\,, \tag{6-22}$$

where ε is porosity, η is tortuosity. Tortuosity can be taken from the porosity-tortuosity relation which describes a system of non monosized spheres, $\varepsilon^{-1/2}$ [91-92]. The reactivity of oxygen in the ceramic materials determines the surface ablation or volume ablation as the dominant regime of the diffusion. The Thiele number, Φ indicates the dominant diffusion regime which is proportional to the following [81],

$$\Phi \propto \frac{k_{CO,CO_2}}{D_{AB}}\,, \tag{6-23}$$

where k_{CO,CO_2} is reaction constant for CO and CO_2. In this study, the partial differential equation describing oxygen diffusion process in the firing composite materials is solved by MATLAB (2018b) using implicit 1-D FDM, in order to find out how this phenomenon contributes to the dehydroxylation process of the clay mineral and corresponding features of the archaeological ceramics.

The oxygen diffusion rate through the ceramic cross section was performed for the non-isothermal environment with the constant heating rate following the general estimation of the kinetics of illite dehydroxylation. It was simulated by the implicit FDM solving the partial differential equation of the Fick's second law, because the average diameter of the observed open porosity in the ceramic samples, was bigger than 1-2 µm [90], is employed as dominant regime [109]. Besides of the measured open porosity of the ceramics, literature data were taken into consideration for the calculation [89-90]. The porosity and corresponding tortuosity were set as changing parameter, according to the increasing temperature. The boundary conditions were constant as 0.21 atm in the air for both sides of the cross section. The samples identified as the pottery wall are relatively thin ranging between 0.5 and 1.5 cm for Ransyrt 1 and between 0.4-1.0 cm for Kabardinka 2. Thus, the 1-D distance for the simulation was 0.5, 1, 1.5 cm for each calculation. Because of the complex changes of the reactivity of oxygen to C-, Fe and possibly S-bearing phases and H_2O in the heterogeneous ceramic pastes during firing, the Thiele number is very sensitive to the firing conditions, so that this number cannot be easily set for the real ceramic firing [108-111]. For the general overview in this study, it was determined as various values between 0.0001-1, with regard to the kinetic reaction constant k for the carbon-oxygen reaction which has two velocity constants, k_a, adsorption coefficient with the value 0.14 g/cm^2 s and k_d, desorption coefficient with 2617 g/cm^{2}s [112]. Between 636 and 838 °C, a mean value of these coefficients was

employed. In this simulation, the final diffusion coefficients were obtained by the multiplication of the effective diffusion coefficient and the Thiele number, in order to observe the influence of the reactivity between oxygen and the ceramic pastes during firing directly.

The simulation results indicate that the oxygen concentration gradient which influences the color profile of the ceramic thin sections, was determined mainly by the Thiele number representing the reactivity of the oxygen by diffusion to the reactant in the ceramic pastes and firing time as an additional factor for the thickness of 5 mm cross section (Figure 6-23). If the ceramic thickness is 15 mm, the distribution of the oxygen partial pressure becomes more uneven and very little oxygen is diffused into the open pores in the 1/3 of the whole ceramic body in the middle part. The pore shapes and their changes according to the increasing firing temperature did not play a crucial role after 30-60 minutes of firing, regardless of the initial porosity and ratio of the composite materials.

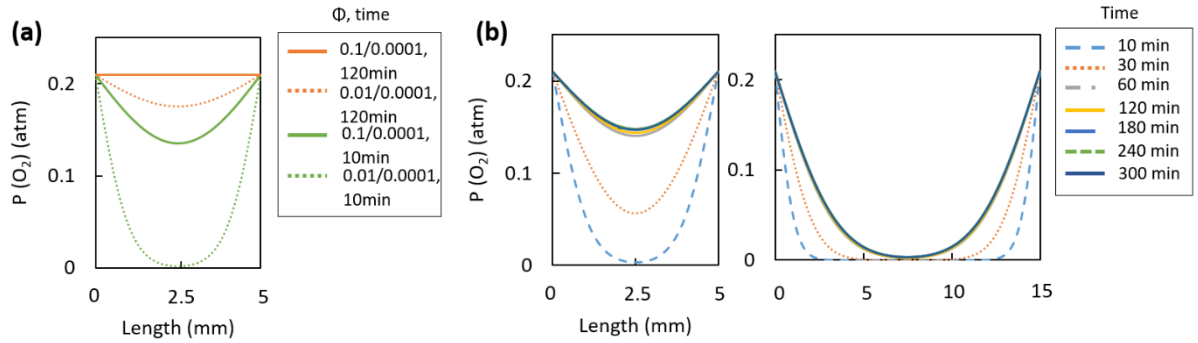

Figure 6-23. (a) Oxygen diffusion rate profile according to the cross section. By FDM for 1-D Fick's second law for the open pores [90] and 5 mm-thickness. Comparison of the oxygen partial pressure by the different Thiele numbers (Φ up to 636 °C/ Φ after 838 °C) and firing times. (b) Comparison of the oxygen diffusion rate of 0.01 by the Thiele number, 5 mm and 15 mm-thickness and various firing times. Oxygen boundary condition 0.21 atm.

The combined simulation of the oxygen and heat transfer depending on the firing temperature with the constant increasing heating rate indicates that the thermally influenced local oxygen concentration and temperature distribution are contributed by the local porosity determined by the local thermal conditions (Figure 6-24). The total length of the system was designed as 10 mm. The firing temperature increased with the constant heating rate of 7K/min for the total firing time of 90 min. The anisotropy factor related to heat transfer barrier was set as 0.5. The boundary conditions of both sides were synchronized with the increasing temperature for the heat transfer and set constant with the oxygen pressure of 0.21 atm for oxygen diffusion. The heat and mass transfer within the system was controlled by the mass balance. As the results, the open pores close to the heat source supplied from both sides lose more volume, in comparison to those in the middle part of the object, while the oxygen distribution and fast heat transfer by the open pores are lower in the middle and higher in both sides. Similar to the oxygen diffusion rate based on the direct influence of the input temperature, the reactivity of the oxygen gas and the reactants in the ceramic pastes this oxygen distribution contributes to the formation of the different concentration profile by as well.

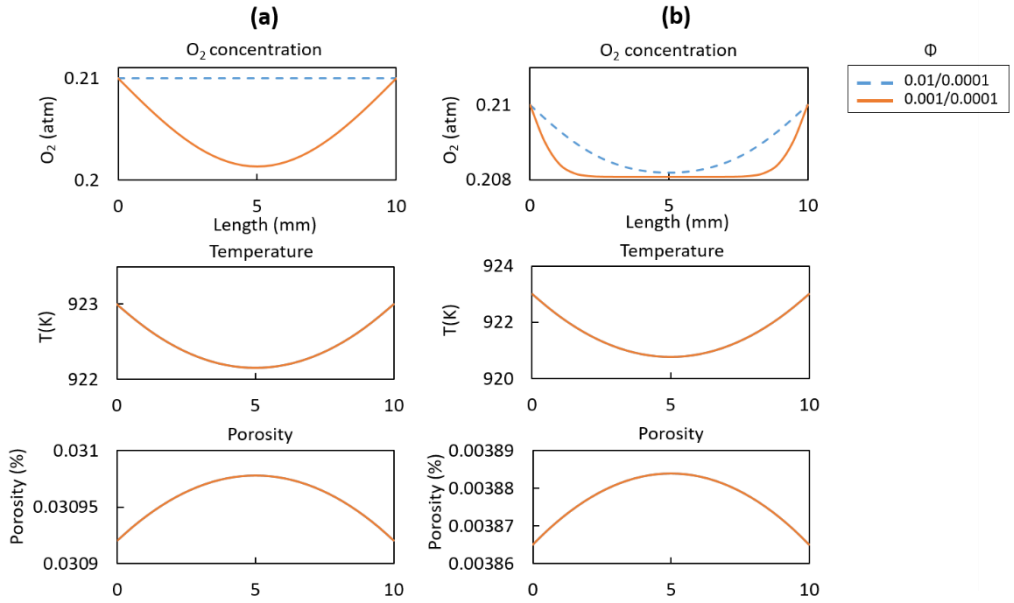

Figure 6-24. Combination of the localized oxygen concentration, temperature and porosity depending on the increasing firing temperature with the constant heating rate of 7K/min, anisotropy factor of 0.5. Boundary conditions for both sides are 0.21 atm. The total length and firing time are 10 mm and 90 min, accordingly. Comparison of the oxygen partial pressure by the different Thiele numbers (Φ up to 636 °C/ Φ after 838 °C): (a) Initial porosity for the large open pores of ca. 8% calculated from the direct observation with the unit size of 1.5-2µm; (b) Initial porosity for the large open pores of ca. 1% calculated from the direct observation with the unit size of 3.5-4µm. Pore data from *Park et al.* [90].

6.5.5. Discussion 2: Firing conditions

All the studied sites contained ceramic sherds with a highly vitreous state over 950 °C resulted from oxidizing and reducing firing, except for the Levinsadovka ceramics. The local potters practiced firing techniques for the daily ware ceramics using the both oxidizing and reducing firing atmosphere. However, in the case of Ransyrt 1 ceramics, it is often difficult to confirm, whether the potters used controlled reducing atmosphere, because calcite and calcined clays are often included in the ceramic pastes and their thermal transformation to Ca-aluminosilicates during the reducing firing is still not clear how they behave together with Fe(II). Interestingly, the ceramics found at Levinsadovka or Saf'janovo often contain calcite grains, however they show a clearer distinction between the products fired in the oxidizing and reducing atmosphere. This may be related to the degree of clay calcination. As discussed above, the ceramic matrix of several Ransyrt 1 samples contains clearly high Ca amounts.

Only the potters at Levinsadovka used reducing atmosphere, in order to achieve the vitreous phase. Ceramics from Kabardinka 2 were fired at more varied temperatures than at the other sites. The lowest and the highest firing temperature were estimated for the samples from this plateau. The wide range of the temperatures might be related with the relatively longer occupation history of the settlement or the transition from the Bronze Age to the Iron Age in the region. However, there is no daily-use ware showing the completely vitrified state. It could be possible that the potters did not reach the peak temperature above 1300 °C or they were not able to keep the long firing time for the thermal transformation of the whole area of the pottery. Although intensive firing using a blower make it possible to reach such high temperature in the open air in the high mountains, the very windy and rapidly

changing local weather conditions in the Northern Caucasus would not be easy to overcome, in order to achieve the stable firing conditions.

Almost every sample would be fired in the one-step firing process with different firing degrees within a single sherd due to the following reasons: 1) heat transfer within the sample; 2) short firing time; 3) heterogeneity in chemical, mineralogical composition; 4) unstable or uneven firing atmosphere and temperature; 5) alteration during use or after deposition. If the potters did not build the ceramic furnace for the stable firing conditions and used a simple firing installation made of stone or fired in a pit, short firing time and unstable or uneven firing atmosphere and temperature would play a crucial role for the pyrotechnology in the daily ware ceramics.

According to the kinetics of illite dehydroxylation, the non-isothermal firing with the constant heating rate of 5 min/K covers the ceramics with various degrees of dehydroxylation within 3-4 hours from the minimum pyrometamorphic degree of the ceramics at each site. However, in the real environment of firing without furnace, the heating rate and temperature difference during firing was dependent on the combustion energy by the heating source. Depending on the combustion kinetics such as kinds, size and amounts of the firing source and use of firing enhancing tools, changes in the firing temperature would show different pattern including peak temperature and duration [113-114]. The temperature would increase very rapidly at the beginning of the firing and the decreasing temperature after reaching the peak temperature would influence the further pyrometamorphic process in the composite materials. The studied sites are very windy, covered by small and short plants and the daily weather changes very often and fast, which will restrict the firing procedure in the open air.

Regarding the theoretical estimation and archaeological contexts, the possible firing practice in the ceramic production could be performed at the site generally in three ways. First, the potters put the objects in the firing source, so that the produced heat could be transferred to the objects without loss. The uneven distribution of the firing source might cause different firing time for each object. The second possible way is that the ceramic pottery was placed around the firing source in several lines. With this alignment, relatively many ceramics could be produced at the same time, saving organic fuels for the firing. The different distances between the object and firing source for the same firing time would have the same effect with the same distance to the firing source for the different firing time for each object, so that the first and second method could produce many objects with the different firing degrees. Additionally, the black coring effect and uneven distribution of the pyrometamorphic degrees within a same object observed in many ceramics of this project indicate short firing time [115]. The rapid increase of the firing temperature by the start of firing enabled to shorten the average firing time. The mass production of the ceramics at once would be more preferred, because the fire making and keeping could be still difficult for every household in this time period. The potters would perform the firing practice within a stone structure as the alternative way due to the very windy and changing daily weather at the site. The closed structure could contribute to more even distribution of the temperature around the firing place and this intermediate condition between the isothermal and non-isothermal environment would

form more symmetrical distribution pattern of the redox-thermal behavior on the ceramic cross section as consequence.

Despite the relatively simple firing practice suggested in this study, the local weather condition, vegetation and other technical issues related to the fire, the firing practice at the studied site would be a labor-intensive work during these prolonged time periods.

6.6. References

1. Jiang, T., Li, G., Qiu, G., Fan, X., Huang, Z. Thermal activation and alkali dissolution of silicon from illite. Appl. Clay. Sci. 40 (2008) 81-89. https://doi.org/10.1016/j.clay.2007.08.002.

2. Stevenson, C. M., Gurnick, M. Structural Collapse in kaolinite, montmorillonite and illite clay and its role in the ceramic rehydroxylation dating of low-fired earthenware. J. Archaeol. Sci. 69 (2016) 54-63. https://doi.org/10.1016/j.jas.2016.03.004.

3. Ptáček, P., Šoukal, F., Opravil, T., Nosková, M., Havlica, J., Brandštetr, J. Mid-Infrared spectroscopic study of crystallization of cubic spinel phase from metakaolin. J. Solid State Chem. 184 (2011) 2661-2667. https://doi.org/10.1016/j.jssc.2011.07.038.

4. Ptáček, P., Opravil, T., Šoukal, F., Havlica, J., Holešinsky, R. Kinetics and mechanism of formation of gehlenite, Al-Si spinel and anorthite from the mixture of kaolinite and calcite. Solid State Sci. 26 (2013) 53-58. https://doi.org/10.1016/j.solidstatesciences.2013.09.014.

5. De Benedetto, G.E., Laviano, R., Sabbatini, L., Zambonim, P.G. Infrared spectroscopy in the mineralogical characterization of ancient pottery. J Cult. Herit. 3 (2002) 177-186. https://doi.org/10.1016/S1296-2074(02)01178-0.

6. Park, K.S., Milke, R., Efthimiopoulos, I., Pausewein, R.R., Reinhold, S. Pyrometamorphic process of ceramic composite materials in pottery production in the Bronze/Iron Age of the Northern Caucasus (Russia). Sci. Rep. 9 (2019) 10725. https://doi.org/10.1038/s41598-019-47228-y.

7. Clark, R.N., King, T.V.V., Klejwa, M., Swayze, G.A., Vergo, N. High spectral resolution reflectance spectroscopy of minerals. J. Geophys. Res.-Sol. Ea. 95(B8) (1990) 12653-12680. https://doi.org/10.1029/JB095iB08p12653.

8. Adams, J.B. Interpretation of visible and near-infrared diffuse reflectance spectra of pyroxenes and other rock-forming minerals. In: Clarence, Jr., K. (Ed.), Infrared and Raman Spectroscopy of Lunar and Terrestrial Minerals, Academic Press: New York (1975) pp. 94-116. https://doi.org/10.1016/C2013-0-10938-5.

9. Adams, J.B. Visible and Near-Infrared Diffuse Reflectance Spectra of Pyroxenes as Applied to Remote Sensing of Solid Objects in the Solar System, J. Geophys Res. 79 (1974) 4829-4836. https://doi.org/10.1029/JB079i032p04829.

10. Gaffey, S.J., McFadden, L.A., Nash, D., Pieters, C.M. Ultraviolet, Visible, and Near-infrared Reflectance Spectroscopy: Laboratory spectra of Geologic Materials. in: Pieters, C.M., Englert, P.A.J.

(Eds.), Remote Geochemical Analysis: Elemental and Mineralogical Composition, Cambridge University Press: Cambridge (1993) pp. 43-78.

11. Leon, Y., Lofrumento, C., Zoppi, A., Carles, R., Castellucci, E.M., Sciau, Ph. Micro-Raman investigation of terra sigillata slips: a comparative study of central Italian and southern Gaul productions, J. Raman. Spectrosc. 41 (2010) 1550-1555. https://doi.org/10.1002/jrs.2678.

12. Shoval, S., Yadin, E., Panczer, G. Analysis of thermal phases in calcareous Iron Age pottery using FT-IR and Raman spectroscopy. J. Therm. Anal. Calorim. 104 (2011) 515-525. https://doi.org/10.1007/s10973-011-1518-5.

13. Weir, C.E. and Lippincott, E.R. Infrared studies of aragonite, calcite, and vaterite type structures in the borates, carbonates, and nitrates. J. Res. Natl. Stand. Sec. A. 65A(3) (1961) 173-183.

14. Henry, D.G., Watson, J.S., John, C.M. Assessing and calibrating the ATR-FTIR approach as a carbonate rock characterization tool. Sediment. Geol. 347 (2017) 36-52. https://doi.org/10.1016/j.sedgeo.2016.07.003.

15. Rathossi, C., Pontikes, Y. Effect of firing temperature and atmosphere on ceramics made of NW Peloponnese clay sediments: Part II. Chemistry of pyrometamorphic minerals and comparison with ancient ceramics. J. Eur. Ceram. Soc. 30 (2010) 1853–1866. https://doi.org/10.1016/j.jeurceramsoc.2010.02.002.

16. Nodari, L., Marcuz, E., Maritan, L. Mazzoli, C., Russo, U. Hematite nucleation and growth in the firing of carbonate-rich clay for pottery production. J. Eur. Ceram. Soc. 27 (2007) 4665–4673. https://doi.org/10.1016/j.jeurceramsoc.2007.03.031.

17. Okuma, G., Kadowaki, D., Hondo, T., Tanaka, S., Wakai, F. Interface topology for distinguishing stages of sintering. Sci. Rep. 7 (2017) 11106. 9:11595. https://doi.org/10.1038/s41598-017-11667-2.

18. Coble, R.L. Sintering Crystalline Solids. I. Intermediate and Final State Diffusion Models. J. Appl. Phys. 32 (1961) 787–792.

19. De Jonghe, L.C., Rahaman, M.N. Sintering of Ceramics. In Handbook of Advanced Ceramics: Materials, Applications, Processing and Properties; Sōmiya, S., Ed.; Elsevier Inc.: Waltham, MA, Oxford, Amsterdam, Volume 1–2 (2003) pp. 187–264. https://doi.org/10.1016/B978-012654640-8/50006-7.

20. Ferrer, S., Mezquita, A., Gómez-Tena, M.P., Machí, C., Monfort, E. Estimation of the heat of reaction in traditional ceramic compositions. Appl. Clay Sci. 108 (2015) 28–39. https://doi.org/10.1016/j.clay.2015.02.019.

21. Vogel, H. Morphological determination of pore connectivity as a function of pore size using serial sections. Eur. J. Soil Sci. 48 (1997) 365–377. https://doi.org/10.1111/j.1365-2389.1997.tb00203.x.

22. Vogel, H.-J., Weller, U., Schlüter, S. Quantification of soil structure based on Minkowski functions. Comput. Geosci. 36 (2010) 1236–1245. https://doi.org/10.1016/j.cageo.2010.03.007.

23. Vogel, H.-J., Roth, K. Quantitative morphology and network representation of soil pore structure. Adv. Water Resour. 24, (2001) 233–242. https://doi.org/10.1016/S0309-1708(00)00055-5.

24. Legland, D., Kiêu, K., Devaux, M.F. Computation of Minkowski measures on 2D and 3D binary images. Image Anal. Stereol. 26 (2007) 83–92.

25. Lehmann, G., Legland, D. Efficient N-Dimensional surface estimation using Crofton formula and run-length encoding. Insight J. (2012). https://hdl.handle.net/10380/3342 (accessed on 15 October 2018).

26. Shoemake, K. III.5.—Euler Angle Conversion. In Graphics Gems; Heckbert, P.S., Ed.; Elsevier Inc.: London, UK,Volume IV (1994) pp. 222–229. https://doi.org/10.1016/B978-0-12-336156-1.50030-6.

27. Pavanati, H.C., Maliska, A.M., Klein, A.N., Muzart, J.L.R. Comparative study of porosity and pores morphology of unalloyed iron sintered in furnace and plasma reactor. Mat. Res. 10 (2007) 87–93. http://dx.doi.org/10.1590/S1516-14392007000100019.

28. Brownell, W.E. Black Coring in Structural Clay Products. J. Am. Ceram. Soc. 40(6) (1957) 179-187. https://doi.org/10.1111/j.1151-2916.1957.tb12600.x.

29. Abdrakhimov, V.Z., Abdrakhimova, E.C. Formation of the black core in high-speed firing of floor tiles. Glass and Ceramics 56(7-8) (1999) 263–265. https://doi.org/10.1007/BF02681509.

30. Rathossi, C., Pontikes, Y. Effect of firing temperature and atmosphere on ceramics made of NW Pelephonnese clay sediments, Part I: Reaction paths, crystalline phases, microstructure and colour. J. Eur. Ceram. Soc. 30 (2010) 1853-1866. https://doi.org/10.1016/j.jeurceramsoc.2010.02.002.

31. Murad, E., Wagner, U. The thermal behavior of an Fe-rich illite. Clay Miner. 31 (1996) 45-52. https://doi.org/10.1180/claymin.1996.031.1.04.

32. Ponomar, V. P., Dudchenko, N. O. & Brick, A. B. Reduction roasting of hematite to magnetite using carbohydrates. Int. J. Miner. Process. 164 (2017) 21–25. https://doi.org/10.1016/j.minpro.2017.05.005.

33. Gualtieri, A. F. and Venturelli, P. In situ strudy of the goethite-hematite phase transformation by real time synchrotron powder diffraction. Am. Mineral. 84 (1999) 895-904.

34. Pomiès, M. P., Morin, G., Vignaud, C. XRD study of the goethite-hematite transformation: Application to the identification of heated prehistoric pigments. Eur. J. Inorg. Chem. 35(1) (1998) 9-25. https://doi.org/10.1016/S0992-4361(98)80011-8.

35. Patra, A. K., Kundu, S. K., Bhaumik, A., Kim, D. Morphology evolution of single-crystalline hematite nanocrystals: magnetically recoverable nanocatalysts for enhanced facet-driven photoredox activity. Nanoscale 8 (2016) 365-377. https://doi.org/10.1039/C5NR06509G.

36. Woo, K., Lee, H. J. Synthesis and magnetism of hematite and maghemite nanoparticles. J. Magn. Magn. Mater 272-276 (2004) e1155-e1156. https://doi.org/10.1016/j.jmmm.2003.12.201.

37. Pomiès, M. P., Menu, M. Red paleolithic pigments: natural hematite or heated goethite? Archaeometry 41(2) (1999) 275-285. https://doi.org/10.1111/j.1475-4754.1999.tb00983.x.

38. Wang, X. and Xiao, P. Characterisation of clay sintering process using impedance spectroscopy. J, Eur. Ceram. Soc. 22(4) (2002) 471-478. https://doi.org/10.1016/S0955-2219(01)00335-1.

39. Ferrer, S., Mezquita, A., Gomez-Tena, M. P., Machi, C., Monfort, E. Estimation of the heat of reaction in traditional ceramic compositions. Appl. Clay. Sci. 108 (2015) 28-39. https://doi.org/10.1016/j.clay.2015.02.019.

40. McConville, C. J. and Lee, W. E. Microstructural Development on Firing Illite and Smectite Clays Compared with that in Kaolinite. J. Am. Ceram. Soc. 88(8) (2005) 2267-2276. https://doi.org/10.1111/j.1551-2916.2005.00390.x.

41. Escalera, E., Antti, M. L. and Odén, M. Thermal treatment and phase formation in kaolinite and illite based clays from tropical regions of Bolivia, 6th EEIGM International Conference on Advanced Materials Research, IOP Conf. Series: Materials Science and Engineering 31 (2012) 012017, https://doi.org/10.1088/1757-899X/31/1/012017.

42. De Jonghe, L. C. and Rahaman, M. N. Sintering of Ceramics, in: S. Sōmiya (ed.), Handbook of Advanced Ceramics: Materials, Applications, Processing and Properties 1-2 (Elsevier Inc.) (2003) 187-264, https://doi.org/10.1016/B978-012654640-8/50006-7.

43. Mysen, B.O., Virgo, D., Neumann, E. R., Seifert, F. A. Redox equilibria and the structural states of ferric and ferrous iron in melts in the system CaO-MgO-Al_2O_3-SiO_2-Fe-O: relationships between redox equilibria, melt structure and liquidus phase equilibria. Am. Mineral. 70 (1985) 317-331.

44. Maysen, B.O. and Virgo, D., Viscosity and structure of iron- and aluminium-bearing calcium silicate melts at 1 atm. American Mineralogist 70 (1985) 487-498.

45. Ottonello, G., Moretti, R., Marini, L., Zuccolini, M. V. Oxidation state of iron in silicate glasses and melts: a thermochemical model. Chemical Geology 174 (2001) 157-179. https://doi.org/10.1016/S0009-2541(00)00314-4.

46. Knipping, J. L., Behrens, H., Wilke, M., Göttlicher, J., Stabile, P. Effect of oxygen fugacity on the coordination and oxidation state of iron in alkali bearing silicate melts. Chemical Geology 411 (2015) 143-154. https://doi.org/10.1016/j.chemgeo.2015.07.004.

47. Usman, M., Abdelmoula, M., Faure, P., Ruby, C., Hanna, K. Transformation of various kinds of goethite into magnetite: Effect of chemical and surface properties. Geoderma 197-198 (2013) 9-16. https://doi.org/10.1016/j.geoderma.2012.12.015.

48. X. Shi, T. Huang, Effect of pore-size distribution in cathodic gas diffusion layers on the electricity generation of microbial fuel cells (MFCs), RSC Adv. 5(124) (2015) 102555-102559. https://doi.org/10.1039/C5RA19811A.

49. Lavikainen, L.P., Hirvi, J.T., Kasa, S., Pakkanen, T.A. Interaction of octahedral Mg(II) and tetrahedral Al(III) substitutions in aluminium-rich dioctahedral smectites. Theor. Chem. Acc. 135 (2016) 85. https://doi.org/10.1007/s00214-016-1846-4.

50. Ilgen, A.G., Kukkadapu, R.K., Leung, K., Washington, R.E. “Switching on” iron in clay minerals, Environ. Sci.: Nano. 6 (2019) 1704-1715, https://doi.org/10.1039/C9EN00228F.

51. F. Panerai, J.C. Ferguson, J. Lachaud, A. Martin, M.J. Gasch, N.N. Mansour, Micro-tomography based analysis of thermal conductivity, diffusivity and oxidation behavior of rigid and flexible fibrous insulators, Int. J. Heat. Mass. Transf., 108 (A) (2017) 801-811. https://doi.org/10.1016/j.ijheatmasstransfer.2016.12.048.

52. Stucki, J.W., Bailey, G.W., Gan, H. Oxidation-reduction mechanisms in iron-bearing phyllosilicates, Appl. Clay Sci. 10 (1996) 417-430. https://doi.org/10.1016/0169-1317(96)00002-6.
53. Wolters, F., Emmerich, K. Thermal reactions of smectites – Relation of dehydroxylation temperature to octahedral structure, Thermochim. Acta. 462 (2007) 80-88. https://doi.org/10.1016/j.tca.2007.06.002.
54. Mysen, B.O., Virgo, D., Neumann, E.R., Seifert, F.A. Redox equilibria and the structural states of ferric and ferrous iron in melts in the system CaO-MgO-Al_2O_3-SiO_2-Fe-O: relationships between redox equilibria, melt structure and liquidus phase equilibria. Am. Min. 70 (1985) 317-331.
55. Maysen, B.O., Virgo, D. Viscosity and structure of iron- and aluminium-bearing calcium silicate melts at 1 atm. Am. Min. 70 (1985) 487-498.
56. Ottonello, G., Moretti, R., Marini, L., Zuccolini, M.V. Oxidation state of iron in silicate glasses and melts: a thermochemical model, Chem. Geol. 174 (2001) 157-179. https://doi.org/10.1016/S0009-2541(00)00314-4.
57. Knipping, J.L., Behrens, H., Wilke, M., Göttlicher, J., Stabile, P. Effect of oxygen fugacity on the coordination and oxidation state of iron in alkali bearing silicate melts. Chem. Geol. 411 (2015) 143-154. https://doi.org/10.1016/j.chemgeo.2015.07.004.
58. Park, K.S., Reinhold, S., Milke, R. Pottery production technology and technological style in the North Caucasus (Russia) in the Bronze/Iron Age: Archaeological characterization from archaeometric results. (in prep.).
59. Drits, V.A., Beson, G., Muller, F. An improved model for structural transformations of heat-treated aluminous dioctahedral 2:1 layer silicates. Clays. Clay. Miner. 43(6) (1995) 718-731. https://doi.org/10.1346/CCMN.1995.0430608.
60. Wang, G., Wang, H., Zhang, N. In situ high temperature X-ray diffraction study of illite. Appl. Clay. Sci. 146 (2017) 254-263. https://doi.org/10.1016/j.clay.2017.06.006.
61. Gualtieri, A. F., Ferrari, S., Leoni, M., Grathoff, G., Hugo, R., Shatnawi, M., Paglia, G. and Billinge, S. Structural characterization of the clay mineral illite-1M. J. Appl. Cryst. 41 (2008) 402–415. https://doi.org/10.1107/S0021889808004202.
62. Cultrone, G., Rodriguez-Navarro, C., Sebastian, E., Cazalla, O., De La Torre, M.J. Carbonate and silicate phase reactions during ceramic firing. Eur. J. Mineral. 13 (2001) 621-634. https://doi.org/10.1127/0935-1221/2001/0013-0621.
63. Trindade, M. J., Dias, M. I., Coroado, J., Rocha, F. Mineralogical transformations of calcareous rich clays with firing: A comparative study between calcite and dolomite rich clays from Algarve, Portugal, Appl. Clay. Sci. 42 (2009) 345-355. https://doi.org/10.1016/j.clay.2008.02.008.
64. Laita, E., Bauluz, B. Mineral and textural transformations in aluminium-rich clays during ceramic firing. Appl. Clay. Sci. 152 (2018) 284-294. https://doi.org/10.1016/j.clay.2017.11.025.
65. Gualtieri, A.F., Ferrari, S. Kinetics of illite dehydroxylation, Phys. Chem. Minerals. 33 (2006) 490-501. https://doi.org/10.1007/s00269-006-0092-z.

66. Vyazovkin, S., Wight, C.A. Isothermal and non-isothermal kinetics of thermally stimulated reactions of solids, Int. Rev. Phys. Chem. 17(3) (1998) 407-433. https://doi.org/10.1080/014423598230108.
67. Liu, Z., Wang, Q., Zou, Z., Tan, G. Arrhenius parameters determination in non-isothermal conditions for the uncatalyzed gasification of carbon by carbon dioxide, Thermochim. Acta. 512 (2011) 1-4. https://doi.org/10.1016/j.tca.2010.08.014.
68. Drits, A.V., Derkowski, A., McCarty, D.K. Kinetics of partial dehhydroxylation in dioctahedral 2:1 layer clay minerals. Am. Mineral. 97 (2012) 930-950. https://doi.org/10.2138/am.2012.3971.
69. Heller-Kallai, L., Lapides, I. Dehydroxylation of muscovite: study of quenched samples. Phys. Chem. Miner. 42 (2015) 835-845. https://doi.org/10.1007/s00269-015-0767-4.
70. Heller-Kallai, L., Rozenson, I. Dehydroxylation of dioctahedral phyllosilicates, Clays. Clay. Miner. 28 (1980) 355–368. https://doi.org/10.1346/CCMN.1980.0280505.
71. Litovsky, E.Y., Shapiro, M. Gas pressure and temperature dependences of thermal conductivity of porous ceramic materials: part 1, refractories and ceramics with porosity below 30%. J. Am. Ceram. Soc. 75(12) (1992) 3425-3439. https://doi.org/10.1111/j.1151-2916.1992.tb04445.x.
72. Litovsky, E.Y., Shapiro, M., Shavit, A. Gas pressure and temperature dependences of thermal conductivity of porous ceramic materials: part 2, refractories and ceramics with porosity exceeding 30%. J. Am. Ceram. Soc. 79(5) (1996) 1366-1376. https://doi.org/10.1111/j.1151-2916.1996.tb08598.x.
73. Hong, X., Hui, L. An empirical formula of mean specific heat capacity of ideal gases. In: Su, Y., Chang, G., Luo, Z. (Eds.), Proceedings of the 2015 International Conference on Education, Management, Information and Medicine, The 5th International Conference on Education, Management, Information and Medicine (EMIM 2015), April 24-26, 2015, Shenyang, China, Atlantis Press: Paris, pp. 1083-1086. https://doi.org/10.2991/emim-15.2015.206 https://doi.org/10.2991/emim-15.2015.206.
74. Gibert, B., Mainprice, D., Effect of crystal preferred orientations on the thermal diffusivity of quartz polycrystalline aggregates at high temperature. Tectonophysics 465 (2009) 150-163. https://doi.org/10.1016/j.tecto.2008.11.006.
75. Lin, W., Fulton, P.M., Harris, R.N., Tadai, O., Matsubayashi, O., Tanikawa, W., Kinoshita, M. Thermal conductivities, thermal diffusivities, and volumetric heat capacities of core samples obtained from the Japan Trench Fast Drilling Project (JFAST), Earth. Planet. Sp. 66 (2014) 48. https://doi.org/10.1186/1880-5981-66-48.
76. Arens, P.L. A study of the differential thermal analysis of clays and clay minerals. doctoral thesis, Wageningen University: Netherlands (1951).
77. Hickox, C.E., McVey, D.F., Mille, J.B., Olson, L.O., Silva, A.J. Thermal conductivity measurements of Pacific illite sediment. Int. J. Thermophys. 7(4) (1986) 755–764. https://doi.org/10.1007/BF00503833.
78. Miao, S.Q., Li, H.P., Chen, G. Temperature dependence of thermal diffusivity, specific heat capacity, and thermal conductivity for several types of rocks. J. Therm. Anal. Calorim. 115(2) (2014) 1057-1063. https://doi.org/10.1007/s10973-013-3427-2.

79. Ortiz de Zárate, J.M., Hita, J.L., Khayet, M., Legido, J.L. Measurement of the thermal conductivity of clays used in pelotherapy by the multi-current hot-wire technique. Appl. Clay. Sci. 50(3) (2010) 423-426. https://doi.org/10.1016/j.clay.2010.08.012.

80. Skauge, A., Fuller, N., Hepler, L.G. Specific heats of clay minerals: Sodium and calcium kaolinites, sodium and calcium montmorillonites, illite, and attapulgite. Thermochim. Acta. 61(1–2) (1983) 139-145. https://doi.org/10.1016/0040-6031(83)80310-4.

81. Hirono, T., Hamada, Y. Specific heat capacity and thermal diffusivity and their temperature dependencies in a rock sample from adjacent to the Taiwan Chelungpu fault. J. Geophys. Res.-Sol Ea. 115(B5) (2010) B05313. https://doi.org/10.1029/2009JB006816.

82. Horai, K. Thermal conductivity of rock-forming minerals, J. Geophys. Res. 76(5) (1971) 1278-1308.

83. Abuel-Naga, H.M., Bergado, D.T., Bouazza, A. Thermal conductivity evolution of saturated clay under consolidation process. Int. J. Geomech. 8 (2008) 114-122. https://doi.org/10.1061/(ASCE)1532-3641(2008)8:2(114).

84. Goto, S., Matsubayashi, O. Inversion of needle-probe data for sediment thermal properties of the eastern flank of the Juan de Fuca Ridge. J. Geophys. Res. 113 (2008) B08105. https://doi.org/10.1029/2007JB005119.

85. Húlan, T., Trník, A., Štubňa, I., Bačík, P., Kaljuvee, T., Vozár, L. Development of Young's modulus of illitic clay during heating up to 1100 °C. Medžiagotyra. 21(3) (2015) 429-434. http://dx.doi.org/10.5755/j01.ms.21.3.7152.

86. Jankula, M., Húlan, T., Štubňa, I., Ondruška, J., Podoba, R., Šín, P., Bačík, P., Trník, A. The influence of heat on elastic properties of illitic clay Radobica. J. Ceram. Soc. Jpn. 123(1441) (2015) 874-879. https://doi.org/10.2109/jcersj2.123.874.

87. Xie, X., Lu, Y., Ren, T., Horton, R. An empirical model for estimating soil thermal diffusivity from texture, bulk density, and degree of saturation. J. Hydrometeorol. 19 (2018) 445-457. https://doi.org/10.1175/JHM-D-17-0131.1.

88. Hein, A., Müller, N., Day, P.M., Kilikoglou, V. Thermal conductivity of archaeological ceramics: The effect of inclusions, porosity and firing temperature. Thermochim. Acta. 480 (2008) 35-42. https://doi.org/10.1016/j.tca.2008.09.012.

89. Etukudoh, A.B. Effect of cassava peel on the insulating properties of Ogugu clay deposit. Int. Adv. Res. J. Sci. Eng. Technol. 4(8) (2016) 273-280.

90. Park, K.S., Milke, R., Rybacki, E., Reinhold, S. Application of image analysis for the identification of prehistoric ceramic production technologies in the North Caucasus (Russia, Bronze/Iron Age). Heritage 2 (2019) 2327-2342. https://doi.org/10.3390/heritage2030143.

91. Bruggeman, D.A.G. Berechnung verschiedener physikalischer Konstanten von heterogenen Substanzen. I. Dielektrizitätskonstanten und Leitfähigkeiten der Mischkörper aus isotropen Substanzen. Annal. der. Physik. 24(5) (1935) 636-664. https://doi.org/10.1002/andp.19354160705.

92. Shen, L., Chen, Z. Critical review of the impact of tortuosity on diffusion. Chem. Eng. Sci. 62 (2007) 3748-3755. https://doi.org/10.1016/j.ces.2007.03.041.

93. Hein, A., Kilikoglou, V. Modelling of thermal behavior of ancient metallurgical ceramics. J. Am. Ceram. Soc. 90(3) (2007) 878 – 884. https://doi.org/10.1111/j.1551-2916.2006.01466.x.

94. Huang, C., Qian, X., Yang, R. Thermal conductivity of polymers and polymer nanocomposites. Mat. Sci. Eng. R 132 (2018) 1-22. https://doi.org/10.1016/j.mser.2018.06.002.

95. Skibinski, J., Cwieka, K., Ibrahim, S.H., Wejrzanowski, T. Influence of pore size variation on thermal conductivity of open-porous foams. Materials 2019, 12(12) 2017. https://doi.org/10.3390/ma12122017.

96. Tu, Z., Mao, J., Han, X., He, Z. Prediction model for the anisotropic thermal conductivity of a 2.5-d braided ceramic matrix composite with thin-wall structure. Appl. Sci. 9(5) (2019) 875. https://doi.org/10.3390/app9050875.

97. Jorand, R., Fehr, A., Koch, A., Clauser, C. Study of the variation of thermal conductivity with water saturation using nuclear magnetic resonance. J. Geophys. Res. 116 (2011) B08208. https://doi.org/10.1029/2010JB007734.

98. Yu, C., Zhang, J., Tian, W., Fan, X., Yao, Y. Polymer composites based on hexagonal boron nitride and their application in thermally conductive composites. RSC Adv. 8 (2018) 21948-21967. https://doi.org/10.1039/C8RA02685H.

99. Ordonez-Miranda, J., Alvarado-Gil, J.J. Effect of the pore shape on the thermal conductivity of porous media. J. Mater. Sci. 47(18) (2012) 6733–6740. https://doi.org/10.1007/s10853-012-6616-7.

100. Çeçen, A., Wargoa, E.A., Hannaa, A.C., Turner, D.M., Kalidindi, S.R., Kumbur, E.C. 3-D microstructure analysis of fuel cell materials: spatial distributions of tortuosity, void size and diffusivity. J. Electrochem. Soc. 159(3) (2012) B299-B307. https://doi.org/10.1149/2.068203jes.

101. Fuller, E.N., Shettler, P.D., Giddings, J.C. New method for prediction of binary gas diffusion coefficients. Ind. Eng. Chem. 58(5) (1966) 18-27. https://doi.org/10.1021/ie50677a007.

102. Fuller, E.N., Ensley, K., Giddings, J.C. Diffusion of halogenated hydrocarbons in helium. The effect of structure on collision cross sections. J. Phys. Chem. 73(11) (1969) 3679-3685. https://doi.org/10.1021/j100845a020.

103. Tang, M.J., Cox, R.A., Kalberer, M. Compilation and evaluation of gas phase diffusion coefficients of reactive trace gases in the atmosphere: volume 1. Inorganic compounds. Atmos. Chem. Phys. 14 (2014) 9233-9247. https://doi.org/10.5194/acp-14-9233-2014.

104. Matyka, M., Khalili, A., Koza, Z. Tortuosity-porosity relation in porous media flow. Phys. Rev. E 78 (2008) 02636. https://doi.org/10.1103/PhysRevE.78.026306.

105. Ghanbarian, B., Hunt, A.G., Ewing, R.P., Sahimi, M. Tortuosity in porous media: a critical review. Soil. Sci. Soc. Am. J. 77 (2013) 1461-1477. https://doi.org/10.2136/sssaj2012.0435.

106. Pisani, L. Simple expression for the tortuosity of porous media. Transp. Porous. Med. 88 (2011) 193. https://doi.org/10.1007/s11242-011-9734-9.

107. Gozzi, D., Guzzardi, G., Salleo, A. High temperature reactivity of different forms of carbon at low oxygen fugacity. Solid. State. Ion. 83 (1996) 177-189. https://doi.org/10.1016/0167-2738(95)00252-9.

108. Gremyachkin, V.M. Kinetics of heterogeneous reactions of carbon and oxygen during combustion of porous carbon particles in oxygen. Combust. Explos. Shock. Waves. 42(3) (2006) 254-263. https://doi.org/10.1007/s10573-006-0048-0.

109. Heidenreich, S., Müller, M., Foscolo, P.U. Advanced Biomass Gasification, Academic Press, London and Oxford, UK, San Diego and Cambridge, USA, 2016, pp. 4-10. https://doi.org/10.1016/B978-0-12-804296-0.00002-6.

110. Hu, W., Marek, E., Donat, F., Dennis, J.S., S.A. Scott, A thermogravimetric method for the measurement of CO/CO_2 ratio at the surface of carbon during combustion. P. Combust. Inst. 37(3) (2019) 2987-2993. https://doi.org/10.1016/j.proci.2018.05.040.

111. Essenhigh, R.H. Rate equations for the Carbon-Oxygen reaction: an evaluation of the Langmuir Adsorption Isotherm at atmospheric pressure. Energ. Fuel. 5 (1991) 41-46. https://doi.org/10.1021/ef00025a005.

112. Komadel, P., Madejova, J., Stucki, J.W. Structural Fe (III) reduction in smectites. Appl. Clay Sci. 34 (2006) 88-94. https://doi.org/10.1016/j.clay.2005.10.016.

113. Kuo, K.K.Y. Principles of Combustion. Wiley Hoboken: New Jersey, 2 edition (2005).

114. F.L. Browne, Theories of the Combustion of Wood and Its Control: A Survey of the Literature Forest Products Laboratory. Forest Service, U.S. Department of Agriculture, Issue 2136 of Report (Forest Products Laboratory (U.S.))) (1958).

115. L. Gredmaier, C.J. Banks, R.B. Pearce, Calcium and sulphur distribution in fired clay brick in the presence of a black reduction core using micro X-ray fluorescence mapping. Constr. Build. Mater. 25(12) (2011) 4477-4486. https://doi.org/10.1016/j.conbuildmat.2011.03.054.

Chapter 7. Conclusions

The multiproxy and multiscale approach using PM, XRD and SEM/SEM-EDS/WDS, FTIR/SR-FTIR and Raman spectroscopy, 3D μ-CT and image analysis, covering from micro- to meso-scale in cm, enabled us to characterize the technical part of the pottery production at Ransyrt 1 and Kabardinka 2 in the North Caucasus in the LBA/EIA. Each measurement with the selected range of the spatial resolution was performed step-by-step, categorizing the objects and selecting the representative samples for the next measurement in the higher resolution, so that all the ceramics could be assigned to corresponding groups according to the detailed technological characteristics in the pottery production, despite the high heterogeneity of the archaeological ceramics excavated at these sites. This project focused on three subtopics which have considered as the important production steps of the ceramic pottery in ceramic archaeometry: preparation of the ceramic pastes, formation of the pottery and firing techniques. The results contributed to the characterization of the local technological styles in this ceramic production, described as follows.

First, the ceramic pastes were prepared with the soils around the site. The geoarchaeological survey around the archaeological sites revealed that the soils at Ransyrt 1 were less developed than that of Kabardinka 2 located on the lower mountain plateau. The soils around Kabardinka 2 show more reddish color, probably due to the influence of Fe-rich phases. These geological environments of the archaeological sites were reflected in the ceramic pastes. The coarse sand grains in the ceramics excavated at Ransyrt 1 had the bigger grain size and the lower circularity than those in the Kabardinka 2 ceramics. The chemical composition of all the grains smaller than 50 μm present in the samples was distinguished, according to the site. The ceramics from Ransyrt 1 contained more objects rich in Ca and Mg, while those from Kabardinka 2 were relatively Fe-rich, reflecting the geological environment. This site-specific characteristic of the pastes was proved at the other sites located in the alluvial zones around the Sea of Azov, Levinsadovka and Saf'janovo which were occupied by the LBA/FBA. Interestingly, most ceramics of the studied sites contained the mixture of *cv*- and *tv*-1M illite as the common dominant clay mineral. This indicates that the potters at the site gathered sediments in the alteration process, although illite is one of the most common clay minerals.

The build-up process of the inner structure of the ceramics was similar for both sites. The potters constructed the different parts of the ceramics continuously by pinching, pulling or pressing, or formed modular slabs and attached to each other. The relatively irregular alignment of the grains indicates that the objects were formed principally by hands. The considerable amounts of pores especially around the coarse grains in the Ransyrt 1 ceramics seem to be caused by higher grain size distribution and irrelevant to the formation techniques. This might have influenced the thickness of the ceramics, because the wall and bottom fragments from Ransyrt 1 is thicker than those from Kabardinka 2.

The firing technique practiced at each site was reconstructed based on the complex pyrometamorphic process of the illite-based composite materials. Direct measurements of the original samples in various

observation scales enabled to detect the degree of illite dehydroxylation and dissociation of the Ca-carbonates, crystallization of hematite, spinel and gehlenite, providing thresholds of firing temperatures: 675 °C <; 675-700 °C; 700-750 °C; 750-950 °C; 950-1050 °C; 1050-1100 °C. Together with the results of the chemical and mineralogical composition of the ceramic pastes, the changes in the mineralogy and morphology of the ceramic matrix could be classified into these groups. The firing temperature ranges were similar for both sites, although the range of the firing temperatures is slightly wider for Kabardinka 2 ceramics than Ransyrt 1 ones, possibly influenced by the longer occupation history of the Kabardinka 2 or by the relatively finer grain size distribution of the ceramic pastes and finer structure at the low firing temperature. Moreover, the potters performed similar firing practice in the non-isothermal condition with the increasing temperatures. The atmosphere of the firing place was controlled for the reduction or oxidization, although the redox state in most ceramics under oxidizing firing was localized within a sample, because of the Fe/C/S-bearing phases originated from the soils. In the meanwhile, the temperature distribution in the porous ceramic structure was not huge, above all due to the thickness of the fragments ranging from 0.5 and 1.5 cm. According to the kinetics of illite dehydroxylation in the ideal conditions with the heating rate of 5K/min, the maximum firing degrees could be achieved within three hours after the minimum firing degree for ceramic pottery at each site. This means that the firing step must not need the furnace structure for the intensive and isothermal firing conditions, because the average firing degrees could be acquired by the instant firing for 2-3 hours. In the real practice, temperature changes by the combustion energy are bigger. The ceramics with various firing degrees could be produced at the same time by this type of firing. The objects might be aligned around the firing source with various distances, put in the firing source or the intensity of the fire would not be same for every firing practice. However, due to the weather conditions at the mountain sites which change quickly with the strong winds and rains, the potters would need a structure which can protect the fire and objects from the weather or should dig a space. Moreover, they would prepare organic materials which can produce enough energy by the combustion. Regarding the rare vegetation and absence of the trees at Ransyrt 1 and Kabardinka 2, the supply of enough firing source for a few hours of firing would be one of the crucial issues at each site.

In general, the reconstructed techniques for the preparation of the ceramic pastes, formation of the ceramic body and its firing in the pottery production at both archaeological sites contain similar characteristics caused by the human induced factor. The potters at the site of the MBA/LBA had similar practice in the material production with the people at the site occupied by the LBA/EIA. Additionally, the relatively high deviation of the measurement data is interpreted as the result from the individual decision making in the production process. In the meanwhile, nature induced factors, above all, the resources for the ceramic paste caused the site-specific properties of the ceramics during the production. The selection and preparation of the resource from the local environment caused different textures and micro-morphology, thickness and colours due to the shape parameters and mineralogical and chemical composition of the local sediments. During the firing step, this local resource-based heterogeneity

became bigger, because the mineralogical transformation, dehydroxylation of illite, porosity and pore evolution, amounts of the Fe-, C- and S-bearing phases and water, heat transfer and oxygen diffusion work together and form complex features and properties in the final product.

These general characteristics in the pottery production contributed to the formation of the resource-driven local technological styles at the studied sites and probably in the neighbour settlements with the similar lifestyle in the North Caucasus in the same time period. The local societies in this region had a combined form of the semi-sedentary and semi-mobile lifestyle on the mountain plateaus with the less soil development and vegetation. In this society type, the use of the local resource and the relatively instant firing would be preferred to produce pottery for the regular supply in considerable amounts for each household and institution. The potters transferred their knowledge and practice for the ceramic production, based on the individual decision making over the region and generations. This would lead to distribute the resource-driven local technological styles in the North Caucasus in the Bronze and Iron Age.

Appendix 1. Field work for the soil study around Ransyrt 1 and Kabardinka 2

(01.09.2016-16.09.2016)

A1.1. Map

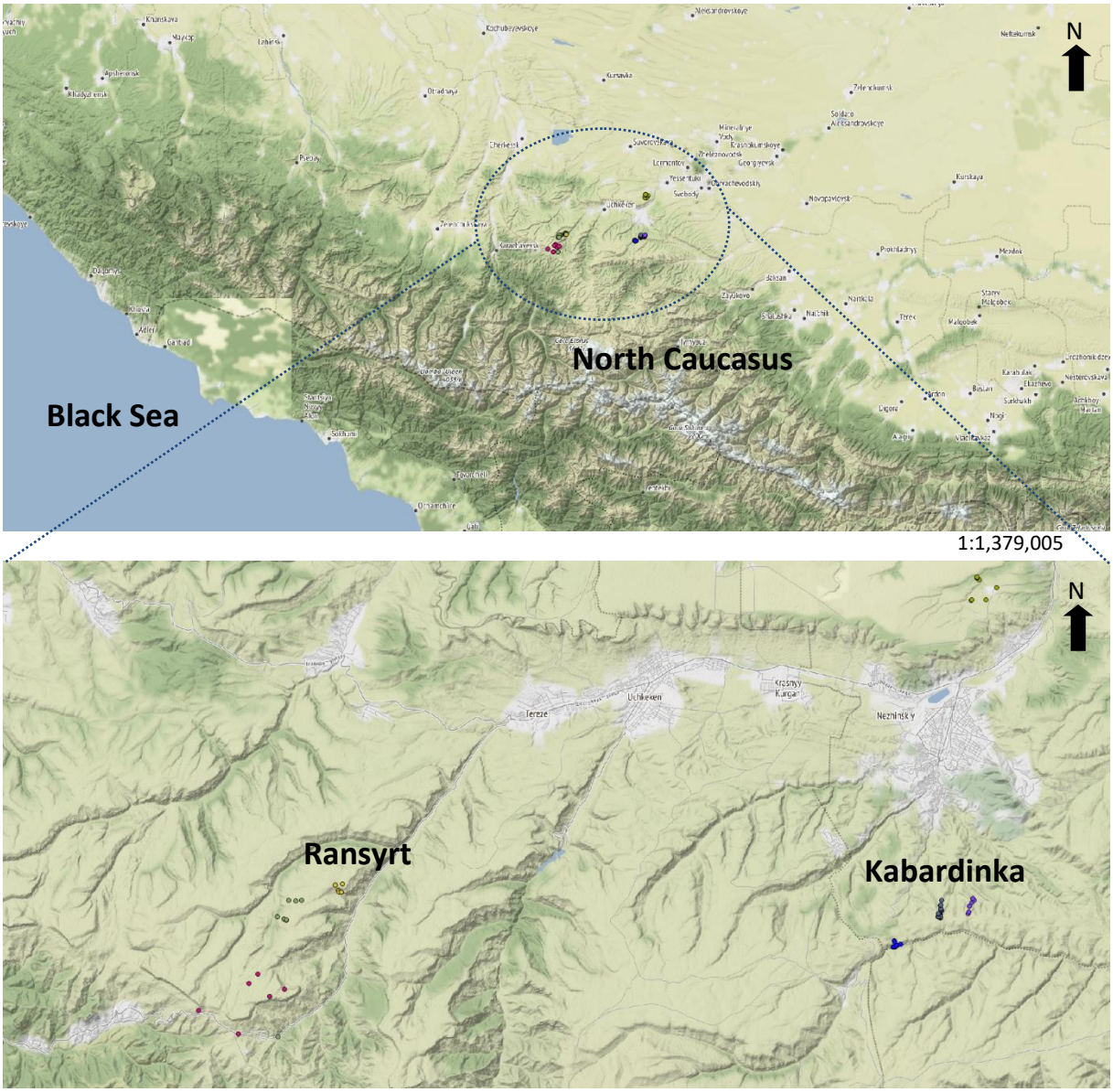

Figure A1-1. Places of soil/rock sampling marked as a colored dot (maps: created by QGIS 2.18.0 with open layers from OSM/Stamen, map tiles by Stamen Design, under CC BY 3.0. data by OpenStreetMap, under ODbL (maps.stamen.com).

A1.2. List

A1.2.1. Around Ransyrt 1

Sediments

Site no.	Sample no. 1 (site)	Sample no. 2
1-10	130916-Ran6env-2	sample 5
1-11	130916-Ran6env-1	sample 1
1-12	130916-Ran6env-2	sample 6

1-15	130916-Ran7-1	sample 1
1-16	130916-Ran6env-2	sample 4
1-19	130916-Ran6env-1	sample 3
1-20	130916-Ran7-1	sample 2
1-21	130916-Ran7-2	sample 3
1-23	120916-Ran1-7	sample 10
1-24	120916-Ran1-5	sample 6
1-25	120916-Ran1-1	sample 1
1-26	120916-Ran1-6	sample 7
1-27	120916-Ran1-2	sample 3
1-28	120916-Ran1-7	sample 9
1-29	120916-Ran1-6	sample ?
1-31	120916-Ran1-1	sample 2
1-32	120916-Ran1-5	sample 4
2-1	120916-Ran1-5	sample 5
2-2	130916-Ran6env-1	sample 2

Stones

Site no.	Sample no. 1 (site)	Sample no. 2
1	130916-RAN-1	stone 2-1
2	130916-RAN-1	stone 2-(1)
3	060916-KAB2-4	stone 1-(1)
4	130916-Ran6emv-3	stone 2
6	120916-Ran1-3	stone 3
8	130916-RAN-2	stone 3-(1)
9	120916-Ran1-2	stone 2-(1)
10	130916-RAN-2	stone 2
16	130916-RAN-1	stone 2-2
17	120916-RAN-1	stone 1
23	130916-RAN-1	stone 1-2
24	120916-Ran1-5	stone 5
25	120916-Ran1-7	stone 6
27	130916-Ran7-2	stone 1
	120916_Ran1-1	stone 1
	120916-Ran1-2	stone 2-(2)
	130916-RAN-1	stone 2

A1.2.2. Around Kabardinka 2

Sediments

Site no.	Sample no. 1 (site)	Sample no. 2
2-3	060916-KAB2-4	sample 6
2-4	050916-KAB2-3	sample 3
2-5	050916-KAB2-1	sample 1

2-6	050916-KAB2-sample 2	
2-7	050916-KAB2-4	sample 4
2-8	060916-KAB2-5	sample 7
2-9	060916-KAB2-2	sample 2
2-10	060916-KAB2-7	sample 12
2-11	050916-KAB2-5	sample 5
2-12	060916-KAB2-7	sample 1
2-13	060916-KAB2-6	sample 10
2-14	070916-KAB3-6	sample 11
2-15	060916-KAB2-1	sample 1
2-16	060916-KAB2-3	sample 5
2-17	060916-KAB2-2	sample 4
2-18	060916-KAB2-5	sample 8
2-19	060916-KAB2-9	sample 13
2-20	060916-KAB2-6	sample 9
2-21	070916-KAB3-7	sample 13
2-22	070916-KAB3-2	sample 2
2-23	070916-KAB3-1	sample 1
2-24	070916-KAB3-5	sample 7
2-25	060916-KAB2-9	sample 14
2-26	060916-KAB2-9	sample 14-2
2-27	070916-KAB2-5	sample 8
2-28	070916-KAB3-4	sample 5
2-29	070916-KAB3-7	sample 12
2-30	070916-KAB3-2	sample 3
2-31	060916-KAB2-10	sample 15
2-32	070916-KAB3-5	sample 9
2-33	070916-KAB3-4	sample 6
2-34	070916-KAB3-3	sample 4
2-35	070916-KAB3-5	sample 10
2-36	070916-KAB3-3	sample 4

Stones

Site no.	Sample no. 1 (site)	Sample no. 2
3	060916-KAB2-4	stone 1-(1)
11	060916-KAB2-8	stone 3-(1)
13	070916-KAB3-6	stone 5
14	130916-Kab6env-3	stone 3
15	070916-KAB3-2	stone 1
18	060916-KAB2-5	stone 2
19	060916-KAB2-9	stone 4-(2)
20	050916-KAB2-6	stone 1
21	070916-KAB3-4	stone 2-(1)

26	070916-KAB3-5	stone 3
	160916-KAB2-4	stone 1-(2)

A1.2.3. Around Podkumouk

Sediments

Site no.	Sample no. 1 (site)	Sample no. 2
1	150916-Pod-4	sample 6
2	150916-Pod-3	sample 4
3	150916-Pod-1	sample 1
4	150916-Pod-2	sample 3
5	150916-Pod-3	sample 5
6	150916-Pod-2	sample 2
7	150916-Pod-4	sample 7

Stones

Site no.	Sample no. 1 (site)	Sample no. 2
5	150916-Pod-1	stone 1-(1)
	150916-Pod-1	stone 1-(2)

A1.2.4. Gumbashi

Sediments

Site no.	Sample no. 1 (site)	Sample no. 2
8	140916-Gum3-1	sample 1
13	140916-Gum2-7	sample 1
17	140916-Gum2-1	sample 2
22	140916-Gum3-1	sample 2

Stones

Site no.	Sample no. 1 (site)	Sample no. 2
12	140916-Gum2-1	stone 1-(1)
22	140916-Gum3-1	stone 1
	140916-Gum2-1	stone 1-(2)

A1.2.5. Etc.

Soils

Site no.	Sample no. 1 (site)	Sample no. 2
9	140916-M-1	sample 1
14	140916-M-2	sample 2
18	140916-M-2	sample 3
30	120916-RAN-1	sample 1

Stones

Site no.	Sample no. 1 (site)	Sample no. 2
7	140916-M-2	stone 1

A1.3. Brief descriptions at the soil survey around Ransyrt 1 and Kabardinka 2

Soil survey according to the soil survey manual, United States Department of Agriculture. Color index by Munsell color chart.

A1.3.1. Survey around Kabardinka 2

No vegetation of trees.

- 050916-KAB2-1re(GPS): Start sample 1

The highest part of the plateau of Kabardinka 2. Plants cover the plateau but cut for the harvest etc. More than 5 cm depth due to vegetation. HUE 10 YR 4/2&3/2, dry not sticky, humid soils. Less than 2.5cm thick ribbon, very soft dark brown soils, probably influenced by organics. Silt loam?

- 050916-KAB2-2: Sample 2

Dry partly humid dark brown solid. HUE 10YR 4/1&3/1. Silty clay and silty clay loam.

- 050916-KAB2-3: Sample 3

Dark brown (organics) sandy. Fine dry sand. HUE 5Y 2/2 &3/2. Thick ribbon, 2.5-5cm. Very silty, silty clay loam.

- 050916-KAB2-4: Sample 4

Mixed layers of sedimentary rocks and vegetation soils? Variously sized grains. Dry+little bit humid. HUE 25 YR 4/6. Ribbon (thick) 2.5-5cm. Soft gritty. Mixture of sandy clay loam and silty clay loam.

- 050916-KAB2-5: Sample 5

Dry organic soil, sands are included. HUE 5Y 5/4. 2-5cm thick ribbon. Not soft and not gritty, clay loam.

- 050916-KAB2-7: Sample 6

Dark humid clayey soils.

- 060916-KAB2-1RE: Sample 1

5cm depth. Organic dark soils after 5-6 cm. Soft humid soils. HUE 10YR 2/3-5/6. Silt clay, silt loam.

060916-KAB2-1RE: Sample 2

30cm depth from the same spot. Sands from the southern sides. Yellowish but still organics. HUE 5Y 5/6-6/6. Gritty and 2-5cm ribbon thin-middle.

- 060916-KAB2-2: Sample 3 (no sampling)

Very dark-dark brown soils cover the area. Archaeological site.

060916-KAB2-3: Sample 4

HUE 5Y 4/3.

060916-KAB2-3: Sample 5

35cm depth from the sample 4 site.

HUE 5Y 6/4&4/3

Light yellowish brown soils under darker organic developed soils. Less than 2.5cm ribbon. Gritty sands.

- 060916-KAB2-4: Sample 6

HUE 10 4/6. Sands near the rocks (20-25cm) under 10cm top soils. Dry soils.

- 060916-KAB2-5: Sample 7

Around 20cm under the top soils. Dark yellowish brown top soils. Sand stones with quartz, etc. Iron concentrations. Dry. Not sticky. HUE 10YR 6/8.

060916-KAB2-5: Sample 8

After the thin layer of stones/sands, there are more light yellowish soils. Dry. Probably iron rich? Gritty. Around 2.5cm ribbon. HUE 10YR 8/8 or light yellowish. 60cm depth.

- 060916-KAB2-6: Sample 9

On the middle of the slope from the plateau. After 3cm depth. Small, red orange, light yellowish stones. Gritty but together with soft soils. 2.5cm ribbon.

060916-KAB2-6: Sample 10

Light yellowish sand. HUE 10YR 5/10.

- 060916-KAB2-7: Sample 11

Middle slope under the small mounds. Under the top soils (grey dark). Stone fragments after 21cm and light yellowish sticky soft soil separates (clay?). Orange yellowish sand stones. Sticky soils. HUE 25YR 7/8. Mostly gritty clay.

060916-KAB2-7: Sample 12

37cm depth from the same site. Light orange yellow. Sandy clay including aggregates with same grain composition. Sticky sand, Gritty. Mixtures of grey beige colors. At the 40cm depth: beige grey soils (sample 12). Heavier. Gradation layer of 15cm from yellow to grey beige. 50 cm depth arrived. 8 cm is for the grey soils. HUE 5Y 7/2.

- 060916-KAB2-9: Sample 13

Stone like soft aggregates. Iron rich sediments but grey beige inside. Dry. HUE YR 25 7/1, 6/6.

060916-KAB2-9: Sample 14

1 m distant from sample 13. Sticky clay. Grey-beige. Like sample 13.

060916-KAB2-9: Sample14-2

Hard state of the sample 14. More iron concentrations.

- 060916-KAB2-10: Sample 15

Dark organic brown sands. Gritty. 20 cm depth. Grey to brown grey. HUE10 4/2-4/3.

- 070916-KAB3-1: Sample 1

18cm under the top organic soils. HUE 5Y 7/4. 2-5cm ribbon. Siltky+gritty. Platy stones under this layer, bedrock?

070916-KAB3-2: Sample 2

Under the 15cm thick top soil. Blocky hard little humid soils. Very dark brown. HUE 10YR 3/2. Less 2cm ribbon. Gritty and silky. This structure is located in front of the fortress wall in the old water conservation system.

070916-KAB3-2: Sample 3

At the 53cm depth. Clay layer (yellow-brown) begins. At the 60 cm depth still clay with sand (approx. 20%). Soft+gritty. Sand stone (light yellow) included in this layer. Iron rich phase (aggregates). HUE 10Y 5/8. At the depth of 68cm: the same clay layer. Clay layer developed well.

- 070916-KAB3-3: Sample 4

Under the slope of KAB3, valley which creates temporary water flow or reservoir. Mortar like soils separates at the 7cm depth. Soils gathered at the 25cm from top soils. Aggregates. HUE 25Y 3/2 and 7/8.

070916-KAB3-3: Sample 4-2 (sample 5)

74cm depth from the same site of sample 3. Dark brown little gritty sands. 84 cm depth: same soils. Not gritty and not soft. Less than 2cm ribbon. HUE 5Y 2/2-3/2. Soils from the hills?

- 070916-KAB3-4: Sample 5

2m distant from the sample 4 next to the broken cliff in the valley. Yellowish sands occurred in the brown organic soils. Gathered at the 42cm depth. Yellow wet sands start at the depth of 32cm. Mixture with grey (mud?) soils.

070916-KAB3-4: Sample 6

65 cm depth, Same sands gradation from the orange red to grey color. Soils gathered from the grey parts. Yellow: HUE25Y 7/6 with the grey: HUE 5Y 7/1, 7/2

- 070916-KAB3-5: Sample 7

24-25 cm grey sands with the stones. Gritty. Light grey and yellow. Dominant in the gritty sands HUE N 8/0. HUE 10 GY 6/1. Hard aggregates. In the smaller river along the slope at the side. Wet, dark black/brown soils are exposed to the air. This water source would be permanent of half permanent/temporary.

070916-KAB3-5: Sample 8

32cm. Light grey gritty dominant. Wet. HUE N 8/0 mixed with HUE N 6/0 or HUE 2.5GY 5/1.

070916-KAB3-5: Sample 9

48cm depth. Dark black flexible. Light grey gritty sands and iron rich red aggregates/concentrations in the soils.

070916-KAB3-5: Sample 10

60 cm depth. Light yellow still gritty wet soils. 2-5 cm ribbon. Sand and gritty. Light brown dominant but grey soils with iron rich concentrations. Yellowish grey dominant. HUE25 8/8. But still light grey (carbonates?) and dark grey included.

- 070916-KAB3-6: Sample 11

Grey rocks included. Gritty sands. White carbonates. Somehow flexible and not dry. The start of the layer at the 12 cm depth after brown top soil. Rocks/lithics total more than 30% included. At the side of the river valley. 58cm depth. Still same stone and sand layer. HUE25YR 7/8. This river valley has two exposed stone bottom.

- 070916-KAB3-7: Sampe12

Little gritty. Wet. More than 5 cm ribbon. Red brown thin soils. Under the mounds where some water stays. After top soils, HUE10 7/8 & 8/8. River/water could help the sedimentation.

070916-KAB3-7: Sampe13

More carbonates are included. Grey white. Same color like sample 12.

- Conclusion: General survey around Kabardinka 2, 3 and environments

In the deep valley with the bigger sized grains or in the river valley with few clay deposits.

1. Deep valley: more organic dark soils are deposited, probably delivered from the upper side. Also it is possible that clay deposits or sedimentation for clay development occurred in such features. But because of the rapid change of the angle of the slope and scale, deposit of the organic soils could more easily take place.
2. River valley under the hills.

In this spot, it is also hard to find clay deposits. Probably, due to the flow speed of the river in/between the mountains, instead of the sedimentation process, transfer of the soils to the downside would be more preferred like 1. Even the bedrock is exposed to the air in this river.
3. On the slope of the hills where water stays for certain time shoed more possible clay deposits. Such sedimentation and weathering of the rocks into the soils process in/on the hills takes place in such water stay. It is questionable whether the ancient potters used this process.

A1.3.2. Survey around Ransyrt 1

No vegetation of the trees.

- 120916-Ran1-1: Sample 1

Due to the cultural layers around Ransyrt 1. Under the small mounds and lower place. HUE 10YR 4/3, 5/3. Some cm sized stones, stone fragments containing qtz and sediments. Dark brown soil influence. From organic top soil? After 15cm top soil, humid and sticky. Not soft and not gritty. 5cm ribbon (tough).

- 120916-Ran1-1: Sample 2

It gets more humid and sticky at 38 cm-53 cm depth. Still some rock fragments in cm size. HUE 10YR 3/3, 3/4.

- 120916-Ran1-2: Sample 3

On the top around Ran1 sites. Little bit under the other geological features. Under the 10 cm, dark brown organic top soil (dry) rock appears already. Bedrocks are embedded in the organic soils, 30-40 cm. Organic soils (dark, brown, dry) mixed with stones are gathered. Not soft and not gritty. HUE 25YR 5/2, 6/2.

- 120916-Ran1-5: Sample 4

On the way to the downhill, first spot. Small temporary? water flow with the hard (stones?) ground. Variously sized, coarse sands to the rocks (30-40 cm) in the water.

120916-Ran1-5: Sample 5

Next to the shallow water. Dark brown soils, sticky fine, soft containing stone fragments and sands.

120916-Ran1-5: Sample 6

Dark brown in the bottom left from sample 5. Middle sized (15cm) stones are embedded. But very sticky and soft. 3-10 cm depth. Similar to sample 5. Due to the rocks, cannot reach the lower layers, but more water exists. HUE 5Y 4/1, 3/1. Little bit grey? Soft.

- 120916-Ran1-6: Sample 7

In the temporary water reservoir. Below the mound, nearly the second down plateau. Began at the 20 cm depth. Sticky, soft, 5 cm ribbon, dark red brown. Some stone fragments (5-10cm) included. HUE 7.5 YR 5/4, 4/4.

120916-Ran1-6-2: Sample 8

From the site of sample 7. More reddish. Red brown soil. Sticky. Humid. HUE 5YR 5/8. Still mixture of the sample 6. Gritty and soft. Stone blocks at the next level of 35 cm (5cm thick layer with the stones).

- 120916-Ran1-7: Sample 9

The lowest part of the second step lower plateau. Lower parts which could have water. Blocks of soils. After 5 cm of top soils containing stone fragments. Dry (little humid?). Water vaporization in the sediment zone? HUE 2.5YR 6/1.

120916-Ran1-7: Sample 10

Less blocky. Stone fragments are embedded. Brown/red brown soils. Not soft and not gritty at the 20 cm depth. HUE 2.5R 5/3.

- 120916-RAN-1: Sample 1

After the top soil (sands) 3cm depth, after the organic soil (2nd black sands) till 15-20 cm depth. Sticky clayey soil in brown-grey. 2-5 cm ribbon but still gritty/not soft and not gritty. In the exposed broken (probably natural process) site. HUE 25 YR 6/3, 6/4. Small stone fragments (cm size) are embedded.

- 130916-Ran7-1: Sample 1

The site around Ransyrt 7. Probably water and soils are accumulated in this spot. After 10 cm depth of dark black top soils, brown grey soils appear. Little sticky and humid. But still dry and little bit gritty. At 30 cm depth, still same characteristics of the soils –gathered. HUE 10YR 4/6, 3/4. 2-5 cm ribbon. Not soft not gritty. Organics.

130916-Ran7-1: Sample 2

More grey and soft, sticky. 45-63cm depth. 5 cm ribbon. Soft. Little bit gritty and some stone fragments are embedded. HUE 10GY 5/1 & 5GY 2/1.

- 130916-Ran7-2: Sample 3

Blow the top mound. After the top soil (5-10cm). Brown little humid but dry soils. But stilly organic soils. HUE 10YR 4/3, 4/4. Till 40 cm. Stone fragments are embedded.

- 130916-Ran6env-1: Sample 1

After 15cm of the top soil (organic brown). Blocky, soft layer. This environment is on the very light slope, lower point. Soft but little gritty. Little sticky but hard blocks to the 24 cm depth. HUE 10YR 5/2.

130916-Ran6env-1: Sample 2

Stone fragments (4-5cm) containing qtz, sediments. More grey often to be seen as grey fragments (1-2mm). More humid & sticky at the 40 cm depth soil gathered. HUE 10GY 4/1, 5/1.

130916-Ran6env-1: Sample 3

Blocky soils (greyish brown). Again at the 44 cm depth. More sticky and humid. 5cm ribbon. Soft at the 55 cm depth still same layer. HUE 7.5 GY 5/1.

- 130916-Ran6env-2: Sample 4

Sticky red brown soil. Probably influenced by organics, but soft and humid. After 4 cm depth, this layer starts. HUE 7.5YR 6/3. It gets more humid and sticky and grey.

130916-Ran6env-2: Sample 5

After the 30 cm depth. Very sticky, clay, soft, 5 cm ribbon. Grey+red brown+light brown. Some sands (visible, 1-2 mm) are embedded. HUE 10 YR 6/2, 7/2 gathered at 43 cm.

130916-Ran6env-2: Sample 6

At the 45 cm depth. Red inclusions (probably iron rich) in the light grey brown clay. Sticky and humid. More flexible and water at the 48 cm-50 cm depth gathered. HUE 7.5 YR 7/3. Similar at the 57 cm depth.

A1.3.3. Survey around Gumbashi

No vegetation of trees. Broken cliff and pile up of the rocks. Relatively more sedimentation process in comparison to Ransyrt

- 140916-Gum3-1: Sample 1

Under the hill, the second step low plateau. In front of the beginning of the small trees in the water plants with shallow water. A flat small plateau next to the small valley. After 21 cm depth of the top soil (soft and little bit humid). Humid sticky soils appear. Still some organics. Brown. HUE 25YR 6/3, 6/2.

140916-Gum3-1: Sample 2

Slightly over the layer (3-5 cm) of the stone layer (bed rocks), there is a thin layer composed of more dark, grey brown soils. Humid, soft, sticky. Soils are gathered at the 35-37 cm. Because of the bed rock (easily broken) stone fragments are included. Some light brown weathered inclusions probably from the bed rock sediments. HUE 25 YR 3/1.

- 140916-Gum2-1: Sample 1

After the 22 cm, thick top soils (little humid, organic, soft). Humid sticky soils appear. HUE 7.5YR 6/1.

140916-Gum2-1: Sample 2

At the 30 cm, the soils become more brown and sticky, humid. Still much organics. At the 31 cm stone layer –Bedrock. 20-30 cm the red brown grey soil layer mixed with the stones. HUE 7.5YR 6/4, 5/3.

Appendix 2. Sample list

Samples were named after 1) the name of the site; 2) the context/quadrat number; 3) additional number according to the amount of the ceramic sherds. The photos were taken by the author.

A2.1. Ransyrt 1 (North Caucasus)

80 samples for the analysis

Ran1=Ransyrt 1

Ran1_514_1

Micro-photo

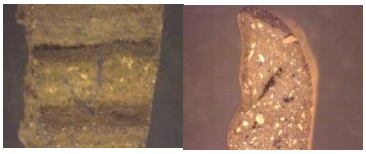

Ran1_514_2

Micro-photo

Ran1_514_3

Micro-photo

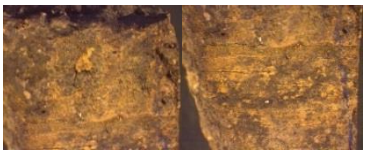

Ran1_527_1

Micro-photo

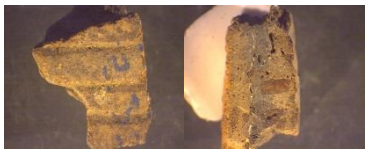

Ran1_5 (product rests? chunks?) No image

Ran1_5_2 (Erdproben) No image

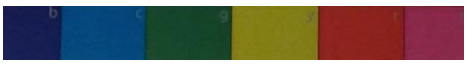

Ran1_dmp1 (Ran1_dmp)

Ran1_dmp2

Ran1_KB3kc1

Ran1_329

Ran1_449

Ran1_452

Ran1_488


Ran1_549


Ran1_470_x: deformed ceramic


Ran1_470_ceramic: carbonate aggregates


Ran1_370_1: fired clay chunks?


Ran1_192_51


Ran1_210_13


Ran1_272_17

No image

Ran1_362_8


Ran1_449_44

Ran1_527A_6

Ran1_198_4

Ran1_211_4

Ran1_260_49

Ran1_357_20

Ran1_541_11

Ran1_N1_1-55

Ran1_217_17

Ran1_224_6


Ran1_244_4


Ran1_298_3


Ran1_527_20


Ran1_630_20


Ran1_192_10


Ran1_326_9


Ran1_529_4


Ran1_554_4


Ran1_214_10


Ran1_261_40


Ran1_437_83


Ran1_515_5

Ran1_619_31

Ran1_17_2

Ran1_225_4

Ran1_332_31

Ran1_538_16

Ran1_619_23

Ran1_N18_49

Ran1_6_2

Ran1_6_11

Ran1_223_11

Ran1_276_26

Ran1_313_2

Ran1_N18_38

Ran1_133_1

Ran1_278_x

Ran1_309_10

Ran1_543_12

Ran1_601_7

Ran1_N18_6

Ran1_167_4

Ran1_244_9

Ran1_279_13

Ran1_306_5

Ran1_N1_1-1

Ran1_462_14

Ran1_509_9

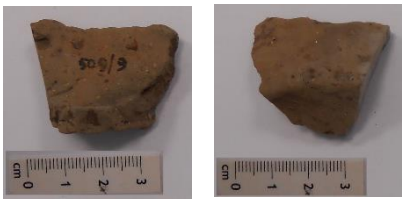

Ran1_129_5

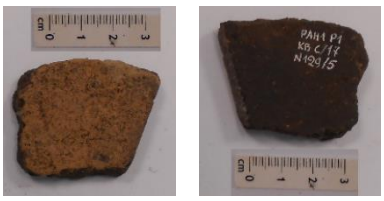

Ran1_239_4

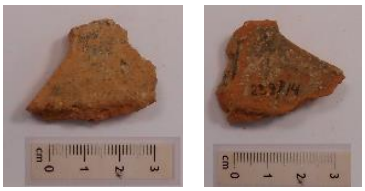

Ran1_571_6

Ran1_6_9

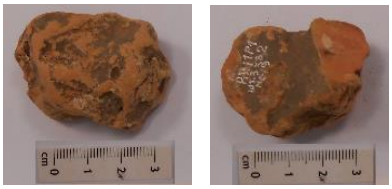

Ran1_440_35

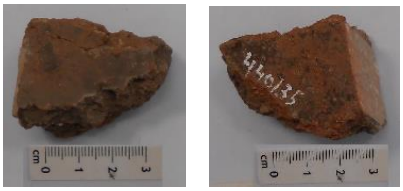

Ran1_N1-1-1

Ran1_489_46

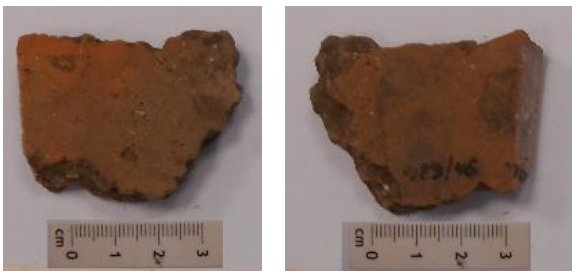

Ran1_279_1

Ran1_441_31

white

Ran1_224_9

Ran1_111_1

A2.2. Kabardinka 2 (North Caucasus)

70 samples for the analysis

KAE=Kabardinka Archaeological Expedition, Kab2=Kabardinka 2

KAE2007, KAE2008 = Kab2

KAE2007-797_1

KAE2007-1123_1

KAE2007-636_1


KAE2007-1697_1

KAE2007-2055_1


KAE2007-482_1


KAE2007-1160_1


KAE2007-1976_1


KAE2007-1142_3


KAE2007-1763_1

KAE2007-2258_5

KAE2007-1235_1


KAE2007-1599_1


KAE2007-824_1

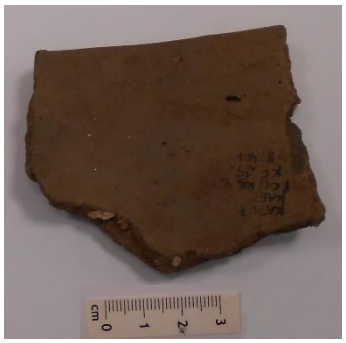


KAE2007-1603_4


KAE2007-1253_3


KAE2007-1408_1


KAE2007-1587_1


KAE2007-1579_2


KAE2007-no number


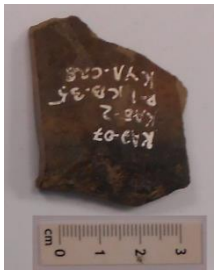

KAE2007-28_2

KAE2007-2257_5

KAE2007-918_1

KAE2007-1418_1

KAE2007-2067_3

No image

KAE2007-1962_1

KAE2007-558_1

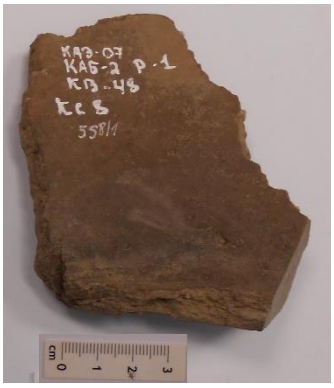

KAE2007-760_1

KAE2007-1848_9

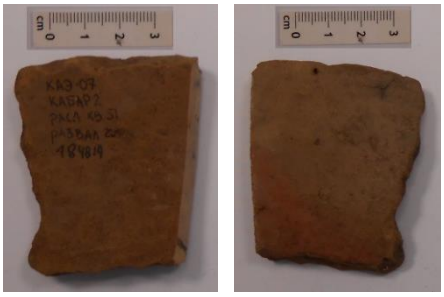

KAE2008-482_14

KAE2008-483_3

KAE2008-516_2

KAE2008-853_1

KAE2008-565_1

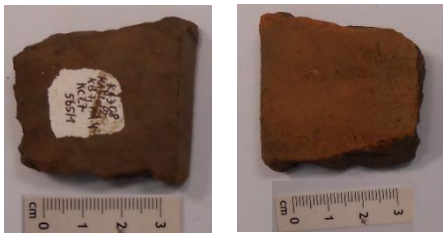

KAE2008-1070_2

No image

KAE2008-1006_1

KAE2008-1195_6

KAE2008-1260_4

KAE2008-483_4

KAE2008-647_14

KAE2008-1220_3

KAE2008-516_26

KAE2008-641_1

KAE2008-410_1

KAE2008-659_6

KAE2008-1396_4

KAE2008-383_8


KAE2008-1152_1


KAE2008-294_1

No image

KAE2008-743_1


KAE2008-1398_1


KAE2008-482_13


KAE2008-693_1


KAE2008-1244_1


KAE2008-483_x1


KAE2008-1021_1


KAE2008-1162_1

KAE2008-657_3

KAE2008-663_11

KAE2008-516_20

KAE2008_294_1

KAE2007_416_9

KAE2007_2062_3

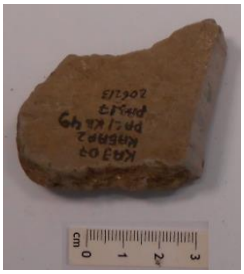

white

KAE2007_650_10

KAE2007_1578_4

KAE2007_944_1

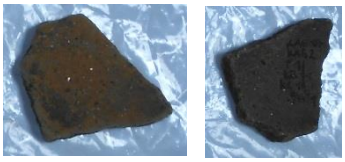

KAE2007_2123_1

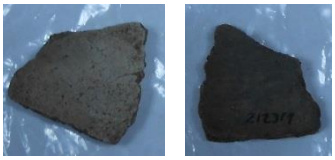

KAE2008_844_1

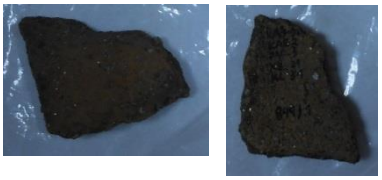

KAE2008_633_1

A2.3. Levinsadovka (Mius Peninsular)

7 samples for the analysis (small rests from the Taganrog project)

Lev=Levinsadovka

Lev_7467
Lev_7687
Lev_7718
Lev_8653
Lev_8653_1
Lev_8653_2
Lev_9633

A2.3. Saf'janovo (Lower Don river)

14 samples for the analysis (small rests from the Taganrog project)

Saf= Saf'janovo

Saf_501_1
Saf_501_2
Saf_501_3
Saf_501_4
Saf_501_5
Saf_501_6
Saf_501_etc
Saf_502_1
Saf_502_2
Saf_502_3
Saf_502_etc (including flint)
Saf_x_1
Saf_x_2
Saf_x_etc

Appendix 3. Analysis of Calcium Carbonates from the Context, Ransyrt_2015_No.470

A3.1. Introduction

In an excavated context at Ransyrt 1, no. 470, a huge mixture of carbonate aggregates and ceramics were found. The ceramic sherds were highly deformed and carbonates fill the cracks in the sherds. This type of carbonate aggregates was only found in this context from the excavation in Ransyrt 1 in 2015. They are connected to several fragments of the ceramic body causing cracks and precipitation of calcite in the ceramic. This intense influence took place also only in these fragments. The genesis of this composite mixture can be assumed in three different ways: 1) the development of the aggregates through the precipitation is not related with the ceramic sherd. The both objects were buried together; 2) the aggregates are developed from the burnt lime and the re-precipitation process (transformation of the lime into calcite) took place next to the ceramic body; 3) the aggregates are developed from the lime after the firing together with the ceramic body in the low temperature and re-precipitation process occurred to the both objects.

In order to clarify the development process of the carbonate aggregates and the relation to the deformation of the ceramic pottery in the aggregates, two objects found at this context, carbonate aggregates (Figure A3-1: Ransyrt1_2015_470_x) and a sherd mixed with carbonates (Figure A3-1: Ransyrt1_2015_470_ceramic) were selected and analyzed by multiple analytical instruments.

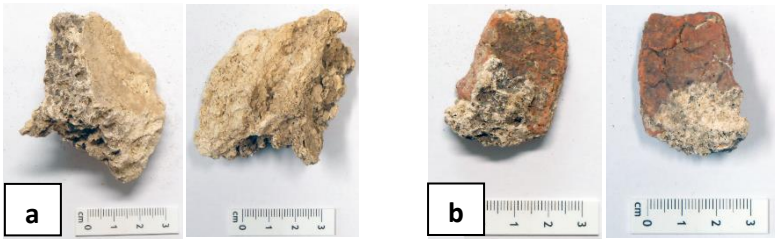

Figure A3-1. Objects from the context no. 470. a) Carbonate aggregates (Ransyrt1_2015_470_x); b) Ceramic sherd deformed by the aggregates (Ransyrt1_2015_470_ceramic). Photos taken by the author.

A3.2. Methods

The objects were investigated by the polarized light microscopy, XRD, SEM-EDS/WDS, SEM-Maps, Raman spectroscopy, due to the high degree of heterogeneity in the chemical and mineralogical composition. Using XRD, Doppel – Pulverdiffraktometer PDF-2 by the Fa. EFG GmbH Berlin, mineral phases in the powder form of aggregates and the deformed ceramic body were identified. The measurement condition was 40 kV/30 mA (1200 W) using Cu-anode (CuKα). SEM revealed more detailed image and chemical and mineralogical composition of the deformed ceramic and carbonates. It was performed on the thin section of the samples by JEOL JXA 8200 Superprobe at the mineralogy/petrology laboratory equipped with EDS/WDS. For the conductivity, they were coated by Carbon. The quantitative analysis of carbonates was done by the beam size of 10 µm. For the investigation of various shapes and morphology of carbonates in higher spatial resolution, ZEISS SUPRATM 40 VP Ultra with thermal field emission cathode and Oxford instruments EDX-System with INCA-software. The sample was coated with Tungsten. Raman spectroscopy provided useful

evidence for the mineral phase according to the crystal shapes of carbonates. It is performed by Horiba ISA Dilor Labram, micro-confocal Raman spectrometer with a diameter of 1 µm, a focal length of 300mm and a spectral resolution of up to 3.5 cm^{-1}. Depending on the analysed material and the applied method, the user can choose between the internal 632 nm He-Ne and an external 532 nm Nd-YAG laser.

A3.3. Results

The fabric of carbonates shows fine grained structure which is further categorized into two kinds of subtypes: 1) nodular or tuberose, milky, opaque, porous; 2) massive or compact, milky, opaque, porous. Macroscopically, the aggregates seem to be a deposit of roughly spherical form with irregular protuberances.

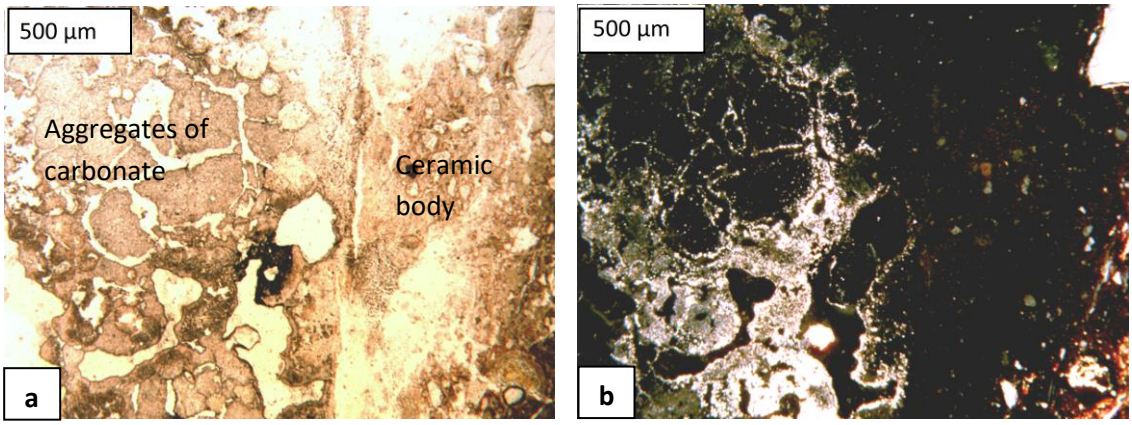

Figure A3-2. Images from the polarized light microscopy between the aggregates and ceramic body deformed by aggregates. a) plane polarized light; b) cross polarized light.

The polarized light microscopic images revealed similar appearance and structure, translucent and porous in round shapes but without twinning (Figure A3-2). The aggregates contain opaque and darker parts as well. The high birefringence color and fine granules indicating microcrystalline is dominant in the aggregates and deformed ceramic sherd (Figure A3-3).

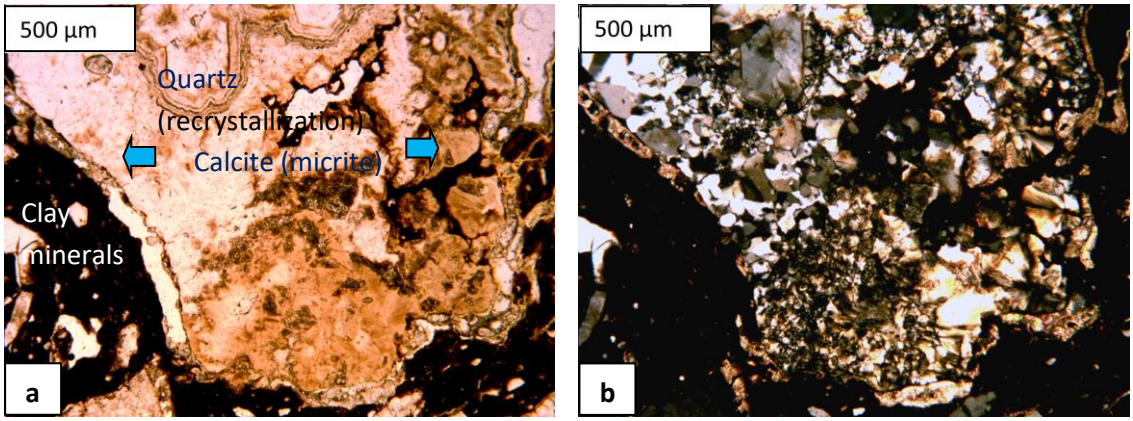

Figure A3-3. Secondary development of calcium carbonate between the quartz grain and clay minerals. Images from the polarized light microscopy in the ceramic body connected to the aggregates. a) plane polarized light; b) cross polarized light.

These carbonates are all identified as calcite by XRD (Figure A3-4). The main peaks from the both instruments come from calcite indicating calcite as a dominant phase and other minerals like magnesite, portlandite, quartz, brucite, siderite and goethite as a minor phase (Table A3-1, Figure A3-4). Ca-hydroxide (portlandite) is present but in a very small quantity.

	Calcite	Magnesite	Portlandite	Quartz	Brucite	Siderite	Goethite
Ransyrt1_2015_470_x	+++++	+	(+)	(+)	(+)	(+)	(+)

Table A3-1. Qualitative evaluation of mineral phases existing in the aggregates (+++++: 80-10%; +++:50-80%; ++:20-50%; +: 5-20%; (+): under 5%).

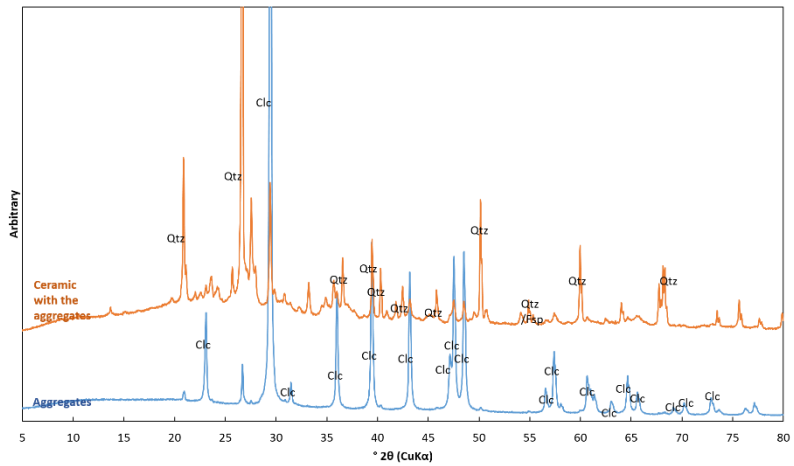

Figure A3-4. XRD peaks of the calcium carbonate aggregates and the deformed ceramic body (Qtz:quartz; Clc: calcite).

The SEM shows these various morphological features composed of the carbonate grains in various sizes (Figure A3-5). Mostly, submicron sized fine grains are forming a lamellar structure (Figure A3-5a). Ca detected in the aggregates by EDS indicates Ca-carbonates. Mixed phases with clay minerals were observed in the boundary between the ceramic body and aggregates (Figure A3-5b). They do not appear from the surface to the middle of the aggregates. The intrusion of clay minerals took place in the separated blocks caused by cracks and large pores.

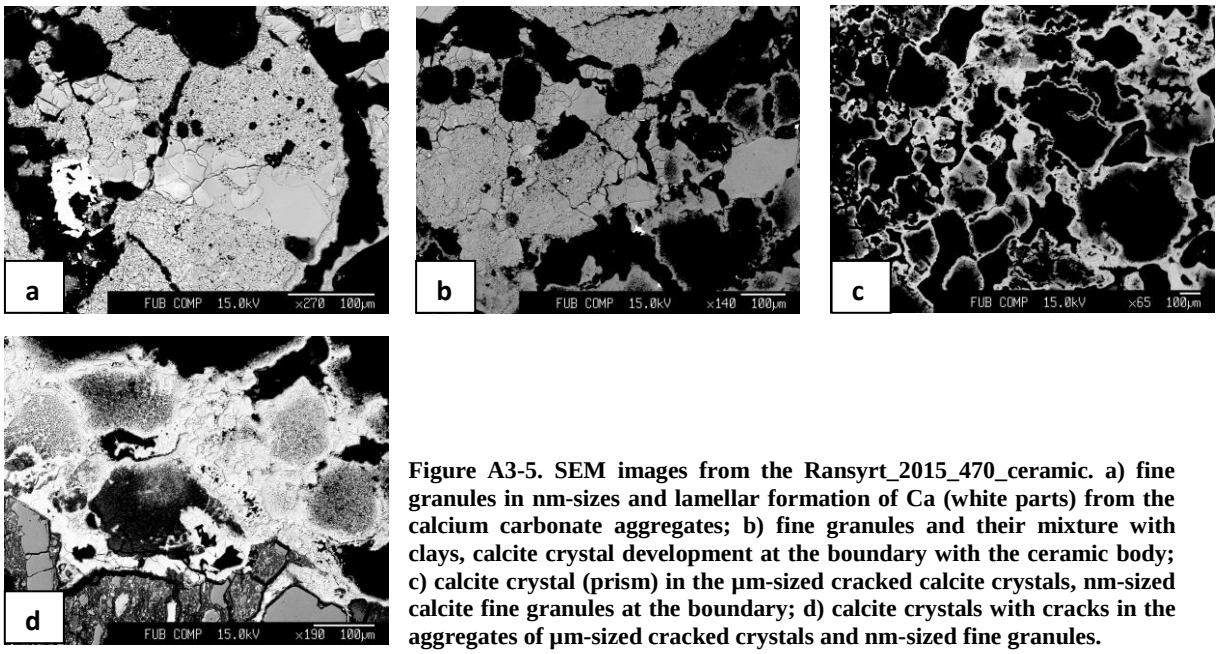

Figure A3-5. SEM images from the Ransyrt_2015_470_ceramic. a) fine granules in nm-sizes and lamellar formation of Ca (white parts) from the calcium carbonate aggregates; b) fine granules and their mixture with clays, calcite crystal development at the boundary with the ceramic body; c) calcite crystal (prism) in the µm-sized cracked calcite crystals, nm-sized calcite fine granules at the boundary; d) calcite crystals with cracks in the aggregates of µm-sized cracked crystals and nm-sized fine granules.

In the images by the FESEM, the three dimensional stack of the aggregate shows more various structures and shapes of Ca-Carbonate (Figure A3-6) [1-2]. High porosity and pseudo-lamellar form of crystal assembly, rhombohedral-hexagonal shapes, small needle like shape, radiation form on the edges of the aggregate blocks (plants like), or some assembly has a mixed form of hexagonal and scalenohedral crystal shapes and fusing Ca-carbonate.

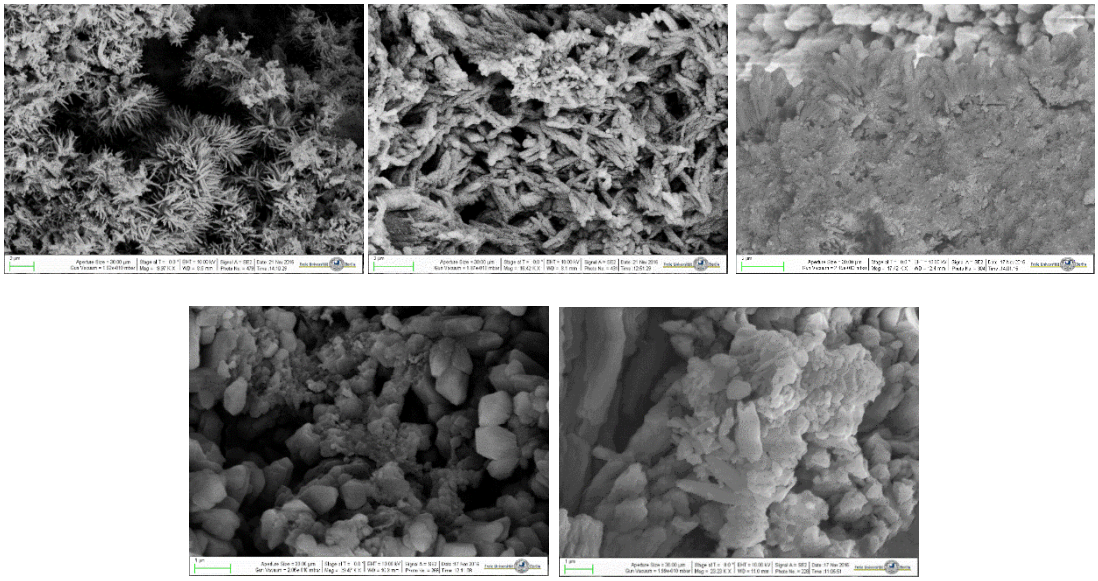

Figure A3-6. SEM images rhombohedral-hexagonal shapes, small needle like shape, radiation form on the edges of the aggregate blocks (plants like).

The chemical composition of the carbonates was measured for the individual carbonate grains bigger than 10 µm (Figure A3-7). In general, the grains contain relatively low ratio of Mg (<1.7 wt.%) and Fe (<0.25 wt.%) in comparison to the Ca is present. The ratio between CaO and CO_2 shows the typical linear tendency which fits to the calcium carbonate (approx.. CaO: CO_2 = 6:4 (wt.%)) (Figure A3-8).

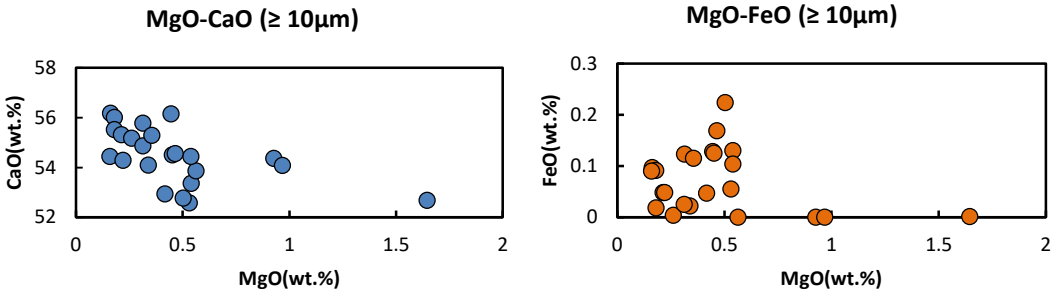

Figure A3-7. MgO-CaO-FeO composition in calcium carbonate crystals (≥10µm) (wt.%).

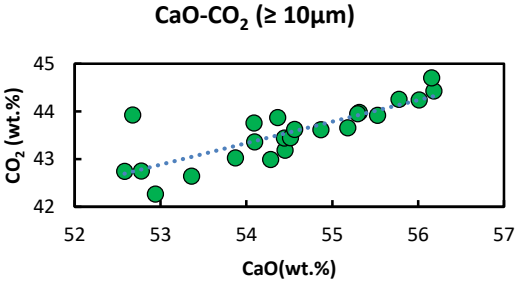

Figure A3-8. Relationship between CaO and CO_2 component (wt.%).

The contents of Mg in the carbonate grains were originated from the original ceramic pastes such as clay minerals, supported by the chemical elemental maps (Figure A3-9). The dominant area of Ca and Mg is clearly separated in the maps and the distribution of Mg coincides more with that of Si representing the ceramic paste. In the calcite aggregates, not so much content of Carbon is detected in the aggregates, probably because of the measurement crystal of the SEM.

However, despite of various shapes/morphology and Mg/Fe contents in the carbonates, these Ca-carbonates were identified only as calcite by the Raman spectroscopy as the XRD of the powder samples indicated and no other polymorphs were detected (Figure A3-10).

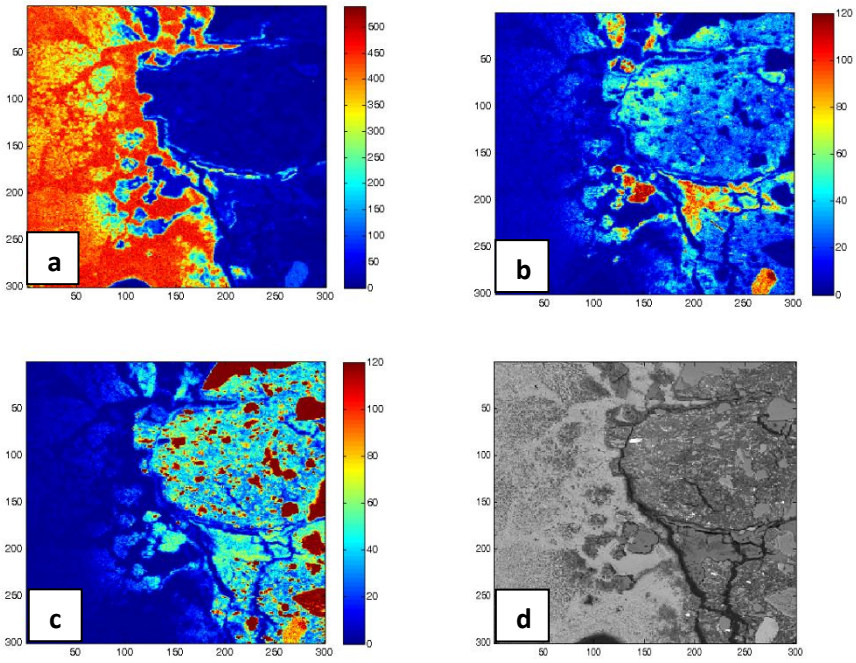

Figure A3-9. Element distribution map: a) Ca; b) Mg; c) Si; d) BSE compression image.

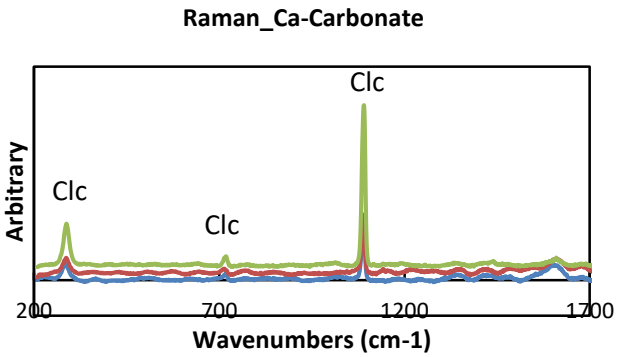

Figure A3-10. Raman spectra of calcite in various shapes.

A3.4. Discussions and conclusions

The pseudo-lamellar, globular form of the micro-fabric in the carbonates indicates the slow precipitation process, often related to CO_2-rich water. A mixed phase in darker or opaque color is the result of the influence of the ceramic paste in the ceramic sherd or clay minerals from the ground to the carbonate precipitates. In the ceramic sherd, microcrystalline calcite, micrite is dominant, which is very common in other ceramic sherds which show the secondary development of calcite from the

deposited earth [3]. It supports this product as the results of the precipitation or re-precipitation of calcium carbonate in the ceramic body. The precipitation process can produce the new crystallization pressure of calcite in confined spaces and caused cracks and deformation [3]. The prismatic or rhombohedral faces with cracks and pores of calcite crystals indicate the recrystallization process, observed in the precipitation process as well [4]. In the meanwhile, in the boundary of the whole aggregate, different faces of fine granules caused by the wreathing process or mechanical stress appear, indicating possible heterogeneous origin during the development of this aggregate. The relatively low ratio of Mg (<1.7 wt.%) in comparison to the Ca indicates low temperatures during this development of aggregates. This mineral could be formed from the Ca^{2+}-, CO_2 -rich water through the following reaction [3,5].

$$Ca^{2+} + 2HCO_3^- \rightarrow CaCO_3 + CO_2 + H_2O \quad \text{(A3-1)}$$

If the aggregates are burnt lime fired together with ceramics, the firing temperature should reach at least the decarbonation temperature (600-800 °C) which seems to be acquired from an intensive firing process [3,5-6].

$$CaCO_3 \text{ (Calcite)} \xrightarrow[\text{Heat}]{} CaO \text{ (Lime)} + CO_2 \quad \text{(A3-2)}$$

However, between the aggregates and the ceramic body or in the ceramic body no Ca-Al-Silicates or Ca-Silicates expected from the firing reaction (higher than 900-1000 °C) were detected by the Energy-dispersive-spectrometry [3,6-8]. Just small amounts of Ca were found in the reaction rims or the melted phase through this method. Anorthite from this ceramic body detected by XRD and SEM would be the original component of the resource. According to the results, whether the aggregates would be fired together with the ceramic body or separately is still to be investigated.

If the Ca-carbonate aggregates are developed from rests of the burnt lime, it will be combined with the water and forms portlandite [6],

$$CaO + H_2O \rightarrow Ca(OH)_2 \text{ (Portlandite)} \quad \text{(A3-3)}$$

This new mineral is also transformed into calcite easily in the air through the carbonation reaction occurs from the surface into the pore system [4],

$$Ca(OH)_2 + CO_2 \rightarrow CaCO_3 + H_2O \quad \text{(A3-4)}$$

Another possibility of the development of the aggregates from dolomite is also hardly probable because of the lack of dolomite and brucite in the ceramic body or the aggregates from the following reaction [5],

$$CaMg(CO_3)_2 \rightarrow CaCO_3 + MgO + CO_2 \quad \text{(A3-5)}$$

$$MgO + H_2O \rightarrow Mg(OH)_2 \text{ (Brucite)} \quad \text{(A3-6)}$$

Although the morphology of Ca-carbonate crystals includes various forms, faces and sizes, they can appear in all three hypotheses mentioned at the beginning. The results can shed light on the detailed use of Ca-aggregates by the inhabitant.

A3.5. References

1. de Leeuw, N.H., Parker, S.C. Surface Structure and Morphology of Calcium Carbonate polymorphs calcite, aragonite and vaterite: An atomic approach. J. Phys. Chem. B 102 (1998) 2914-2922. https://doi.org/10.1021/jp973210f.

2. Sekkal, W., Zaoui, A. Nanoscale analysis of the morphology and surface stability of calcium carbonate polymorphs. Sci. Rep. 3 (2013) 1587. https://doi.org/10.1038/srep01587.

3. Fabbri, B., Gualtieri, S., Shoval, S. The presence of calcite in archaeological ceramics. J. Eur. Ceram. Soc. 34 (2014) 1899-1911.

4. Cizer, Ö., Rodriguez-Navarro, C., Ruiz-Agudo, E., Elsen, J., VanGemert, D., van Balen, K. Phase and morphology evolution of calcium carbonate precipitated by carbonation of hydrated lime. J. Mater. Sci. 47(16) (2012) 6151-6165. https://doi.org/10.1007/s10853-012-6535-7.

5. Trindade, M.J., Dias, M.I., Coroado, J., Rocha, F. Mineralogical transformations of calcareous rich clays with firing: A comparative study between calcite and dolomite rich clays from Algarve, Portugal. Appl. Clay Sci. 42 (2009) 345-355. https://doi.org/10.1016/j.clay.2008.02.008.

6. Cultrone, G., Rodriguez-Navarro, C., Sebastian, E., Cazalla, O., de la Torre, M.J., Carbonate and silicate phase reactions during ceramic firing. Eur. J. Mineral. 13 (2001) 621-634.

7. Duminuco, P., Messiga, B., Riccardi, M.P. Firing process of natural clays. Some microtextures and related phase compositions. Thermochim. Acta 321 (1998) 185-190. https://doi.org/10.1016/S0040-6031(98)00458-4.

8. Riccardi, M.P., Messiga, B., Duminuco, P. An approach to the dynamics of clay firing. Appl. Clay Sci. 15 (1999) 393-409. https://doi.org/10.1016/S0169-1317(99)00032-0.

Appendix 4. Official transport of the archaeological ceramics from Russia to Germany (in German)

Official contract for the transport of the samples from German Embassy in Moscow, Russia to Deutsches Archäologisches Institut in Berlin, Germany
2 Copies

Bitte die auszufüllenden Stellen mit F11 anspringen (nur bei MS-Word möglich)

Auftraggeber: ***(Behörde/Referat)***

Gz.: ***(Geschäftszeichen)***

Ort, Datum
Berlin, 27.07.17

E-Mail : poststelle@ dainst. de
Tel.: 030 / 187711 /122

An das Auswärtige Amt

☐ Referat 114-50@diplo.de (Bonn – Luftfracht / Landfracht)

☒ Referat 115-5@diplo.de (Berlin – Luftbeutel)

Betr.: **Versandverfügung für die Kurierstelle** (auch vorab als Avis)

Bezug: Richtlinien für die Beförderung von Kuriersendungen, EGO 16-5 Ziffer 4.1

Anlag.: **2 Pakete**

☒ Haftungsausschluss- und Kostenübernahmeerklärung (umseitig)

☐ Begründung des amtlichen Interesses durch AV/AA (umseitig)

Die angelieferte Sendung enthält keine Verschlußsachen, kein Gefahrgut und keine zollpflichtigen Gegenstände. Sie soll unbegleitet über den amtlichen Kurierweg versandt werden:

Absender/Anlieferer: **DB - Moskau**

Adressat/Endempfänger: **DAI – Zentrale Berlin, Eurasien Abt. / Fr. Reinhold**

Zweck/Veranlassung:

Inhalt: **Wiss. Proben**

Wert: ca. EURO, Gewicht: **6,- kg**

Maße (bei Luftbeutel): x x cm / Packhöhe (bei Fracht): cm

Ankunft am Zielort bis spätestens (Datum): **schnellstmöglich**

Besonderheiten: **DAI / 090 – 008 / 28.07.17**

Kostenträger:
☒ Auftraggeber
☐ Adressat/Endempfänger
☐ Globalbudget der AV
☐ DiA/EÖA-Zweckmittel der AV
☐ siehe Rückseite
☐ _____

Haftungsausschluss- und Kostenübernahmeerklärung

Unter Bezugnahme auf die mir bekannten Richtlinien für die Beförderung von Kuriersendungen erkläre ich mich hiermit damit einverstanden, dass das Auswärtige Amt im Falle von Verlust, Beschädigung oder verzögerter Zustellung der umseitig beschriebenen Sendung keine Haftung übernimmt.

Die Transportkosten für diese Sendung sollen mir unter folgender Adresse in Rechnung gestellt werden:

Begründung des amtlichen Interesses:

☐ Botschaft/Generalkonsulat in *(Dienstort)*_____

☐ AA-Referat _____

☐ Es handelt sich nur um Bundeseigentum (Haftungsausschuß-Erklärung entfällt), das inventarisiert wird bei: _____

☐ Der Versand muss als *Diplomatic Mail* erfolgen, weil …

Curriculum Vitae

Because of the personal data privacy, Curriculum Vitae is not provided in the electronic version of the thesis.